Department of Precision and Microsystems Engineering

A planar precision stage using a single image sensor

Len van Moorsel

Report no : 2017.005
Coach : J.W. Spronck
Professor : J.L. Herder
Specialisation : Mechatronic System Design
Type of report : Master of Science Thesis
Date : 2 February 2017

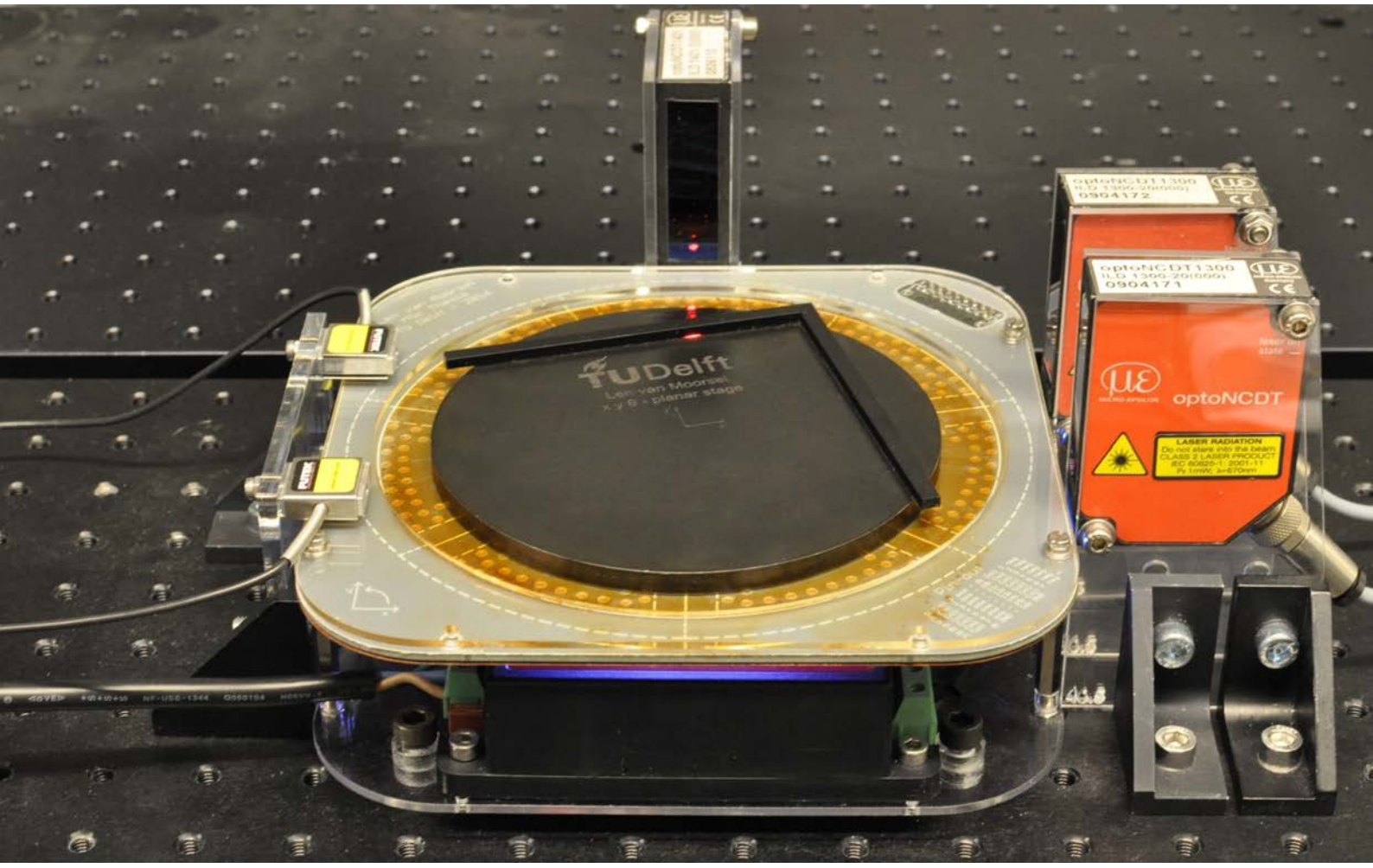

TU Delft Delft University of Technology

Challenge the future

A planar precision stage using a single image sensor

by

Len van Moorsel

in partial fulfillment of the requirements for the degree of

Master of Science
in Mechanical Engineering

at Delft University of Technology.

February 2, 2017

Thesis committee:	ir. J.W. Spronck	TU Delft, supervisor
	Prof. dr. ir. J.L. Herder	TU Delft
	Prof. dr. ir. E.G.M. Holweg	TU Delft
	dr. ir. L. Sasso	TU Delft
	dr. ir. B.A.J. Lenseigne	TU Delft

This thesis is confidential and cannot be made public until February 2, 2022.

Faculty of Mechanical, Maritime and Materials Engineering (3mE)
Delft University of Technology

TU Delft Delft University of Technology

Abbreviations

ADC Analog to Digital Converter. 21, 24, 62
AFPMM axial flux permanent magnet motor. 28, 79

CCD Charge-Coupled Device. 9, 89, 90
CE Chip Enable. 106
CL closed-loop. 6, 26, 56, 60, 61, 70, 102, 104
CMOS Complementary Metal Oxide Semiconductor. 9, 89, 90
CSI Camera Serial Interface. 90
CSI-2 Camera Serial Interface Type 2. 90

DAC Digital to Analog Converter. 51
DOF Degree of Freedom. vii, ix, 1, 56–58, 66, 68, 79, 81, 82
DoF Depth of Field. 17, 19–21, 34, 75
DOFs Degrees of Freedom. vii, viii, 1, 3, 7, 9, 13, 27, 32, 61, 63, 70, 81, 82, 85

EMF Electromotive Force. 48, 49

FFT Fast Fourier Transform. 62, 64, 103
FOH first-order-hold. 67–69
FPGA Field Programmable Gate Array. 81

I2C Inter-Integrated Circuit. 50, 105
ICs Integrated Circuits. 89

LPF low-pass filter. 48, 49, 59, 66–69

MIMO Multiple-Input Multiple-Output. 55, 80
MIPI Mobile Industry Processor Interface. 90
MISO Master In Slave Out. 106
MOSI Master Out Slave In. 106
MPC model predictive controller. 80

NA Numerical Aperture. 17–21

OL open-loop. 25, 26, 56, 60, 61, 70, 102, 104

PCB Printed Circuit Board. viii, 27, 31, 36–42, 45, 54, 78–81, 96–98

PD Proportional and Derivative. 25
PI Proportional and Integral. 67
PID Proportional, Integral and Derivative. 55, 59, 60, 69, 86
PSD Position Sensitive Device. 1
PWM Pulse Width Modulation. 47–52, 105

SCK Serial Clock. 106
SISO Single-Input Single-Output. 55, 80, 82
SPI Serial Peripheral Interface. 21, 51, 62, 63, 105, 106
SS Slave Select. 106

UART Universal Asynchronous Receiver Transmitter. 105

VC-A Vibration Criterion A. 5

ZOH zero-order-hold. 24, 60, 65, 67, 68, 70

Nomenclature

B magnetic flux density. 95
B_r remanent flux. 91, 92
C rotational damping coefficient. 57
D duty cycle. 47
I moment of inertia. 57
M magnification. 18, 21
N f-number. 20, 21
N_w working f-number. 19–21
V_EMF back EMF. 48, 49
V_out average output voltage. 48
V_s power supply voltage. 48, 52
Φ magnetic flux. 91, 92
$\boldsymbol{F}$ force vector. 42
$\boldsymbol{I}$ current vector. 42
$\boldsymbol{\Phi}$ force transformation matrix. 43, 44
ϵ positioning error. 6
λ wavelength. 18, 21
$\mathbf{B}$ magnetic flux density. 29, 91–93
$\mathbf{F}$ Lorentz force. 29, 95
$\mathbf{I}$ current. 29
$\mathcal{F}$ magnetomotive force. 37, 91, 92
$\mathcal{R}$ reluctance. 91, 92
μ_0 magnetic permeability. 92
ω_c bandwidth. 6
ω_c cutoff frequency. 49, 50, 59
ρ resistivity. 38
b image distance. 18, 21
c circle of confusion. 19–21, 34
c damping coefficient. 6, 57
d aperture diameter. 18–21
d_Abbe Abbe resolution. 18, 20, 21
f focal length. 18, 20, 21
f_PWM PWM frequency. 51, 52, 75
f_clock clock frequency. 51, 52
k spring stiffness. 6
l length of the coil in the magnetic field. 29
l_m length of the magnet from north to south pole. 92
m mass. 6, 57
n index of refraction. 18, 19
s Laplace operator. 6
v object distance. 18, 19, 21

Abstract

This thesis presents the design, implementation and validation of a standalone, three degree of freedom x, y, θ_z planar precision stage, with novel sensing and actuation concepts. This stage is one of the first stages capable of large planar translations (30 mm) as well as infinite rotation with only one moving part and a single sensor.

In microscopic research, it is often desirable to observe regions of interest with high resolution in two or three dimensions. Those regions are generally too large to be captured by a single image at sufficient resolution. The reduced field of view creates the need for a system to (re)position and orientate the object of interest within the field of view of the microscope. In precision engineering such a positioning system is commonly referred to as a stage. By controlling the position of the stage, the region of interest displayed can be changed. Moreover, when the microscope is placed under an angle with the plane of interest, a free rotation θ_z of the stage around a certain x,y-location would enable the user to obtain a 3D image of the object.

Conventional systems either use two or three separate stages for achieving the three Degrees of Freedom (DOFs). State-of-the-art stages with a single mover have been developed for positioning with nanometre precision, positioning using low-cost mouse sensors or rotating 360°. These stages have downsides: respectively, an expensive sensor system, a limited rotational range of approximately 5° or only a small translational range of 9 mm.

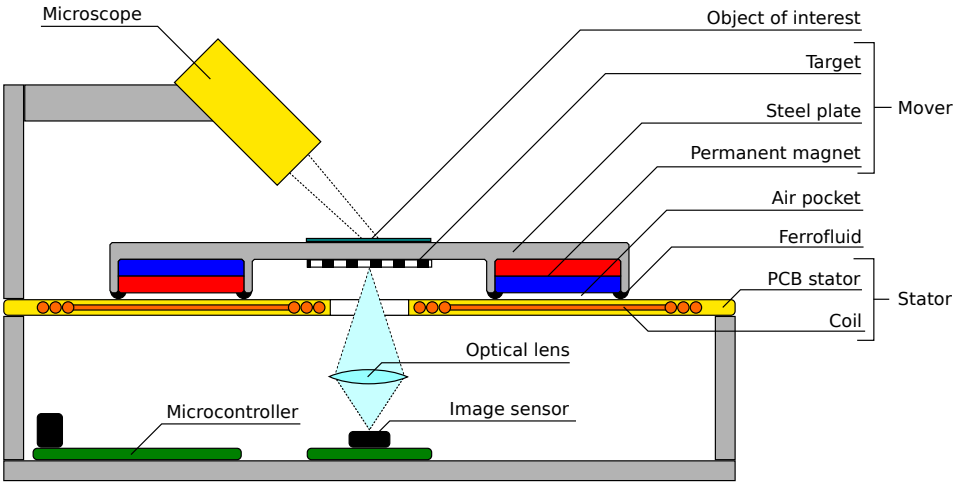

Figure 1: System overview showing the location of the microscope, object of interest for microscopy, mover with magnets and target, stator and sensor system, with respect to each other.

The goal of this thesis is to design a three Degree of Freedom (DOF) planar precision stage using a single image sensor. The stage proposed in this research combines the concepts of a low-cost sensor system with infinite rotation and large translations,

resulting in a system that can be used in a wide range of applications, such as 3D microscopy. This thesis presents the sensor system, electromagnetic actuator design, real-time control system and implementation as a standalone system.

The **sensor system** makes use of a low-cost (30 euro) 8 megapixel (MP) digital image sensor. The sensor is placed below the mover (Figure 1). It recognises a part of the target: a pattern of QR-like codes at the bottom of the mover. Digitally processing the images theoretically allows extracting the absolute 6 DOFs of the mover. The three planar DOFs are used in this project to determine the planar position (x, y) and rotation (θ_z) of the mover. The designed sensor system measures a translational range of 30 mm in x and y, limited by the size of the target, and infinite rotations in θ_z. The minimum sensor-system measurement dispersion is below 2 µm (3σ) in translation and below 0.005° (3σ) in rotation. The sample rate of the sensor system depends on the number of pixels processed by the image-recognition algorithm. For an image size of 1.2 MP a sample rate of 2 Hz was obtained. For an image size of 0.02 MP sample rates of up to 25 Hz were achieved.

The **actuator** consists of a stationary Printed Circuit Board (PCB) containing coils and a mover with permanent magnets. The mover rests on top of the PCB. It has a circular shape and consists of a 2 mm thick steel plate and a ring of eight alternating magnet segments on the bottom of the steel plate: four segments with upward-facing north poles, and four segments with downward-facing north poles. The coils in the stator create Lorentz forces on the permanent magnets in the mover. The shape and functionality of seven independent coils has been integrated in the PCB. By applying currents through the coils, seven independent Lorentz forces can be generated on the mover. By combining different forces, the desired translations and rotations can be achieved at every location. The actuator is designed for translational steps of 1 mm within 0.5 s, a rotational speed of 36°/s, and low power losses for the provided forces. This limits power consumption and heat generation to a maximum of 40 W.

A ferrofluid bearing is applied between the mover and the PCB. Ferrofluid consists of nanometre-size ferromagnetic particles suspended in a liquid carrier. This fluid accumulates at the locations of highest magnetic field intensity: in this case at the corners of the magnets of the mover. The ferrofluid seals eight pressurised volumes of air between the mover and the PCB and acts as a hydrostatic bearing, allowing loads of up to 100 N. The bearing system uses the same permanent magnets as used by the actuator. This synergy allows for a low number of parts. The absence of stick-slip makes this bearing suitable for high-precision positioning systems for applications such as a micrometre precision stage for microscopy. Translational motions are finite and acceleration forces dominate the corresponding necessary forces up to 0.4 N. Rotational motion is infinite and the corresponding required torque of 0.1 Nm is dominated by the damping coefficient of the bearing multiplied by the rotational velocity of the mover.

A **control system** is implemented to work standalone on a low-cost microcontroller (Raspberry Pi 3). The microcontroller simultaneously processes the images acquired by the sensor. The control system bandwidth of 10 Hz is designed to suppress external vibrations with amplitudes up to 37 mm/s^2. It is designed to work with the delay and relatively low sample rate of 16 Hz of the sensor system. Separate low-cost microcon-

trollers (based on Arduino Cortex-M0 architecture) are used as motor control units to control the currents through the coils. The user can change the 3 DOF position setpoint of the mover with a 3D mouse.

The implementation as a standalone system is realised within a size of 175x175x50 mm (Figure 2) and works independently outside a lab environment. The total component cost of the developed stage is below 300 euro. Although the bandwidth is limited to 10 Hz, this is sufficient for human users. Therefore this stage could be used in applications in need of micrometre precision at a low cost, such as digital microscopy.

In **conclusion**, a cost-effective, standalone, three degree of freedom micrometre precision stage has been developed, by applying existing sensor and actuation principles in a new and innovative way. The feasibility of using a vision system for position control of a micrometre precision stage has been demonstrated. Since high-performance computing power continues to decrease in cost, the future perspective for these systems is bright.

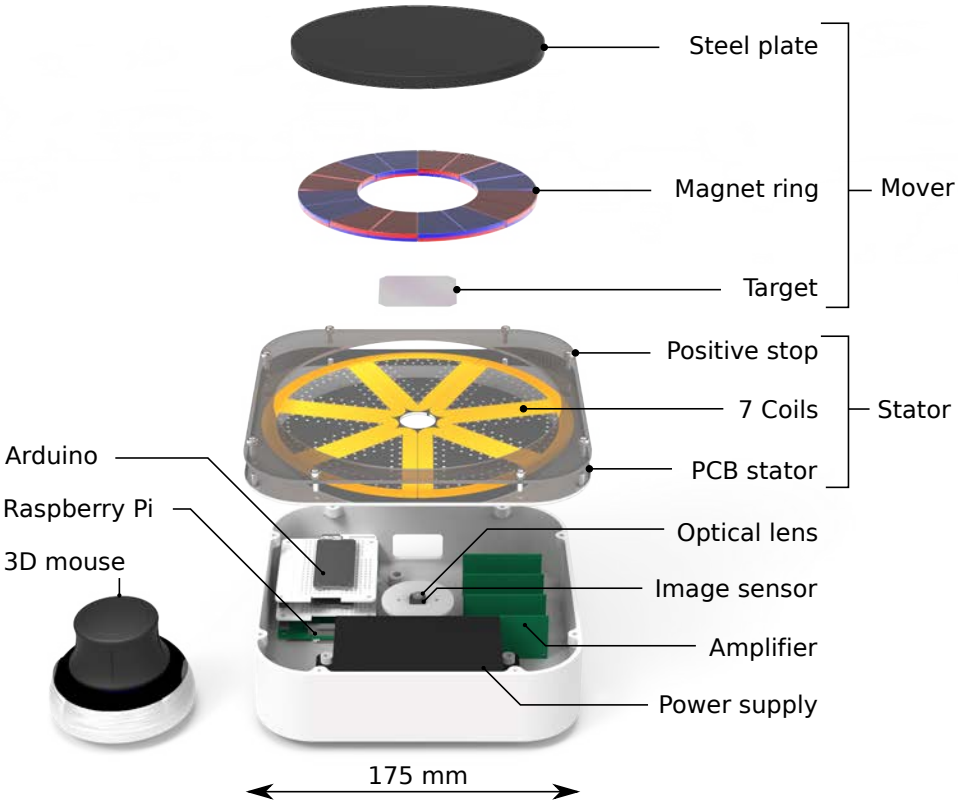

Figure 2: Exploded system overview.

Acknowledgements

The past eleven months have been quite an adventure. It was a continuous roller-coaster of highs and lows, however the highs were higher than the lows, which would not have been the same without the Mechatronic System Design group. The atmosphere in the group has been very inspiring, and I am proud to say that I have been part of it.

Through the support of the entire group I have learned more than I could have ever expected. I learned how to build an embedded control system running on standalone hardware, do electromagnetic simulations in COMSOL, build my own PCBs using Eagle and program software in Python and C++. These are skills that I never expected to learn as a Mechanical Engineer, but I am very glad to have acquired.

Hereby I would like to express my gratitude to everyone who contributed directly or indirectly to this thesis.

First and foremost, I would like to thank Jo Spronck as my supervisor and for being my mentor. The weekly meetings where he would always respond with a "no" have been very helpful throughout the project.

Figure 3: Jo Spronck studying ferrofluid and magnetism in the lab.

Just Herder, for the insight in how to structure academic presentations and papers, and being the chairman of the exam committee.

Boris Lenseigne, for discussing possible image-recognition algorithms, challenging me that it would be hardly possible to use image recognition on a microcontroller for position control, and being part of the exam committee.

Edward Holweg and Luigi Sasso for being interested in my work and for taking time to be part of the exam committee.

Rafael Muñoz Salinas from the University of Córdoba, as a developer of the ArUco marker recognition algorithm, for the support to implement the marker recognition algorithm on the microcontroller.

Hassan HosseinNia, for the insight he has provided in designing basic PID controllers and advanced Smith Predictors.

Niranjan Saikumar, for the knowledge and troubleshooting support for the H-bridge implementation and help with writing paper proposals.

Stefan Lampaert, for his support with modelling and design of the ferrofluid bearing.

Jaap Kokorian, for the support with LaTeX.

Jos van Driel, for his help with the measurement equipment and LabView.

Rob Lutjeboer, Harry Jansen & Patrick van Holst, for their assistance in the lab.

Gert Spek, for helping out with my early C++ programs.

Efraïm Eland, for his help selecting components for the amplifier design.

Joeri Simonian, for helping out with rendering and producing a very small marker.

My house mates, for their support and good care when I was not at the university.

My fellow students, for their sharing of knowledge and the discussions during the Monday morning meetings, the hard-earned coffee breaks and the late evenings. Bart, Bas, Gijs, Tobias, Joost, Arjan, Martijn, Raoul and Eshan, thank you!

And last but not least, I would like to thank my parents for their unconditional support through all those years.

Len van Moorsel, February 2017

Contents

Abbreviations ii

Nomenclature iv

Abstract vii

Acknowledgements xi

1 Introduction 1
- 1.1 Digital microscopy . . . 1
- 1.2 State of the art . . . 1
- 1.3 Project objective . . . 2
- 1.4 Additional goals . . . 2
- 1.5 Thesis overview . . . 2

2 Conceptual system design 5
- 2.1 Requirements . . . 5
- 2.2 Specifications . . . 5
  - 2.2.1 Controller bandwidth and error rejection . . . 6
  - 2.2.2 Required actuator forces . . . 6
  - 2.2.3 Required actuator torque . . . 7
- 2.3 Additional design requirements . . . 7
- 2.4 Conceptual system overview . . . 8

3 Sensor system 9
- 3.1 Image sensor . . . 9
  - 3.1.1 Binning and upsampling . . . 11
  - 3.1.2 Sensor placement . . . 12
- 3.2 Target and image recognition . . . 12
  - 3.2.1 Conceptual sensor system design . . . 12
  - 3.2.2 ArUco target . . . 14
  - 3.2.3 ArUco image-recognition algorithm . . . 15
- 3.3 Optics . . . 17
  - 3.3.1 Resolution . . . 17
  - 3.3.2 Magnification . . . 18
  - 3.3.3 Diffraction limit and Numerical Aperture . . . 18
  - 3.3.4 Depth of field . . . 19
  - 3.3.5 Trade-off diffraction limit and depth of field . . . 20
  - 3.3.6 Specifications of the optical system . . . 21
- 3.4 Validation . . . 21
  - 3.4.1 Number of sensor bins . . . 22
  - 3.4.2 Calibration . . . 23

3.4.3 Measurement dispersion . . . 23
3.4.4 Tracking . . . 24
3.4.5 Delay and sample rate . . . 25
3.4.6 Trade-off measurement dispersion and sensor delay . . . 25
3.5 Specifications of the complete sensor system . . . 26
3.6 Conclusion . . . 26

4 Actuator **27**
4.1 Conceptual actuator design . . . 27
4.1.1 Literature . . . 28
4.1.2 Power losses . . . 28
4.1.3 Lorentz force . . . 29
4.1.4 Conceptual analysis . . . 29
4.1.5 Model limitations . . . 30
4.1.6 Design guidelines . . . 31
4.1.7 Final trade-off . . . 31
4.1.8 Mover and stator dimensions . . . 32
4.2 Mover design . . . 32
4.2.1 Bearing system . . . 32
4.2.2 Magnetic design . . . 34
4.2.3 Load capacity and stiffness validation . . . 35
4.3 Stator design . . . 36
4.3.1 Optimising the number of windings . . . 37
4.3.2 PCB design . . . 39
4.3.3 Thermal design . . . 40
4.4 Actuator forces and torque . . . 42
4.4.1 Force transformation matrix . . . 42
4.4.2 Modelling . . . 43
4.4.3 Validation . . . 44
4.5 Conclusion . . . 45

5 Amplifier **47**
5.1 Introduction to PWM . . . 47
5.2 H-bridge . . . 48
5.3 Load . . . 48
5.4 Implementation . . . 50
5.4.1 Timers, counters and PWM . . . 51
5.4.2 Power supply . . . 52
5.5 Validation . . . 52
5.5.1 Power supply . . . 52
5.5.2 H-bridge . . . 53
5.6 Current controller . . . 53
5.7 Conclusion . . . 54

6 Controller **55**
6.1 Controller goals . . . 56
6.2 Performance specifications . . . 56

6.3 System . . . 56
6.4 Inverse transformation matrix and commutation . . . 58
6.5 Basic control: introduction to PID control . . . 59
6.6 Basic controller . . . 60
6.7 Closed-loop system identification . . . 61
6.8 Advanced control . . . 65
6.8.1 Model Predictive Control . . . 66
6.8.2 Reconstruction filter . . . 67
6.8.3 Smith predictor with reconstruction filter . . . 68
6.9 Advanced controller . . . 69
6.10 Conclusion . . . 70

7 Results **71**
7.1 Step response . . . 71
7.2 Positioning precision . . . 72
7.3 Positioning stability . . . 73
7.4 Linearity . . . 74
7.5 Specifications of the complete system . . . 75

8 Discussion **77**

9 Conclusion **79**

10 Recommendations **81**

Bibliography **83**

A Paper proposals **85**
A.1 Axial Flux Permanent Magnet Motor Design for Large Translations . . . 85
A.2 XY∞: Implementation of a Vision System for Position Control of a Planar Precision Stage . . . 86

B Ferrofluid damping **87**
B.1 Translation . . . 87
B.2 Rotation . . . 87

C Image sensor technology and hardware selection **89**
C.1 Image sensor technology . . . 89
C.2 Hardware selection . . . 90

D Detailed magnetic design **91**
D.1 Magnet thickness . . . 91
D.2 Steel backing plate . . . 91
D.3 Single or double rotor . . . 92
D.4 Distance between rotor and stator . . . 92
D.5 Steel ring and ferrofluid location . . . 93
D.5.1 Ferrofluid location defined by the magnetic field intensity . . . 93
D.5.2 Flux density . . . 93
D.5.3 Negligible influence of current on the ferrofluid location . . . 94
D.6 Magnet selection . . . 95

E PCB design for an electromagnetic actuator **96**
E.1 PCB basics . . . 96
E.2 Board design. . . . 96
E.3 Size of PCB and coils . . . 96
E.4 Design approach . . . 97
E.5 Eagle commands . . . 97
E.6 Meeting the design rules . . . 97
E.7 Exporting Eagle files to Solidworks . . . 98

F PCB connector and pin-out **99**

G Current controller **100**

H Rotational controller **102**
H.1 Basic controller . . . 102
H.2 System identification . . . 103
H.3 Advanced controller. . . . 104

I Software **105**
I.1 Communication: SPI . . . 105
I.2 H-bridge control. . . . 106

1

Introduction

1.1 Digital microscopy

In microscopic research, it is often desirable to observe regions of interest with high resolution in two or three dimensions. Those regions are generally too large to be captured by a single image at sufficient resolutions. Therefore optical magnification is applied, increasing the resolution while simultaneously reducing the field of view. The reduced field of view creates the need for a positioning system to move the object of interest into the field of view of the microscope. Such a positioning system is commonly referred to as a stage in precision engineering. Moreover, when the microscope is placed under an angle with the plane of interest, a free rotation θ of the stage around a certain x,y-location would enable 3D imaging of the object.

1.2 State of the art

Conventional systems either use two or three separate stages for achieving the translations and rotation. A number of state-of-the-art ferrofluid stages with a single mover have been developed in recent years. Max Café [1] developed a research stage for ferrofluid research. The planar range of the stage is limited to 10x10 mm and rotation is limited. The sensor system uses three laser interferometers and three capacitive sensors for 6 DOF control. The laser interferometers cost approximately €10k each and the capacitive sensors €1k. The high cost of the sensor system makes this stage unsuited for low-cost applications. Gihin Mok [2] built a second stage that uses two low-cost mouse sensors, to significantly reduce the cost of the overall system. His sensor system is able to retrieve 3 DOF information, however with a significant delay due to the internal working of the mouse sensors. The rotational range of the stage is limited. Haris Habib [3] built a third stage that is able to rotate 360°. A relatively expensive Position Sensitive Device (PSD) sensor of €600 is used that is able to theoretically measure 4 DOFs. A trade-off had to be made between range and resolution, since the size of the PSD is limited. His stage has a translational range of 9x9 mm.

Since camera sensors for mobile phones are the highest volume image sensor application in the world, these sensors with relatively high performance are available at a low cost. With a single camera sensor in theory 6 DOFs can be absolutely measured and the planar and rotational range can be decoupled from resolution. The resolution can be designed by changing the field of view and the number of pixels of the image

sensor. The range is independent of the field of view of the image sensor if overall position information is made available locally through codification. The range is then only limited by the total size of the recognised target.

1.3 Project objective

Given the current lack of large range micrometre precision stages using cost-effective sensors and an unexplored cost-effective sensor technology, an interesting research topic is the application of such an image sensor in a precise positioning system. This project focuses on the design of a three degree of freedom planar stage using a single image sensor, with micrometre positioning precision in x and y and sub-degree precision in θ.

A complete mechatronic system will be designed, and a specific feasibility study of implementing a vision system for position control will be performed. Although current vision systems are limited by computational power and therefore by cost, the future perspective of these systems is bright, since low-cost systems with high performance are foreseen in the near future.

1.4 Additional goals

The final result of this research should be a demonstrator. A number of additional goals should be achieved for this project to be successful:

- **Demonstrate working of new type of optical position sensor** a novel type of sensor system for precise position measurement should be developed.
- **Robust performance & Reliability** the system should work under a large range of circumstances, and not be significantly influenced by the environment. A simple system with a low number of parts is aimed for.
- **Cost-effective** the system should offer micrometre precision at a low cost. All subsystems should thus be cost-effective: sensor system, actuator, bearing, software and electronics. To reach this goal open-source software will be used instead of commercial software for the sensor system, actuator and communication. The control system will be built in Matlab Simulink. All software is thus fully known and can be modified.
- **Standalone** the system should work independently from lab equipment like dSPACE and external amplifiers. To reach this goal the entire system will be implemented on cost-effective microcontrollers, such as a Raspberry Pi or an Arduino.

1.5 Thesis overview

In Chapter 2 the conceptual system design for a demonstrator stage using a single image sensor will be presented. General requirements and specifications are deducted with the application of digital microscopy in mind. These are used as design targets for the different functions: sensor system, actuator and control system. Chapter 3 describes the sensor system that is developed in this project and its performance. The sensor system will be used for position feedback of the mover. Seven Lorentz actuators

are used to actuate the demonstrator stage in three DOFs. Chapter 4 describes the conceptual and detailed design of those actuators and the bearing system. The voltages to drive the currents through the Lorentz actuators are regulated by H-bridges. The design and implementation of these amplifiers is described in Chapter 5. The control system that closes the loop between the sensor system, actuator and amplifiers is described in Chapter 6. The performance of the complete system is evaluated in Chapter 7. Chapter 8 contains the discussion and the conclusions are presented in Chapter 9. Chapter 10 lists the recommendations. Multiple appendices on different subjects are present, and are referred to if more information on a certain subject is required.

2

Conceptual system design

To design this positioning system, requirements are formulated with the application of digital microscopy in mind. Further specifications are derived from these requirements. This chapter is concluded with a conceptual overview of the complete system.

2.1 Requirements

The requirements are based on microscopic applications such as blood cell or chip inspection. The requirements are shown in Table 2.1.

Table 2.1: Requirements for the planar stage based on digital microscopy applications

Requirement	
Degrees of Freedom	3: x, y, θ
Positioning	absolute
Load capacity	$\geq 100\,\text{grams}$
Range of translational operation	$\geq 30\,\text{mm}$
Range of rotational direction	∞ degrees
Speed of rotational operation	$\omega \geq 36\,^\circ/\text{s} = 0.1\,\text{Hz}$
Resolution in translational directions	$\leq 1\,\mu\text{m}$
Resolution in rotational direction	$\leq 0.01^\circ$
Precision in translational directions (3σ)	$< 10\,\mu\text{m}$
Precision in rotational direction (3σ)	$< 0.1^\circ$
Settling time for 5 mm translational step	1 s
Settling time for 1 mm translational step	0.5 s
Settling time for 10° rotational step	1 s
Settling time for 1° rotational step	0.5 s

2.2 Specifications

During microscopic research, the object of interest should stay in place with respect to the microscope. External vibrations cause disturbances that need to be rejected.

Floor vibrations measurements were performed in the mechatronics lab [4]. The largest amplitude of $2.2\,\text{mm/s}^2$ has a frequency of 10 Hz. According to the American high-technology company BBN, Vibration Criterion A (VC-A) is adequate in most instances for optical microscopes up to 400x zoom. This corresponds to accelerations

of $37\,\mathrm{mm/s^2}$ [1]. As a requirement $37\,\mathrm{mm/s^2}$ will be used.

Since the planar stiffness of a ferrofluid bearing is close to zero, the demonstrator stage can be modelled as a mass-damper system. A control system is used to add virtual stiffness to this system, for which sufficient bandwidth is needed. Additionally a high bandwidth allows for fast positioning. The frequency response $G(s)$ of the mass-damper system is:

$$G(s) = \frac{1}{ms^2 + cs} \tag{2.1}$$

where s is the Laplace operator, m is the mass of the mover and c the damping coefficient. By adding a controller $C(s)$ consisting of only a proportional gain K_p:

$$C(s) = K_\mathrm{p} \tag{2.2}$$

a mass-damper-spring system is created, defined by the closed-loop (CL) response of this system:

$$T(s) = \frac{CG}{1 + CG} = \frac{K_\mathrm{p}}{ms^2 + cs + K_\mathrm{p}} \tag{2.3}$$

where T is the complementary sensitivity function, and K_p acts as a spring stiffness k.

2.2.1 Controller bandwidth and error rejection

The mass of the mover times the acceleration gives a force that should be compensated for by the control system.

$$F_\mathrm{control} = ma_\mathrm{vibrations} \tag{2.4}$$

The maximum positioning error ϵ allowed under certain accelerations determines the stiffness the controller should add to the system.

$$F_\mathrm{control} = k\epsilon \tag{2.5}$$

The controller bandwidth ω_c is equal to the square root of the control stiffness divided by the mass of the mover.

$$\omega_\mathrm{c} = \sqrt{\frac{k}{m}} \tag{2.6}$$

This yields:

$$\omega_\mathrm{c} = \sqrt{\frac{a_\mathrm{vibrations}}{\epsilon}} \tag{2.7}$$

With the positioning error ϵ limited to $10\,\mu\mathrm{m}$ and vibration levels of $37\,\mathrm{mm/s^2}$, a bandwidth of $10\,\mathrm{Hz}$ is obtained.

2.2.2 Required actuator forces

The expected mass of the stage is $500\,\mathrm{g}$. The required actuator forces to reject the disturbances are therefore:

$$F_\mathrm{disturbance} = ma_\mathrm{vibrations} = 0.019\,\mathrm{N} \tag{2.8}$$

Simon van Veen [4] derived a formulation to determine the necessary force for step of size x_s with a settling time t_s:

$$\frac{x_s c^2}{c(2\tau - t_s) + m(1 + e^{(-c/m t_s)} - 2e^{(\frac{c(\tau - t_s)}{m})})} \tag{2.9}$$

where m is the mass of the mover, c the damping coefficient and τ is defined by:

$$\tau = t_s(1 + \frac{1}{2}\log\frac{1 + e^{(-c/m)}}{2}); \tag{2.10}$$

A 1 mm step with a settling time of 0.5 s and a damping coefficient of 24 Ns/m, as derived in Appendix B, results in a force of 0.14 N. However, since the damping coefficient of the ferrofluid bearing is a large unknown, a safety factor 3 is used, thus the total required force becomes 0.4 N.

2.2.3 Required actuator torque

For the torque needed in rotation, the requirement of a constant speed of rotation of 36 °/s is leading. The rotational damping coefficient is calculated in Appendix B. The required torque is given by:

$$T = C_\theta \frac{d\theta}{dt} = C_\theta \omega \tag{2.11}$$

For a rotational damping coefficient of 20.9×10^{-3} Nms/rad, a torque of 13×10^{-3} Nm is necessary. Since little experimental results are available on the rotational damping of a ferrofluid bearing, the damping coefficient in rotation is uncertain. Therefore the required torque is set to 0.1 Nm.

2.3 Additional design requirements

- **Single mover:** Conventional systems use multiple stages placed on top of each other to achieve the translations and rotations in the three DOFs x, y and θ. For this novel type of demonstrator a requirement is set that there should be only one mover.
- **Manufacturability:** The parts should be manufactured in-house or ordered at one of the suppliers of the university.
- **Design for assembly:** A low number of parts decreases the time of assembly.
- **Serviceability:** The components should be easy to access and to adjust, so that different configurations can be tested and components with low tolerances can be aligned.
- **Adjustable software & hardware:** The software and hardware used should be easily adjustable, to allow different configurations to be tested.

2.4 Conceptual system overview

Figure 2.1 shows the conceptual system overview. The microscope is placed under an angle to allow 3D visualisation of the region of interest. The object of interest is placed on top of the mover. A target is placed on the bottom of the mover and is seen by the image sensor of the sensor system. A lens is used for optical imaging and magnification. The field of view of the microscope is aligned with the sensor system to reduce Abbe errors. Lorentz forces act on magnets in the mover. Ferrofluid is used as a bearing system between the mover and the actuator.

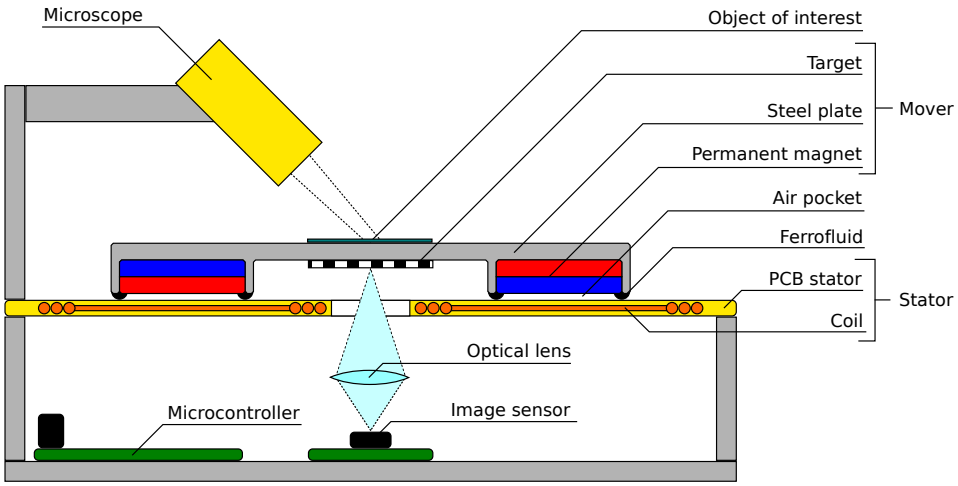

Figure 2.1: System overview

3

Sensor system

The sensor system measures the position of the mover in the three DOFs: x, y and θ. Since cameras used in the mobile phone industry have significantly decreased in price over the past decade, an interesting research topic is to investigate if such an image sensor can be used for a micrometre positioning system. The sensor system uses an 8 megapixel image sensor similar to the camera sensors in present-day mobile phones. Since the image sensor by itself is not able to detect a position, it is combined with an image-recognition algorithm and a target on the mover, containing a pattern to be recognised. To create an image of the target on the sensor, an optical lens is used. As is seen in this chapter a trade-off has to be made between resolution, depth of field, delay and sample rate of the sensor system by adjusting two variables: number of pixels and optical magnification. Summarising, the sensor system consists of an image sensor, an image-recognition algorithm, a target and optics. In this chapter these subjects will be covered and the performance of the sensor system is measured.

3.1 Image sensor

Two types of image sensor technologies are commercially available: Charge-Coupled Device (CCD) and Complementary Metal Oxide Semiconductor (CMOS). Although CMOS was known to acquire lower quality images than CCD, the quality of CMOS has significantly increased. A detailed description of the two technologies is found in Appendix C.1. For this research a CMOS image sensor was selected.

A 5 MP camera for a Raspberry Pi, named camera module V1.3 (Figure 3.1), was selected at the start of this project. However, during the project a new 8 MP camera module (V2.1) was released, based on the Sony IMX219 image sensor. The performance of these two image sensors was compared and camera module V2.1 was selected for the final design. A more detailed description of the camera modules is found in Appendix C.2.

The IMX219 is an image sensor based on CMOS technology and has a sensor area of 3280 x 2464 pixels. Each pixel has a size of 1.12 µm, giving a total sensor area of 3.674 x 2.760 mm, corresponding to a sensor diagonal of 4.6 mm. Further specifications are listed in Table 3.1.

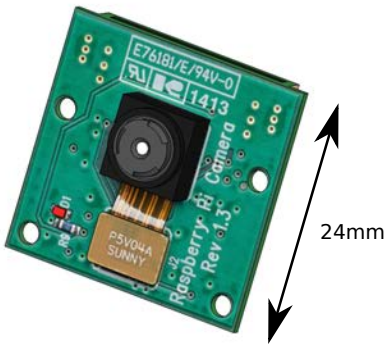

Figure 3.1: Raspberry Pi camera module. The camera module is based on the 8 MP Sony IMX219 image sensor.

Table 3.1: Specifications of the Sony IMX219 image sensor used in the Raspberry Pi camera module V2.1

total number of active pixels	8.08 MP
number of active pixels	3280 x 2464
size of each pixel	1.12 µm
sensor area	3.7674 x 2.760 mm
sensor diagonal	4.6 mm (Type 1/4.0)
frame rate at 1280 x 720	198 fps
frame rate at 960 x 540	240 fps

Pixel arrangement

Since the visible spectrum of white light consists of a range of wavelengths from 400 to 700 nm, the image sensor has red (R), green (G) and blue (B) photo sensors. These sensors act as wavelength filters and are arranged in a square grid. Such a filter array is called a Bayer filter. An example of a Bayer filter is found in Figure 3.2a. The filter pattern consists of 25% blue, 50% green and 25% red pixels. Therefore it is also referred to as a BGGR filter.

Spectral response

The spectral response of each type of pixel can be measured in terms of its quantum efficiency: the percentage of photons hitting the sensor area that produce charge carriers. In Figure 3.2b it is seen that for each type of pixel the peak in quantum efficiency is found at a different wavelength. The colour of this wavelength corresponds to the name of the colour of the pixel. Out of the three types of pixels, the blue pixels have their maximum quantum efficiency at the lowest wavelength. The lower the wavelength, the lower the diffraction limit of light. Therefore it is beneficial to illuminate the target with a source of blue light (457 nm), and read out only the blue pixels. However, since the camera software does not allow reading out only one type of pixel, this would mean only one fourth of the total number of pixels per area is used effectively. Since half the number of pixels is active in x and in y, the resolution of the sensor would be halved. To get a resolution as high as possible with the standard camera software, the target is illuminated with white light to give a high read out of all pixels.

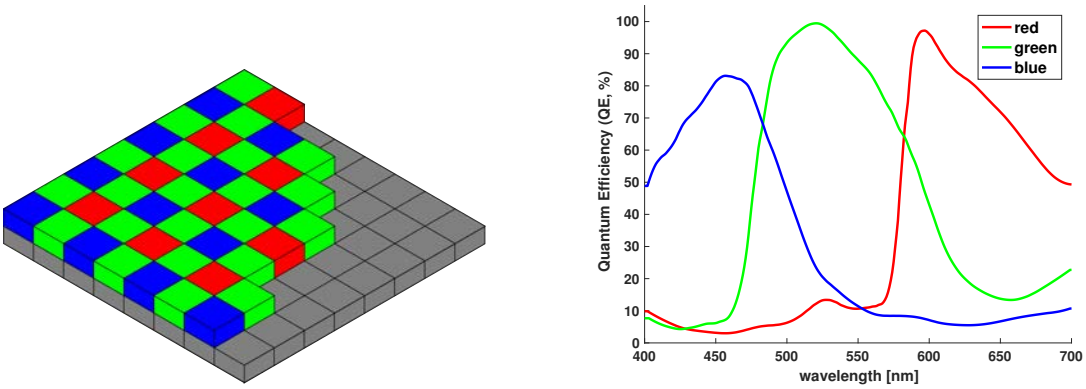

(a) Bayer filter.

(b) Spectral response of the Sony IMX219.

Figure 3.2: (a) Pixel arrangement as a Bayer filter array[a]. The filter pattern consists of 25% blue, 50% green and 25% red pixels. (b) Spectral response of the Sony IMX219 used in the Raspberry Pi camera module V2.1.[b]

[a] `http://en.wikipedia.org/wiki/Bayer_filter`
[b] `https://khufkens.github.io/pi-camera-response-curves/`

3.1.1 Binning and upsampling

The image sensor can be used with different numbers of pixels and sample rates. These settings are known as camera modes. In general, the higher the number of pixels read out, the lower the sample rate and vice versa. When the image sensor is used with standard software at the maximum number of pixels, each pixel is read out and the frame rate is 15 Hz. At a number of pixels of 1280x720 or below, a phenomenon called binning occurs. In binning a number of pixels is read out as one. Since fewer steps are needed, the sensor becomes faster.

During conceptual validation of camera module V1.3 and V2.1 it was found that at a frame rate of 90 Hz, V1.3 performs 4x4 binning, whereas V2.1 performs 2x2 binning. If the maximum number of bins of 640x480 at 90 fps is selected, V1.3 reads out 2560x1920 pixels in bins of 16 pixels, which is almost full field of view. V2.1 however reads out the most central 1280x960 pixels in bins of 4 pixels, with a much smaller field of view. Since the image sensor is supposed to create images with low distortion caused by binning, 2x2 binning is preferred over 4x4 binning and camera module V2.1 was selected.

The field of view can be adjusted by changing the optical system or changed digitally. If a smaller field of view is selected digitally, it was expected that the central pixels are read out without binning, however another phenomenon occurs, called upsampling. This phenomenon was revealed by testing camera V1.3. When a field of view of 25% is selected with an output of 640x480 pixels, it was expected that the sensor would read out the 640x480 central pixels without binning. However, the camera module was found to read out 160x120 bins of 4x4 pixels each, and subsequently upscale this low-resolution data to 640x480 pixels. This phenomenon is also known as digital zoom. Since this effectively reduces the number of pixels, the field of view was adjusted with optics rather than digitally.

3.1.2 Sensor placement

The sensor could be placed above or below the stage, with a target placed correspondingly. Since a controlled environment can be created below the mover, it was decided to place the sensor facing towards the bottom of the mover. The target to be recognised is therefore attached to the bottom of the mover. The target is placed parallel and close to the location of interest for digital microscopy, to keep Abbe errors low. It has the additional advantage that the top of the mover is kept completely free to place the object of interest for microscopic research.

3.2 Target and image recognition

Since the image sensor by itself is not able to detect a position, it is combined with an image-recognition algorithm and a target of which the location can be recognised.

3.2.1 Conceptual sensor system design

First a conceptual design is made for the target to be recognised and the functions that the image-recognition algorithm should fulfil.

Target

Multiple targets could be thought of and the total target size could be either smaller or larger than the total field of view of the image sensor. A simple pattern for 2D position measurement could consist of one black dot placed on a white background. Two dots could be used for 4D position measurement, since three translations and one rotation can be observed. The target has to be smaller than the field of view of the image sensor plus the desired range of motion to be detected. For a desired translational range of 30 mm and 640 pixels this would give a resolution of 47 µm. Since a higher resolution is desired, targets that are larger than the field of view of the image sensor are explored.

Information about the overall position of the target should be present locally. Therefore this information should be available in the field of view of the image sensor. The overall coordinates of the mover could be written on the target with a unique coordinate pair, in the same way the squares of a chessboard are labelled, from A1 to H8. This is an alphanumeric way to code information. A matrix code, also know as a 2D barcode, is a two-dimensional way of representing information. A type of matrix code is used, since these are easier to detect than an alphanumeric code and allow achieving high speed and precision.

Multiple types of 2D barcodes are known, of which the QR-code (Figure 3.3a) is most famous. In image-recognition literature, 2D barcodes are often referred to as (fiducial) markers. Although non-square marker types are proposed in literature, square codes have gained popularity since they allow to extract the position of the marker from its four corners. By placing a number of markers in a square array, a pattern is created. Such a pattern of markers is known as a marker map or marker board, seen in Figure 3.3b. By seeing only one of the markers in the marker map, the absolute position of the pattern can be calculated. The overall position information is extracted from the information stored in the marker, and the local position information is extracted from the orientation of the marker in the taken image. This allows the resolution of

(a) QR-code

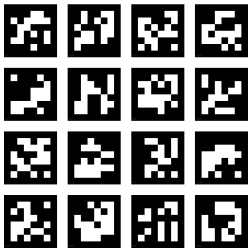

(b) Marker map

Figure 3.3: 2D barcodes (also known as markers) can be used to store information in an array of black and white bits. (a) A QR-code, the most well known type of 2D barcode. (b) By combining multiple markers, a marker map is created.

the sensor to be chosen independently of the range, since only a part of the target has to be seen at each moment.

To calibrate the sensor system, the size of the marker has to be specified to the algorithm. In theory all six Degrees of Freedom could be extracted from a square marker. Changes in the three planar DOFs are recognised due to movement of the marker in the field of view. A change in the out-of-plane translation is recognised if the size of the marker changes. The two remaining rotations are recognised if the shape of the marker changes from square to trapezoidal due to tilt. In this research only the three planar DOFs will be used.

To make sure that one marker is visible at all times, the minimal field of view of the image sensor should be $2\sqrt{2}$ times the size of one marker. The translations cause a factor 2 and a rotation of 45° is responsible for an additional factor $\sqrt{2}$ (Figure 3.4). For robustness of the sensor system, a field of view of four times the size of one marker is chosen. This has the additional advantage that more corner points are available for computing the position, thus the position obtained is less influenced by noise.

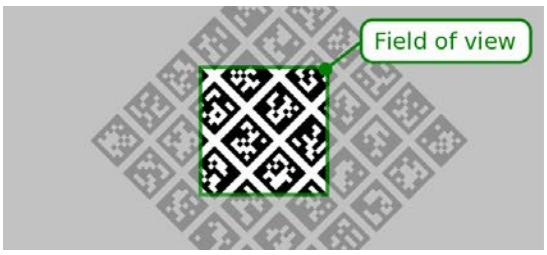

Figure 3.4: Field of view of the image sensor. Theoretically the field of view should be $2\sqrt{2}$ times as large as the size of one marker, to make sure one marker is always visible. For robustness, a field of view of four times one marker is selected.

A small research showed that marker maps are often used in Augmented Reality applications. The marker map is used as a basis for additional items to be shown in the image. Common marker-recognition software packages are ARToolkit, openAR and ArUco. Most of these packages are based on OpenCV (Open Source Computer Vision), a library aimed at real-time computer vision. OpenCV was designed for computational efficiency, which makes it very suited to run on a low-cost microcontroller.

Image-recognition algorithm

To determine the position of the target, a conceptual design was made for the image-recognition algorithm. The steps performed are seen in Figure 3.5. First the colour image is converted to grey-scale. The angle θ is determined by a least squares fit of lines. The position of the markers in the field of view of the image sensor allows the relative position of the target to be determined in x and y. By reading the data stored in the markers within the field of view, the absolute position can be determined in x, y and θ. Based on this conceptual design, literature was studied to find different state-of-the-art marker-recognition algorithms.

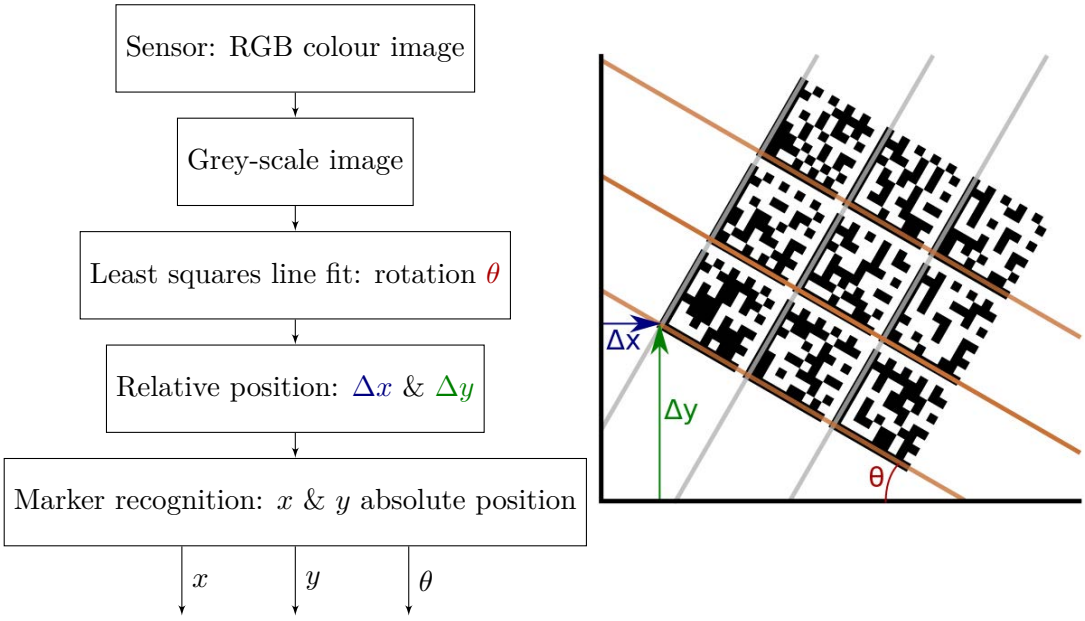

(a) (b)

Figure 3.5: Conceptual design of the image-recognition algorithm. The colour image is converted to grey-scale. The rotation is determined by a least squares line fit. The relative positions in the field of view are calculated. By reading the data stored in the markers, the absolute position of the target is determined.

3.2.2 ArUco target

The ArUco library is available as open source software and has elaborate documentation. The software is created by a research group of the University of Córdoba [5]. On a 2.4 GHz processor with 2048 MB of RAM an average processing time of 11.08 ms/image was found, corresponding to 90 Hz.

Multiple types of marker dictionaries such as ArUco, ARTag and ARToolkit+ (BCH) can be used with the ArUco algorithm. In general, each dictionary contains a predefined set of markers with a unique id. Each marker consists of a black border and an inner area where information is stored in bits.[1] The ArUco MIP36h12 dictionary is recommended for robustness, it however contains a maximum of 250 different markers. The redundancy can be used to detect and correct errors. The ArUco dictionary is

[1] All dictionaries define each marker with 6x6 bits, giving a total number of possible markers of 2^{36}. Since four rotations (0°, 90°, 180° and 270°) are possible, the total number of unique markers is 2^{34}.

selected for its ability to correct errors and its low noise levels compared to ARTag and ARtookit+ BCH.

Since the translational range of motion is square and the maximum number of markers is 250, a marker map of 15x15 markers is created. As the translational range of motion is 30 mm, each marker should have a size including white margin of 2 mm. Taking edge effects of the range into account gives a marker size of 2.5 mm. The marker map (Figure 3.6) has a size of 37.5x37.5 mm, making sure at least one marker is always in the field of view of the image sensor, also at maximum translations.

(a) ArUco marker map **(b)** Printed target

Figure 3.6: (a) The target is an ArUco marker map of 15x15 markers. (b) The marker map is printed with a 1200 DPI printer at a size of 37.5x37.5 mm and placed on the bottom of the mover.

For ease of manufacturing it is important to ensure that the marker can be printed on a commonly used laser printer. Since each marker consists of 6x6 bits for coding, a black border of one bit wide and a white border of approximately one bit wide. Each 2.5 mm consists of 8 bits, or 3.2 bits/mm. For the algorithm to work well, each bit has to be printed with approximately 10 dots of ink, giving a minimum resolution of 32 dots/mm, corresponding to a minimum printing resolution of 813 DPI. A 1200 DPI printer was used to print the target.

By trading robustness of the algorithm for a larger number of markers, the resolution of the sensor system could be increased by printing smaller markers. This would however mean that a normal printer is not suitable, and alternative techniques such as photoplotting or laser engraving should be used. Since the goal of this thesis is to build a demonstrator stage to show it is possible to use an image sensor for precise positioning, these options were investigated but not further pursued. A smaller field of view additionally decreases the maximum speed of the sensor system, since the maximum velocity of the target is limited by the shutter time of the image sensor (≈ 1 ms). Otherwise significant blurring of the image occurs.

3.2.3 ArUco image-recognition algorithm

The ArUco marker-recognition algorithm was implemented. Since the exact working of the algorithm is treated as a black box and is outside the scope of this thesis, only a general description of the steps that are performed by the algorithm is given. The steps as described by [5] are shown in Figure 3.7.

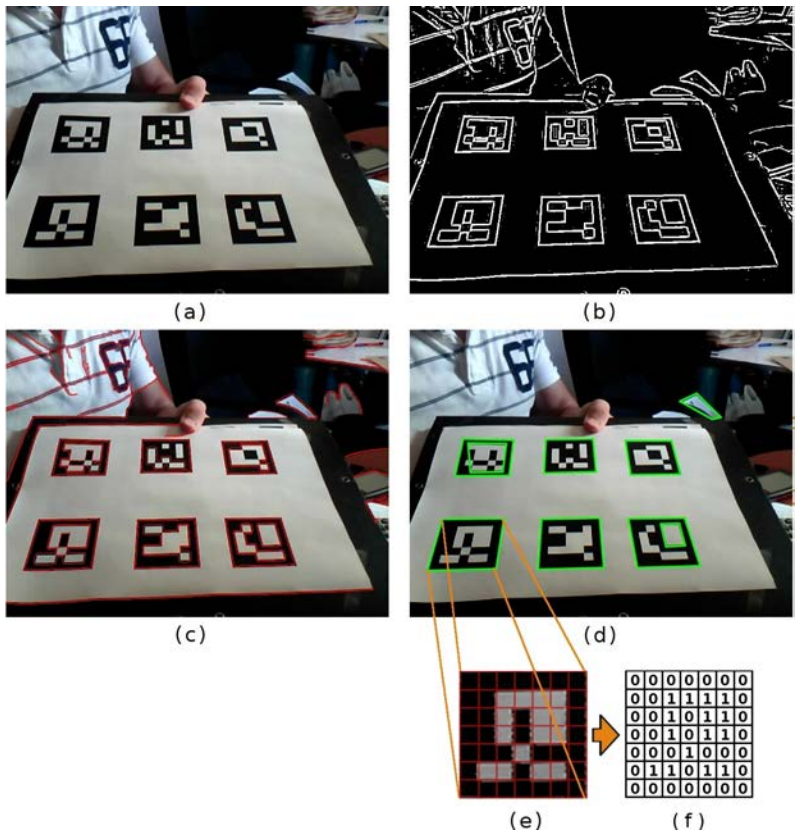

Figure 3.7: Steps performed by the ArUco image-recognition algorithm. (a) Original image. (b) Result of applying local thresholding. (c) Contour detection. (d) Polygonal approximation and filtering of irrelevant contours. (e) Example of marker after perspective transformation. (f) Bit assignment for each cell. [5]

- A **grey-scale** image is made of the original image (a).
- **Image segmentation:** First the most prominent contours in the grey-scale image are extracted (b).
- **Contour detection and filtering:** Secondly the image is thresholded and the contours are detected (c). A polygonal approximation is performed and the polygons that do not approximate to a square shape are discarded. The polygons with exactly four corners are the bases for the markers (d).
- **Marker code extraction:** Next the inner region of the contours are analysed to extract the internal code. The image is flattened and divided into a regular grid (e). For each cell the number of black and white pixels are counted and a value 0 or 1 is assigned to the cell, corresponding to black and white respectively (f). If the bits on the border of the marker are not identified as 0, the image is rejected as a potential marker candidate.
- **Marker identification and error correction:** Now the bits are analysed to determine which of the candidate markers belong to the dictionary and which are part of the environment. Once the code of a marker candidate is extracted, four different id's are obtained, one for each possible rotation. If any of these

four id's corresponds to a marker in the dictionary, the candidate is considered as a valid marker. If no match is found a correction algorithm is applied which can detect and correct erroneous bits.

- **Corner refinement and pose estimation:** Once a marker has been detected, its position and orientation with respect to the image sensor can be estimated. The corners are refined through sub-pixel interpolation, which increases the accuracy of the estimated pose.
- **Refine marker detection for boards:** If only a subset of markers that belong to the board have been detected, the detected markers and the board layout can be used to find the markers that were not detected previously.
- **Board pose estimation:** Now that the pose of each marker is known, an estimate of the pose of the total marker map can be made.

3.3 Optics

Optics are used as the link between the target and the image sensor. This section describes the optical phenomena and their formulas to demonstrate how the lens specifications were calculated.

The target is the object of which an image should be made on the sensor. This could be done by means of a basic pinhole, however a lens system achieves better results in terms of resolution by allowing higher diffraction orders to pass through the optics.

The optical system needs to meet a number of requirements:

- The image length seen by one pixel, defined as the resolution, should be small.
- The magnification should match the dimensions of the field of view to the dimensions of the image sensor.
- The wave nature of light and the associated diffraction phenomena theoretically limit the resolution of an optical system. The diffraction limit is determined by the wavelength of the light and the Numerical Aperture of the lens. These should be chosen appropriately.
- The Depth of Field, defined as the distance between the nearest and farthest objects that appear sharp, should be a couple of millimetres, to make the sensor system robust against a change in height of the mover.

3.3.1 Resolution

Resolution is a term used to describe different phenomena. In image sensor technology it is often used to describe the number of pixels. In precise positioning systems, resolution is defined as the smallest change in position that can be measured by a sensor. In optics, resolution is defined as the image length "seen" by one pixel bin. The last definition is used in this chapter.

For precise positioning, a small resolution is required. For robustness and low noise levels of the algorithm it was decided in subsection 3.2.1 to set the shortest length of the sensor image equal to 4 times the length of one marker. The four markers have a length of 10 mm, and are seen by 120 pixel bins, therefore the resolution of this system is 83 µm.

3.3.2 Magnification

Optical magnification is used to match the size of the object to an image with the size of the sensor. To calculate the magnification, the thin lens formula is used:

$$\frac{1}{f} = \frac{1}{v} + \frac{1}{b} \tag{3.1}$$

where f is the focal length, v is the object distance and b is the image distance.

The magnification M is defined according to the traditional sign convention used in photography: the size of the image, divided by the size of the object. Positive values for f, v and b are real, negative values are virtual [6].

$$M = \frac{b}{v} = \frac{h_\mathrm{i}}{h_\mathrm{o}} \tag{3.2}$$

The target width seen by the image sensor is 10 mm. Validation showed that the field of view of the image sensor is the same for 160x120 bins, as for 1280x960 bins. This optically corresponds to 16x16 binning in case of 120 bins. The target is thus seen by 120 bins of each 16 pixels wide, with a pixel size of 1.12 µm. Therefore the magnification is:

$$M = \frac{120 \cdot 16 \cdot 1.12\,\mu\mathrm{m}}{10\,\mathrm{mm}} = 0.22 \tag{3.3}$$

3.3.3 Diffraction limit and Numerical Aperture

The resolution of an optical system can be limited by factors such as lens imperfections or misalignment. Due to the wave nature of light and the diffraction associated, however, the theoretical resolution of an optical system is determined by the number of diffraction order of light that are able to pass through the optics. When light from a point of the object passes through the optics and is reconstructed as an image, the point of the object appears in the image as a small pattern known as Airy disc, due to the diffraction of light. Low diffraction orders allow large features to be reconstructed. High diffraction orders allow small features to be distinguished. This resolution limit is also know as Abbe resolution d_Abbe and is calculated with:

$$d_\mathrm{Abbe} = \frac{\lambda}{2n\sin\alpha} = \frac{\lambda}{2\mathrm{NA}} \tag{3.4}$$

where λ is the wavelength of the light, n is the index of refraction of the medium and $n\sin\alpha$ is called the Numerical Aperture (NA). The angle α is defined as:

$$tan(\alpha) = \frac{\frac{d}{2}}{v} \tag{3.5}$$

where v is the object distance and d is the aperture diameter. The relation between the NA, angle α and size of the Airy discs is seen in Figure 3.8.

It is important to notice that the maximum value of α is 90° and that n is defined by the medium. Oil has a larger value of n than air. Therefore the NA of an optical system can be increased by using oil instead of air. For this demonstrator air is chosen for ease of implementation.

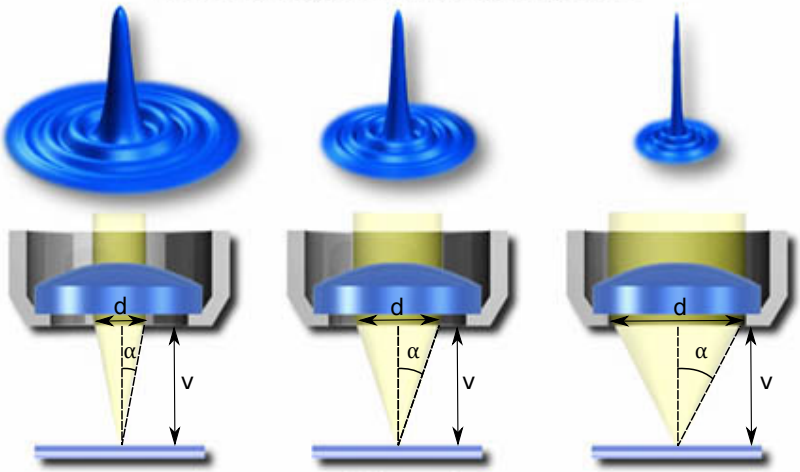

Figure 3.8: In these figures[a] the same lens is used and the object distance v is constant. The aperture diameter d is adjusted to change the Numerical Aperture. The Numerical Aperture increases from left to right, and the Airy disc size is seen to decrease with NA. With a higher Numerical Aperture, smaller features can be reconstructed.

[a] `http://www.olympusmicro.com/primer/anatomy/numaperture.html`

Although the limits imposed by diffraction are not reached with this system, for scaling it is important to know the theoretical limit in resolution caused by the optical system.

3.3.4 Depth of field

Since the height of the mover may vary, the sensor should be able to capture sharp enough images in a large range of heights. In optics this range is defined as the Depth of Field (DoF), also known as focus range. It is the distance between the nearest and farthest objects in a scene that appear acceptably sharp in an image.

According to the thin lens formula, an object should be placed precisely in at a distance v from the lens. In reality the object might however be slightly nearer or farther from the lens. This prevents light rays from the object to focus perfectly on the image and creates a circle of confusion c, also known as circle of indistinctness, disk of confusion, blur circle, or blur spot.

In photography, instead of Numerical Aperture, another measure of the angular aperture is typically used, called "working f-number" or "effective f-number" N_{w}:

$$N_{\mathrm{w}} = \frac{v}{d} = \frac{1}{2sin\alpha} \tag{3.6}$$

The working f-number can be related to the Numerical Aperture:

$$N_{\mathrm{w}} = \frac{n}{2\mathrm{NA}} \tag{3.7}$$

where n is the index of refraction.

According to [7], for a symmetrical lens, the Depth of Field can be calculated with:

$$\mathrm{DoF} = \frac{2vf^2Nc(v-f)}{f^4 - N^2c^2(v-f)^2} \tag{3.8}$$

where N is f-number, which has a slightly different definition than N_{w}: $N = \frac{f}{d}$. Assuming $N^2c^2(v-f)^2$ is small compared to f^4 yields:

$$\mathrm{DoF} = \frac{2vNc(v-f)}{f^2} \tag{3.9}$$

For this system it corresponds to within 0.14 % of the non-simplified formulation. A larger Numerical Aperture leads to a smaller Depth of Field and a linear relationship between f-number N, circle of confusion c, and Depth of Field DoF is shown. The relationship between Depth of Field and circle of confusion is also seen in Figure 3.9.

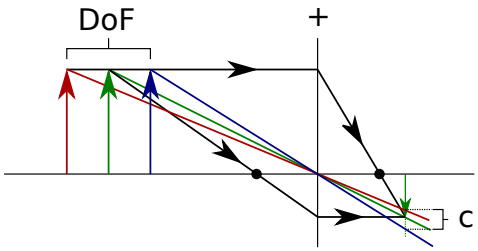

Figure 3.9: The relation between Depth of Field (DoF) and circle of confusion (c). The circle of confusion increases with Depth of Field.

3.3.5 Trade-off diffraction limit and depth of field

As can be seen from the two previous sections, the Abbe resolution becomes smaller with increase in Numerical Aperture, however, the circle of confusion becomes larger with increasing Numerical Aperture, for a constant Depth of Field. This leads to a trade-off between diffraction limit and Depth of Field.

Multiple lens systems were optically tested, including systems consisting of multiple lenses in series. It was however seen that the standard lens that comes with the Raspberry Pi camera module is of high quality and gives small image distortion. It also has a small focal distance, which keeps the total length of the optical path short, which is desirable for a compact standalone system. The lens has a focal length of approximately 3.5 mm and an aperture diameter of approximately 1.25 mm.

The diffraction limit of this optical system is 11.1 µm. A theoretical Depth of Field of 1.47 mm can be achieved, with a circle of confusion of 10 µm. The circle of confusion is much smaller than the pixel resolution of 83 µm. Therefore, this system is not optically limited. For a design using a larger magnification and smaller markers, a trade-off between Abbe resolution, circle of confusion and Depth of Field should be made.

The DoF was measured by attaching the image sensor to a linear stage. The setup is shown in Figure 3.10b. This allowed the distance of the sensor to the target to be adjusted and measured. The output of the sensor algorithm was checked for a range of positions. The DoF is measured as the difference between the minimum and maximum distance that still gave a correct output.

3.3.6 Specifications of the optical system

The specifications of the optical system are listed in Table 3.2.

Table 3.2: Specifications of the optical system

sensor resolution		83 µm
maximum sensor frame rate		90 Hz
object size: 4 markers		10 mm
image size		2.2 mm
magnification	M	0.22
lens focal length	f	3.5 mm
aperture diameter	d	1.25 mm
object distance	v	19.8 mm
image distance	b	4.3 mm
total optical path length	$v+b$	24.0 mm
Numerical Aperture	NA	0.032
f-number	N	2.8
working f-number	N_{w}	15.8
wavelength used for d_{Abbe}	λ	700 nm
Abbe resolution	d_{Abbe}	11.1 µm
circle of confusion accepted	c	10 µm
Depth of Field calculated	DoF	1.47 mm
Depth of Field measured	DoF	3.96 mm

3.4 Validation

In order to measure the performance of the standalone sensor system two tests were done. The tracking capability and the measurement dispersion were tested for different numbers of pixel bins. The target was placed on a motion-controlled stage in an experimental setup. The Thorlabs DDSM-100/M stage was used, since it has a range of 100 mm, a resolution of 0.5 µm and a maximum speed of 500 mm/s. The position of the Thorlabs stage is controlled from a PC, and interfaces with a position controller using a quadrature encoder. To make sure the position output of the sensor system and the position of the stage was synchronously measured, a NI-DAQ 6211 data acquisition unit was used to simultaneously log the four quadrature encoder signals and the x-position measured by the sensor system. The quadrature signals were converted into a position in Matlab afterwards. To make the x-position measured by the sensor system available as an analog input for the data acquisition unit, an Arduino was used since it has an Analog to Digital Converter (ADC) converter. The Raspberry sent the measured x-position to the Arduino using a Serial Peripheral Interface (SPI) communication protocol. The schematic overview and the implementation of the measurement setup is seen in Figure 3.10.

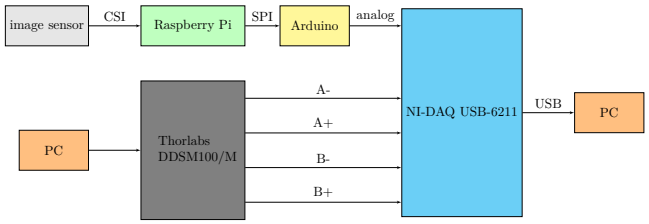

(a) Schematic setup

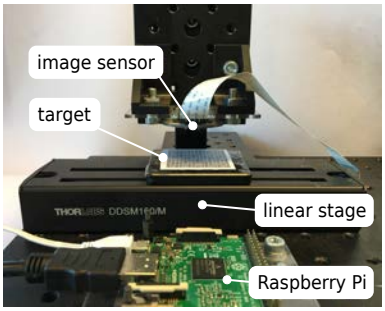

(b) Measurement setup

Figure 3.10: Measurement setup for validation of sensor system specifications. (a) Schematic setup. The quadrature position output of the Thorlabs stage is measured with a NI-DAQ USB-6211. An Arduino is used to convert the digital signal on the Raspberry Pi into an analog signal. (b) Measurement setup. The target with markers is placed on top of a Thorlabs DDSM100/M linear stage programmed to translate. The image sensor is placed above the target and connected to the Raspberry Pi. Wiring is removed for clarity.

3.4.1 Number of sensor bins

Different numbers of pixel bins can be read from the sensor. Images were taken from the same part of the target, where 10 mm of the target is seen by 60, 120, 240, 480, and 960 bins. These images are seen in Figure 3.11. A red line of one bin wide is drawn around each of the identified markers. The id's corresponding to each of the identified markers are shown in blue. In the image with 60 bins the number of bins is only a factor 1.5 larger than the 40 bits of the marker and the algorithm is not able to recognise the markers. For an increased number of bins, more bins are used to capture the same 10 mm and the images become sharper.

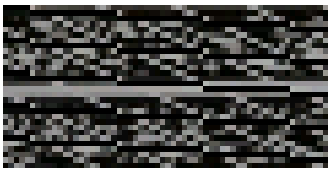

(a) 60 bins

(b) 120 bins

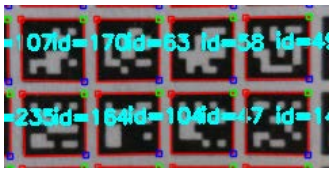

(c) 240 bins

(d) 480 bins

(e) 960 bins

Figure 3.11: Images of the same optical setup, taken with different numbers of pixel bins. The total width of four markers is 10 mm. Images are cropped to a size of 2:1. The largest number of bins in each image is 60, 120, 240, 480 and 960. The markers are identified by the image-recognition algorithm. The algorithm adds the id's corresponding to each of the identified markers in blue and draws a red line of one bin wide around them. The algorithm is not able to recognise the markers in the image with 60 bins. For an increased number of bins, the images become sharper.

3.4.2 Calibration

The sensor system was calibrated before the measurements were done, to make sure that a position displacement of the stage of 30 mm gives a sensor system output of 30 mm.

First the lens distortion coefficients were calibrated with a calibration program provided in the ArUco library. Next the output of the sensor system was measured at two locations defined by the stage. This calibration yielded a factor that was corrected for.

3.4.3 Measurement dispersion

The sensor measurement of one position does not yield only one value, but a distribution of measurements. In statistics, dispersion is a measure for the extent to which the distribution is stretched and squeezed, and can be expressed in terms of standard deviation σ. The results for four different numbers of pixel bins are found in Figure 3.12 and Figure 3.13. The unfiltered and filtered data is compared in Figure 3.14.

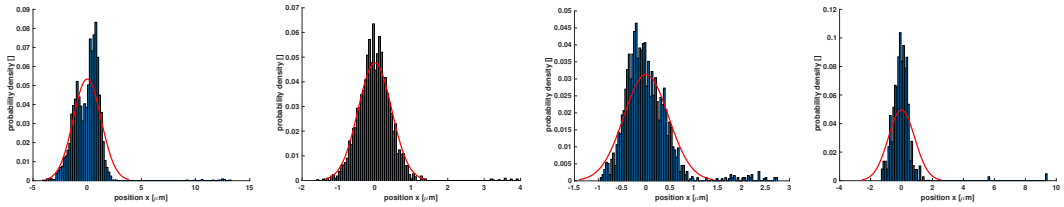

(a) 160x120: $3\sigma = 3.9\,\mu m$ **(b)** 320x240: $3\sigma = 1.4\,\mu m$ **(c)** 640x480: $3\sigma = 1.4\,\mu m$ **(d)** 1280x960: $3\sigma = 2.6\,\mu m$

Figure 3.12: Translational measurement dispersion for four different numbers of pixel bins. Outliers with positive sign increase the measurement dispersion. No explanation has been found for these outliers.

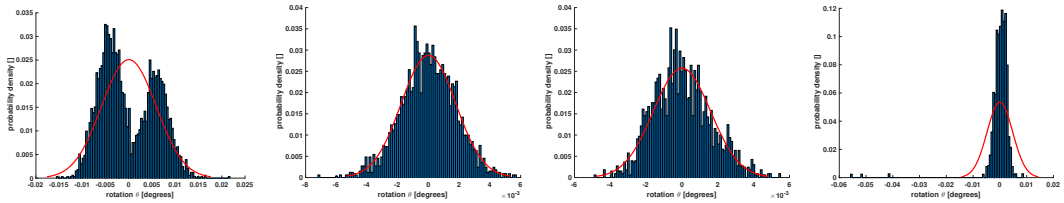

(a) 160x120: $3\sigma = 0.0177°$ **(b)** 320x240: $3\sigma = 0.0053°$ **(c)** 640x480: $3\sigma = 0.0048°$ **(d)** 1280x960: $3\sigma = 0.0143°$

Figure 3.13: Rotational measurement dispersion for four different numbers of pixel bins. Mark that the measurement for 160x120 bins displays two peaks rather than one. For this behaviour no explanation has been found.

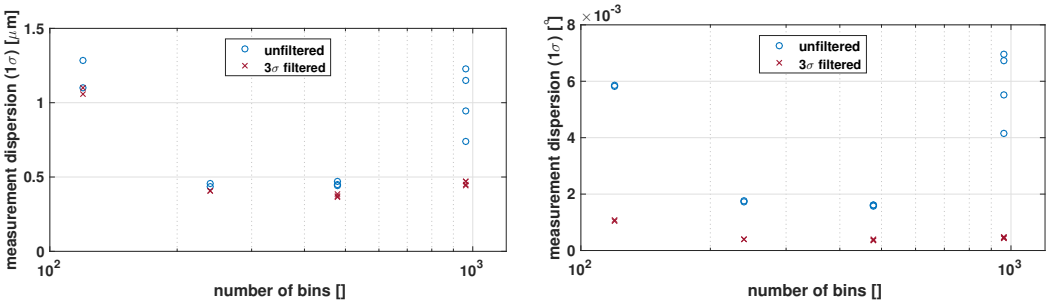

(a) Translation **(b)** Rotation

Figure 3.14: 1σ measurement dispersion for translation and rotation for different numbers of pixel bins. The optical magnification and the field of view (10 mm) are held constant. Unfiltered data is displayed in blue. The data is also filtered by rejecting the outliers larger than 3σ. The 1σ measurement dispersion of the filtered data is shown in red. The 1σ dispersion of the filtered data is below 0.5 µm for a number of pixel bins larger than 240. The unfiltered data however has outliers that significantly increase the measurement dispersion for 960 pixel bins.

3.4.4 Tracking

The tracking capabilities of the sensor system were measured by moving the stage from −15 mm to 15 mm with a constant velocity of 30 mm/s, followed by the opposite movement with a constant velocity of −30 mm/s. The results are seen in Figure 3.15. The noise on the sensor signal can be mainly attributed to the ADC of the Arduino. Two phenomena are observed:

- The sensor system signals are delayed.
- The sample rate of the sensor system causes a zero-order-hold (ZOH) behaviour of the signal.

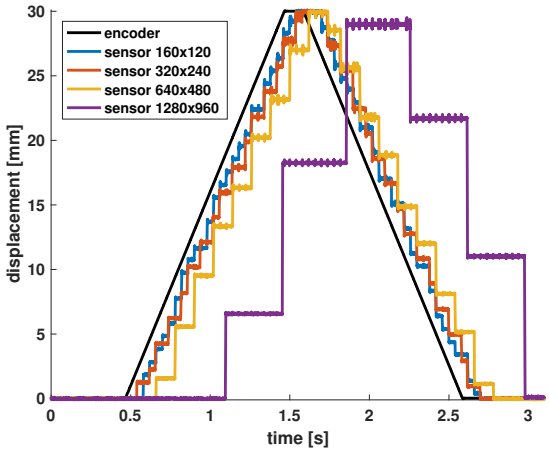

Figure 3.15: Translational ramp tracking for different numbers of pixel bins. The sensor signal is delayed and has a sample rate that depends on the number of bins. This is mainly caused by the image-recognition algorithm that uses time to process the images.

Therefore additional measurements are performed, to determine the sensor system delay and corresponding sample rate for different numbers of pixel bins.

3.4.5 Delay and sample rate

The delay and sample rate were measured with timers in the sensor system algorithm C++ script. The results are found in Figure 3.16. The delay increases with number of bins. The average delays are 60 ms, 75 ms, 150 ms and 450 ms, respectively. The sample rate is inversely proportional to the delay and therefore decreases with number of pixel bins. To compensate for the sensor system delay, an advanced controller using a Smith predictor is proposed in chapter 6.

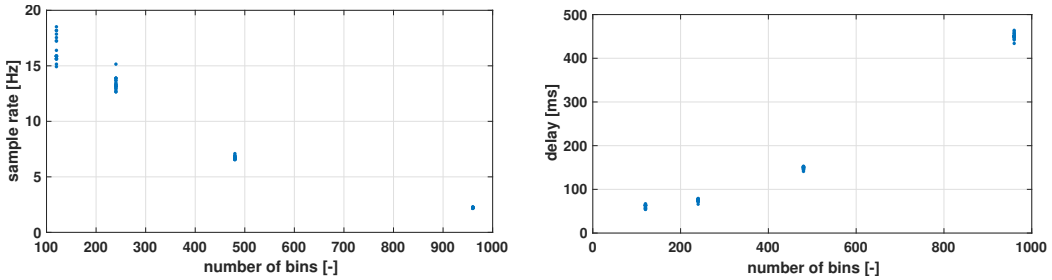

(a) Sample rate **(b)** Delay

Figure 3.16: Sample rate and delay for four different numbers of pixel bins. The sample rate decreases and the delay increases with number of pixel bins.

3.4.6 Trade-off measurement dispersion and sensor delay

As measurement dispersion and sample rate decrease with the number of pixel bins, a trade-off should be made between these two parameters to select the desired number of bins.

Since the sensor system is used for position feedback in a control scheme, the controller bandwidth should be high enough to reject disturbances. In the conceptual design a requirement of 10 Hz was derived. In order to assess the stability, the expected open-loop response of a Proportional and Derivative (PD) controller C, the plant G, and the sensor delay H is modelled. The controller is designed to create a bandwidth of 10 Hz of the system without delay. The phase of the open-loop response is shown in Figure 3.17 for the system without sensor delay, and with the average sensor delays corresponding to 120, 240, 480 and 960 pixel bins. When the phase of the open-loop response crosses $-180°$ the system becomes unstable. This reduces the bandwidth of the controller to 4.2 Hz for the lowest number of pixel bins, without controller stability margins. The control bandwidth could be increased slightly by tuning the controller phase gain to reach its maximum below the frequency where the phase crosses $-180°$. To approach the desired bandwidth of 10 Hz as close as possible, it was decided to use the lowest number of pixel bins that can still recognise the markers.

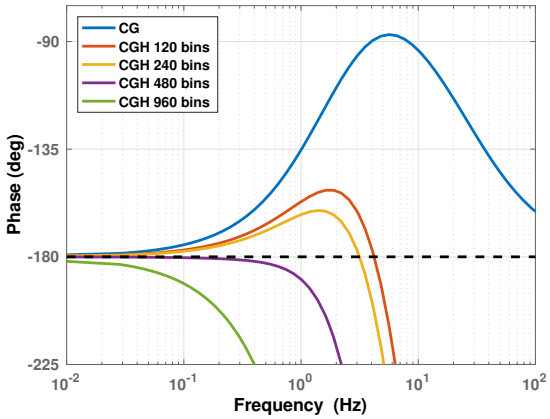

Figure 3.17: The open-loop transfer functions of the controller C, plant G, and the delay induced by the sensor system algorithm H, for different amounts of pixel bins. The controller is tuned for a bandwidth of 10 Hz for the system without delay (CG). The closed-loop response of the system will become unstable when the phase of the open-loop crosses $-180°$. The time delay therefore limits the bandwidth of the control system. To approach the desired bandwidth of 10 Hz as close as possible, it was decided to use 120 bins.

3.5 Specifications of the complete sensor system

Table 3.3: Specifications of the complete sensor system

number of pixel bins	160x120
sensor resolution without pixel interpolation	83 µm
sensor measurement dispersion with pixel interpolation (3σ)	3.9 µm & 0.0177°
maximum tested speed	480 mm/s
average sample rate	16 Hz
average time delay	60 ms
depth of field	3.96 mm

3.6 Conclusion

By combining the image sensor with a target of markers, the range of the sensor system is decoupled from its resolution. Optics were designed to match the size of four markers to the size of the sensor. A trade-off has to be made between the resolution and sample rate of the image-recognition algorithm. For a high number of pixel bins, sharp images with low measurement dispersion are obtained. However, the higher the number of bins, the lower the sensor signal sample rate. For control bandwidth, the lowest number of pixel bins that can still detect the markers was selected.

4

Actuator

The actuator is used to position the region of interest into the field of view of the microscope. The actuator is based on the Lorentz actuation principle and consists of a stator that is stationary and a mover. The stator contains coils embedded in a PCB. Magnets are part of the mover, which is placed on top of the stator. Multiple coils are used to create forces that are combined to motion the mover in x-, y- and θ-direction. A planar ferrofluid bearing is used between the mover and the stator, to allow for planar movements and constrain the remaining three DOFs. In this chapter the conceptual design of the actuator is presented, followed by the magnetic design of the mover and bearing, and the electric design of the stator. Finally the forces developed by the actuator are calculated and validated.

4.1 Conceptual actuator design

Lorentz forces generated by the actuator position the mover in plane with respect to the stator. Permanent magnets are used as source of flux to limit the amount of parts needed to generate the magnetic field. The conceptual design is shown in Figure 4.1 and Figure 4.2.

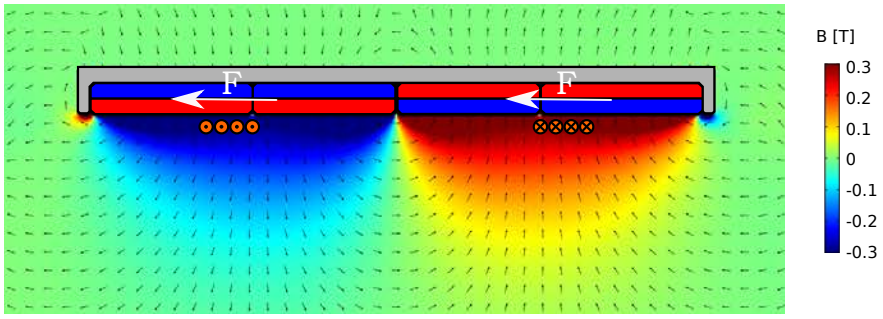

Figure 4.1: Cross-section of the conceptual actuator design. The magnetic field B_z of the mover creates a Lorentz force on the windings. The current direction is indicated by crosses and dots in the windings. The Lorentz force is determined by the right-hand rule. Reaction forces in opposite direction are acting on the mover. Since the windings are stationary, the mover will accelerate sideways.

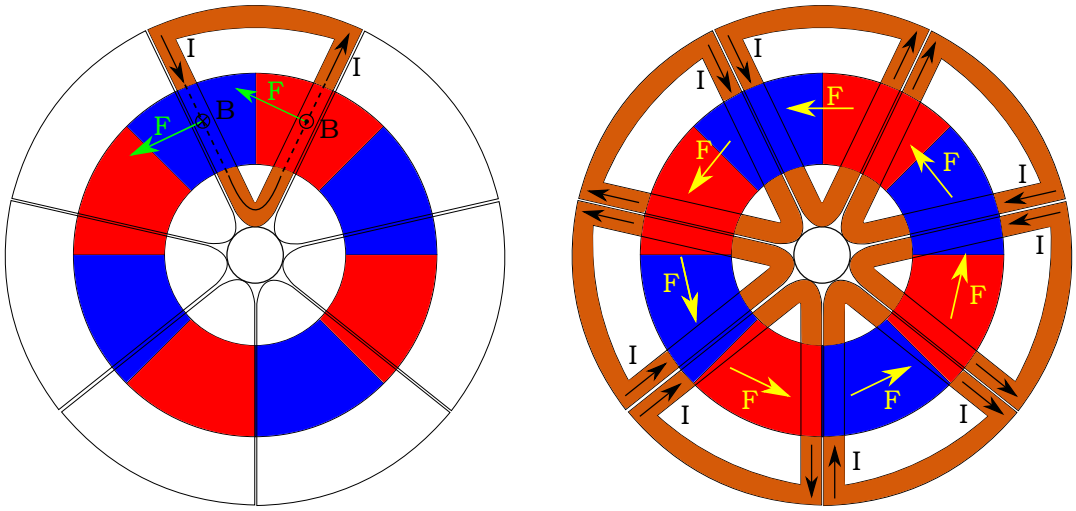

(a) (b)

Figure 4.2: Top view of the conceptual actuator design. (a) Each coil consists of two straight "legs" and two sections connecting the legs on the top and bottom. A current through the coil creates a Lorentz force on each leg of the coil. Since the coils are stationary, a reaction force with the same magnitude but opposite direction is created on the mover. The forces acting on the mover are shown in green. (b) The two forces generated by each coil can be combined into one total force per coil, shown in yellow. By adjusting the current through each coil and combining the forces of different coils, a net force or torque can be exerted on the mover. In this case a pure torque is created.

4.1.1 Literature

Multiple types of permanent magnet motors are known in literature, divided in the categories radial flux and axial flux. For planar positioning, an axial flux permanent magnet motor (AFPMM) is most suited, since the distance between the coils and magnets can be kept constant for all planar positions. The flux of the magnetic poles is thus directed perpendicular to the plane of motion.

The literature lists a number of different axial flux permanent magnet motors types: single rotor single stator, double rotor single stator, single rotor double stator and multi rotor multi stator [8]. Multi stator configurations are not suited for this application since it prescribes the stator to be placed on both sides of the mover. In the present configuration however, one side of the mover should be kept free to place an object of interest. A single and double rotor configuration were analysed. For consistency with literature, in this chapter, the mover is sometimes referred to as *rotor*. In the rest of the report, the rotor will be referred to as mover.

Axial flux designs conventionally have a ball bearing preventing planar translations. However also bearingless AFPMM designs can be found in literature, which do not restrict planar translations. These systems are conventionally limited to small translations [9] [10].

4.1.2 Power losses

For the standalone system low power consumption is preferred. Heat causes thermal expansion which is not desired for precise positioning, therefore low heat generation

is required. Power losses are related to current by:

$$P = I^2 R \tag{4.1}$$

Therefore it is important that the required forces and torques can be produced with low currents. The force per unit current is known as motor constant.

4.1.3 Lorentz force

The Lorentz force is calculated with:

$$\mathbf{F} = l \cdot \mathbf{I} \times \mathbf{B} \tag{4.2}$$

where $\mathbf{F}$ is the Lorentz force, l is the length of the coil in the magnetic field, $\mathbf{I}$ is the current and $\mathbf{B}$ is the magnetic flux density. For a twice as high Lorentz force, a twice as high current is needed, corresponding to four times higher heat generation.

4.1.4 Conceptual analysis

To achieve high motor constants and low heat generation, an analysis of different concepts was performed. 60 concepts with different numbers of magnet poles and coils were evaluated. Three concepts can be seen in Figure 4.3. A simplified model is used to calculate the motor constants that the actuator can generate at every rotational position, when the mover is positioned in the middle of the stator. Different combinations of mover and stator configurations were evaluated. The number of magnet poles m was varied between 2 and 12. Since a magnet ring is used, only even numbers of poles were considered. The number of coils n in the stator was varied between 3 to 12.

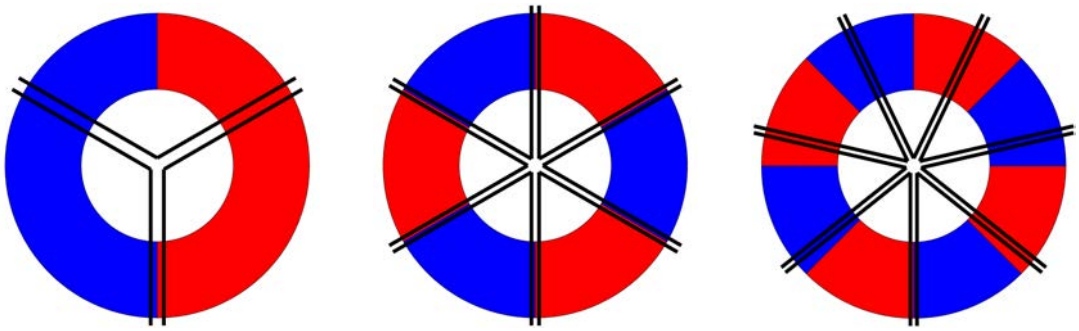

(a) 2 poles and 3 coils **(b)** 6 poles and 6 coils **(c)** 8 poles and 7 coils

Figure 4.3: Three actuator concepts. A red segment is a magnet pole with its north pole facing up; a blue segment is a magnet pole with its north pole facing down. The black lines indicate the location a coil consisting of an infinitely thin single winding. (a) Basic concept with 2 magnet poles and 3 coils. (b) Concept with 6 poles and 6 coils. (c) Concept with 8 poles and 7 coils. Using this simplified model, a conceptual analysis of different combinations of coils and poles was performed.

The minimum forces F_{x}, F_{y} and torque T_θ at all rotational positions were calculated for every concept. These values are shown in Figure 4.4. The minimum motor constants at every location were calculated by dividing the force by the total currents. These are shown in Figure 4.5.

A higher number of windings increases the force, because in total more current can

be applied to the stator[1] and the forces are better aligned with the required direction.

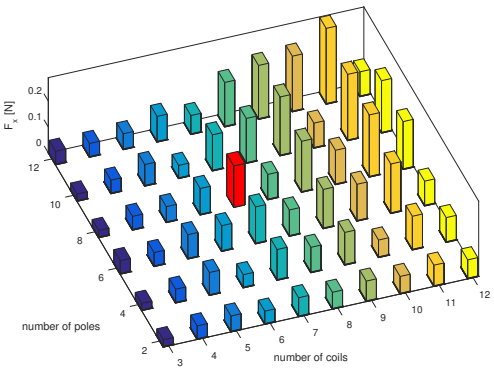

(a) F_x

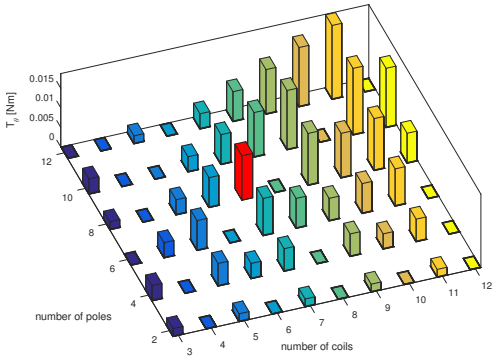

(b) T_θ

Figure 4.4: 60 different actuator concepts were evaluated. The minimum force (a) and torque (b) of a full rotation θ around $(x, y) = (0, 0)$ are displayed. The number of coils in the stator was varied between 3 and 12, and even pole numbers in the mover from 2 to 12 were evaluated. Using these figures, design guidelines were established. The red bar indicates the concept with 8 poles and 7 coils that was selected. It delivers high forces and torques, with a low number of coils.

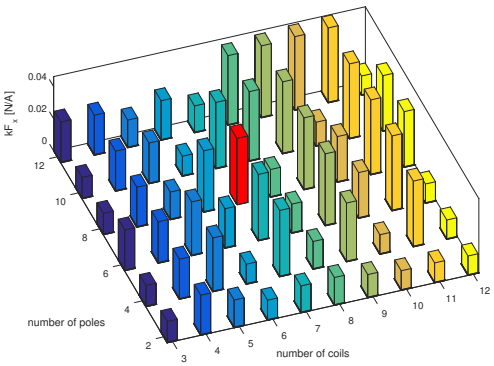

(a) kF_x

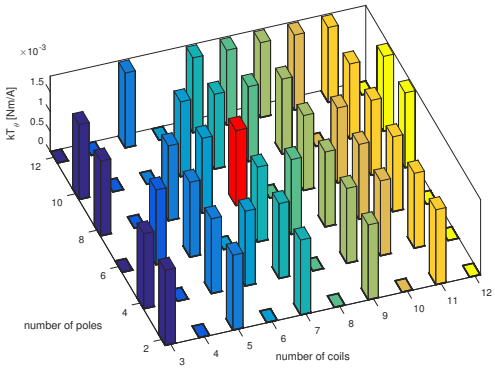

(b) kT_θ

Figure 4.5: The minimum motor constants for translation (a) and rotation (b) of a full rotation θ around $(x, y) = (0, 0)$. The red bar indicates the selected concept with 8 poles and 7 coils.

4.1.5 Model limitations

The simplified model has a number of limitations:

- The magnetic flux density is assumed to be constant over the surface of the mover. Only the sign of the magnetic flux is changed when the coil is under a south pole instead of under a north pole.
- Each coil in the model consists of one winding with infinitely small diameter. This could cause the force generated by a coil to be zero when the coil is precisely in between two magnets. To partially solve this simulation limitation, each coil has an opening angle that is 2° smaller than theoretically possible. For instance for three coils, the opening angle of each coil could be 120°, it is however set to 118°. Additionally the coils are translated by a small amount, as seen in

[1]This effect is compensated for in the motor constants.

Figure 4.3, to make sure the coils never fully align with the rotor at the central position.
- The motor constants at locations different than the central position are not evaluated.
- The number of coils in the actuator does not influence the actuator area available for each coil. Therefore more coils is always better, since some coils will have their force acting already in the correct direction, but the corresponding increase in resistance (due to smaller area available to place coils) is not directly taken into account.
- The model does not consider whether the two other degrees of freedom are balanced. For instance, when a torque is generated with a 2/3 magnet/coil configuration, the forces are not balanced in x- and y-direction. For a 4/3 configuration the forces are balanced, since each coil generates an equal force under 120° angles.
- Only configurations are considered that can be produced in a single two layer PCB, since these can be produced cost-effectively.

4.1.6 Design guidelines

The result of this analysis is a number of design guidelines:

- The number of magnet poles m divided by the number of stator coils n, and vice versa, should not be equal to an integer value. In these cases, for certain rotations of the mover, no torque can be generated. This causes a lock of the rotor.
- For high motor constants, the number of magnet poles should be chosen one larger or smaller than the number of coils. i.e. 6 or 8 magnets in case of 7 coils.
- For high forces and $n > 3$, and for high torques, the number of magnet poles should be chosen one higher than the number of coils. i.e. 6 magnets and 5 coils or 8 magnets and 7 coils. Each coil now "sees" one north and one south pole.

4.1.7 Final trade-off

Based on the design guidelines and a number of different considerations, a trade-off is made to select the number of magnet poles and coils. The trade-off takes into account the required force, amount of damping, robustness to tilt, commutation, number of amplifiers required and market availability:

- a higher number of coils gives a higher amount of force;
- a higher number of poles increases the amount of damping, due to the additional ferrofluid that accumulates where a north and south pole meet;
- for a higher number of poles, commutation has to be performed more often;
- a higher number of poles increases tilt stability of the rotor around the x and y axes;
- for each coil a separate voltage or current controller is necessary;
- magnet segments of 22.5° with a size that allows a target of 30x30 mm to be placed in the centre of the magnet ring are commercially available.

The result of the trade-off is 8 magnet poles and 7 coils. Two off-the-shelf magnet segments of 22.5° are used per magnet pole of 45°. A number of coils greater than

three creates an over-actuated system. This is beneficial for large translations as some motor constants decrease when large translations occur. These position-dependent motor constants will be evaluated for the final design and shown in subsection 4.4.1.

4.1.8 Mover and stator dimensions

The target has a size of 37.5x37.5 mm, thus a diagonal of 53 mm. Since the target should be kept clean of ferrofluid, it is placed inside the magnet ring. Therefore the magnet ring should have an inner diameter larger than the target diagonal. The smallest ring that can be formed around the target with off-the-shelf magnets, has an inner diameter of 60 mm and an outer diameter of 120 mm. This determines the size of the mover.

The size of the stator is chosen such that each magnet pole only "sees" the straight part of a coil. The straight parts of the coils should thus have a length equal to the length of one segment (30 mm) plus the required translation of the mover (30 mm). This gives a diameter of the stator of 150 mm.

4.2 Mover design

The mover consists of a ring of eight alternating magnet poles. Each pole of 45° consists of two magnet segments of 22.5°. The mover design is seen in Figure 4.6.

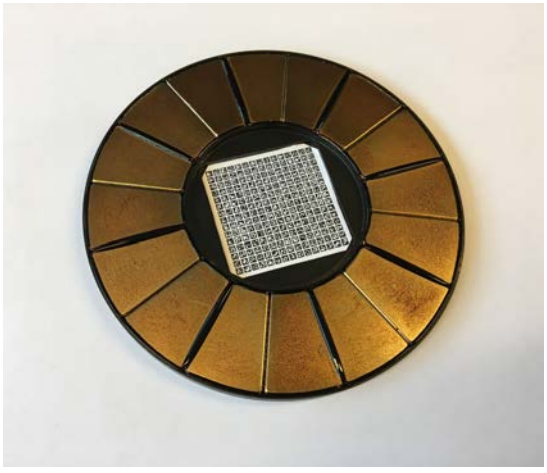

Figure 4.6: The final mover seen from the bottom. 16 magnet segments are used to create eight magnet poles. The target used for position recognition is placed in the centre of the magnet ring.

4.2.1 Bearing system

The bearing system should allow the mover to be positioned to its desired planar position and restrict the remaining three DOFs. The mover needs to move with low or no friction for precise position control.

Bearing concepts

Different bearing concepts could be suited to meet this purpose. Teflon contacts would be the easiest solution, however Gihin Mok [2] has shown that this introduces stick-slip behaviour, which is difficult to control. Hydrostatic bearings alternatively

are known for their low stick-slip and are based on a fluid such as oil, water or air. An air bearing is undesirable for this application since additional equipment is needed to pressurise air. A water bearing was created that uses the hydrophilic properties of a base surface and the hydrophobic properties of teflon. Under load, water is displaced and the hydrophobic behaviour of teflon creates a pressure that increases the load capacity of the bearing. However, the load capacity appeared to be too low for this application. In order to create a higher load capacity, it was decided to use a hydrostatic bearing based on ferrofluid.

Ferrofluid

Several projects about the design of ferrofluid bearings have been conducted in recent years in the research group. The work by Van Veen [4], Café [1] and Lampaert [11] was used for the design of the planar bearing.

Ferrofluid consists of nanometre-size ferromagnetic particles suspended in a liquid carrier, usually oil. Ferrofluid brought into contact with a permanent magnet, collects at the corners of that magnet, the locations of highest magnetic field intensity (Figure 4.7). The ferrofluid can be used to seal a pocket of air. This pocket of air acts as a load carrier. Since permanent magnets will be used for the mover, ferrofluid can be placed on the same magnets as used by the Lorentz actuator. This synergy allows for a low number of parts and a low mass of the mover.

Figure 4.7: One magnet segment of 22.5° with ferrofluid. The ferrofluid collects at the corners of the magnet and can seal a pocket of air, creating a planar bearing.

Load capacity

The load capacity created by the air pocket depends on the surface area of the pocket and the pressure that the ferrofluid can withstand before it collapses. A safe assumption for a robust design is 50 mbar [4]. This gives a load capacity of 42 N.

Vertical height, tilt and trail formation

The vertical height of a ferrofluid bearing can change due to its vertical stiffness and trail formation.

The stiffness of a ferrofluid bearing is lower than that of teflon contacts, which causes a height variation of the mover with different loads. Previously developed ferrofluid bearings have a vertical stiffness in the order of 1×10^4 N/m. Due to variation of the mass of the object (0 to 100 g), the maximum variation in height would be 100 µm.

Additionally the mover may tilt if the load is not placed in the middle of the mover.

When the mover is translated, a part of the ferrofluid remains behind. This phenomenon is called trail formation and causes the height of the bearing to decrease. This effect is about 2 µm per mm translation [4]. With a total range of 30 mm, this gives an additional height variation of 60 µm. If the mover remains at a specific location for several minutes, the ferrofluid returns to its preferred location on the magnets and the height of the mover restores back to its original position.

The position output of the sensor system is independent of height, since the size of one marker is known by the image-recognition algorithm and is compensated for. The circle of confusion however increases when the mover is above or below the focal plane of the bearing, which could cause the image to be blurred. Since this would cause the sensor algorithm to stop, it is important to keep the mover within the Depth of Field of the sensor system. The stiffness of the bearing is increased compared to ferrofluid bearings in literature, by increasing the surface area of the bearing. The trail formation can be compensated for by pre-wetting the surface: depositing a layer of ferrofluid before a measurement is done. However, for a robust system, the Depth of Field of the sensor is designed larger than the expected maximum 160 µm, making a start-up sequence for pre-wetting the surface unnecessary.

Damping

The oil of the ferrofluid system creates damping when the mover is translated and rotated. Research by Lampaert [11] has shown how the planar damping coefficients c and C can be calculated. For translation the damping c can be calculated with:

$$c_{\mathrm{x}} = \frac{F_{\mathrm{x}}}{\dot{x}} = \eta_{\mathrm{r}}\eta_{\mathrm{b}}\frac{A_{\mathrm{bearing}}}{h_{\mathrm{bearing}}} \tag{4.3}$$

where A_{bearing} is the total surface area of the ferrofluid in contact with the stator and h_{bearing} is the fly height of the bearing. η_{b} is the viscosity of the ferrofluid. η_{r} depends on the hydrostatic behaviour of the bearing: when trail formation takes place $\eta_{\mathrm{r}} \approx 4$, without trail formation $\eta_{\mathrm{r}} \approx 1$.

For rotation, the damping coefficient C can be calculated similarly:

$$C_{\theta} = \frac{T_{\theta}}{\dot{\theta}} = \eta_{\mathrm{r}}\eta_{\mathrm{b}}\frac{J_{\mathrm{bearing}}}{h_{\mathrm{bearing}}} \tag{4.4}$$

Where J is the polar moment of inertia of the ferrofluid contact. The precise calculation of c_{x} and C_{θ} is found in Appendix B.

4.2.2 Magnetic design

The magnetic design of the mover is based on the following considerations:

- **Magnet thickness** The thinnest commercially available magnets are chosen, as they give the highest magnetic flux per unit of mass. This allows for high accelerations according to Newton's Second Law of Motion.
- **Steel plate** A steel backing plate is used as a surface for microscopic samples to be placed on. The steel plate reduces the reluctance path of the magnetic flux above the magnet ring. Thereby the magnetic flux density below the mover

is increased. Above the mover, at the location where microscopic samples are placed, the flux density is decreased.
- **Single magnet ring** A single magnet ring is used. A double rotor configuration would increase and homogenise the magnetic flux density, however it also increases the ferrofluid damping, due to an increased contact area of the fluid.
- **Distance between mover and stator** The magnet ring is placed close to the stator for a high magnetic flux density at the location of the coils.
- **Steel ring and ferrofluid location** Steel rings on the inside and outside of the magnet poles are used to guide the location of the ferrofluid. Without these steel rings, no air pockets would be formed, decreasing the load capacity and vertical stiffness.

The reader is referred to Appendix D for a detailed description of these considerations.

The mover has a total mass of $m = 464\,\mathrm{g}$. The 16 magnet segments contribute 15.8 g each and the monolithic steel backing plate 211 g. The total mover has a rotational moment of inertia of $I = 9.5 \times 10^{-4}\,\mathrm{kgm}^2$, which is calculated with Solidworks.

4.2.3 Load capacity and stiffness validation

To validate the expected load capacity of 42 N and evaluate the stiffness of the ferrofluid bearing, a force displacement measurement was performed on a Zwick test bench. The measurement setup and the results are seen in Figure 4.8. The bearing has a load capacity of 100 N. The stiffness of the bearing is not directly measured. Instead, the stiffness of the bearing with the stiffness of the bench in series is measured. Therefore a reference measurement of the stiffness of the bench is done. The test bench has a stiffness of $k_{\mathrm{bench}} = 1.7 \times 10^6\,\mathrm{N/m}$. The measurements show a stiffness of approximately $5.5 \times 10^5\,\mathrm{N/m}$. The stiffness of the bearing is calculated with:

$$k_{\mathrm{bearing}} = 1/(\frac{1}{k_{\mathrm{tot}}} - \frac{1}{k_{\mathrm{bench}}}) = 8.1 \times 10^5\,\mathrm{N/m} \tag{4.5}$$

The measured bearing stiffness of $8.1 \times 10^5\,\mathrm{N/m}$ is 80 times higher than the $1 \times 10^4\,\mathrm{N/m}$ reported in literature. This difference can be mainly attributed to the larger surface area of the mover compared to the area of the magnets used in literature. It is therefore a good practice to express the stiffness in terms of stiffness per unit pocket surface area: $9.5 \times 10^7\,\mathrm{N/m}^3$.

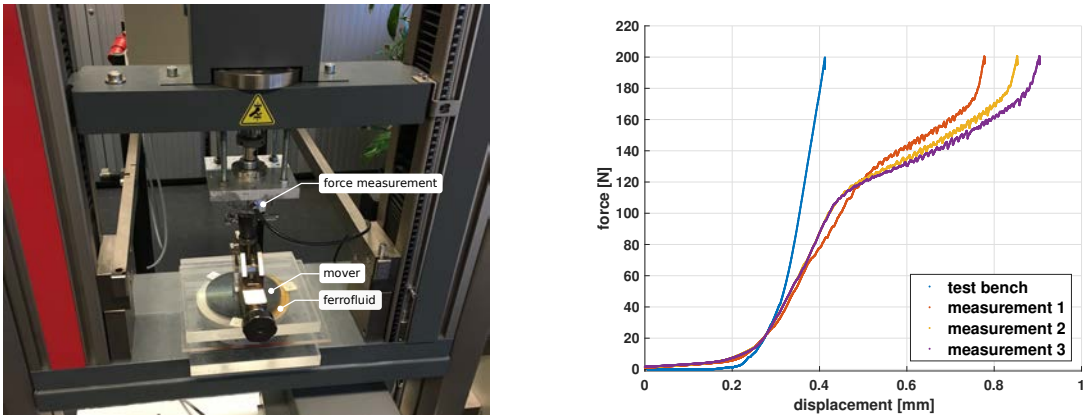

(a) **(b)**

Figure 4.8: Measurement of the load capacity and stiffness of the ferrofluid bearing. (a) Measurement setup. To get a good measurement of the load capacity and stiffness, the area of the air pocket should be the same as in the real setup. Therefore the bearing is placed on a flat surface with a hole in the centre, to represent the actual stator. (b) Measurements. The bearing collapses at loads above 100 N. The test bench itself has a stiffness of 1.7×10^6 N/m. The stiffness of the bearing with the stiffness of the bench in series is measured three times. The measurements show a stiffness of approximately 5.5×10^5 N/m.

4.3 Stator design

The coils are embedded into a PCB with two copper layers, since it was seen in [1] that a PCB actuator allows a stator to be designed that has good thermal behaviour, and it can be produced in large quantities at low cost. In order to create a closed circuit, each coil needs at least two copper PCB layers. The PCB consists of a base layer of glass-reinforced polymer (FR4), two layers of copper on the outside of the FR4, covered by a layer of soldermask which is usually green or black. The basic layup of a PCB is seen in Figure 4.9. The final stator PCB is seen in Figure 4.10.

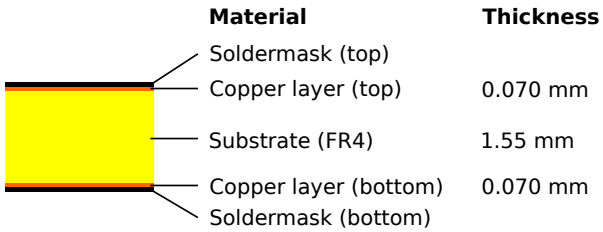

Figure 4.9: The PCB consists of base layer of FR4 and two copper layers. The copper layers are partially covered by soldermask.

Figure 4.10: Final stator design: seven coils are embedded in a PCB.

4.3.1 Optimising the number of windings

Heat is produced by the coils of the PCB. The dimensions of the coils can be optimised to keep heat generation and power consumption as low as possible. The width of each coil d, number of windings per coil n, power supply voltage U, and copper thickness t are the design variables.

Since most amplifiers do not function below 5 V, this is the minimum power supply voltage. For seven coils and eight magnet poles, increasing the width of a coil above 7.5 mm would reduce the average magnetic flux density that is acting on the coil at large translations (±15 mm). This is caused by the fact that one side of the coil would "see" both a positive and negative flux. The maximum width of each coil is thus set to 7.5 mm.

Under the constraints of the required force of 0.4 N and torque of 0.1 Nm, and not exceeding the maximum amplifier current of 3 A, the objective is to minimise the heat produced per unit of force.

The power dissipated per coil is:

$$Q = I^2 R \tag{4.6}$$

The force delivered by each coil is given by:

$$F = B(nI)l \tag{4.7}$$

To achieve the required forces with an average flux density B and an active length per winding l, a certain magnetomotive force $\mathcal{F} = nI$ is needed.

Changing the number of windings creates two effects:

- Less windings → higher currents necessary to achieve the required forces → more heat production
- Less windings → wider windings → lower resistance → less heat production

The resistance of each winding can be calculated with:

$$R = \frac{\rho l_{\text{tot}}}{A_{\text{w}}} = \frac{\rho n k l_{\text{w}}}{h d_{\text{w}}} \tag{4.8}$$

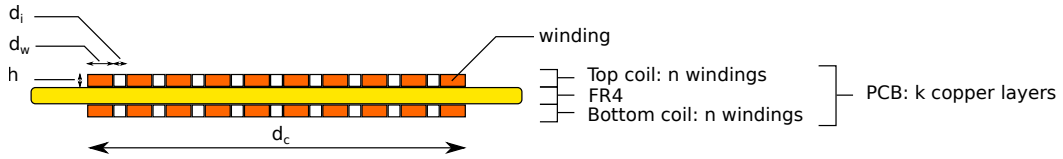

Figure 4.11: Coil dimensions and parameters: copper layer height h, coil width d_c, winding width d_w, isolating width d_i, number of windings per coil n, number of copper layers k.

where ρ is the resistivity of copper, l_{tot} the total length of one coil, k the number of copper layers of the PCB, A_w the cross sectional area, l_w the length, h the height and d_w the width of one winding. The height of a winding is equal to the thickness of the copper layer of the PCB. The cross sectional area (Figure 4.11) of each top or bottom coil half A_c, defined by its height h and width d_c, consists of n winding areas A_w with a width of d_w, and (n-1) isolating areas A_w with a width of d_i:

$$A_c = nA_w + (n-1)A_i = (nd_w + (n-1)d_i)h \tag{4.9}$$

This allows expressing the above formula as:

$$R = \frac{\rho n^2 k l_w}{h(d_c - (n-1)d_i)} \tag{4.10}$$

This relation shows that the coil width d_c and copper thickness h should be chosen as high as possible. Additionally it is seen that the number of windings increases R more than quadratically, whereas according to Equation 4.7 it decreases I^2 only quadratically. To minimise power losses the number of windings should thus be as low as possible, as long as the force requirement per coil is met. It is equivalent to stating that the volume fraction of copper in the PCB should be as high as possible.

As the number of windings changes the resistance of the coils, it acts as a conversion ration between voltage and current. For the desired low number of windings, the currents are high and the voltages are low. The voltage cannot be below the minimum amplifier voltage of 5 V without reducing the resolution of the amplifier and the current cannot exceed the maximum current per amplifier of 3 A.

The optimisation for number of windings is displayed in Figure 4.12 for a copper thickness h of 70 µm and coil width d_c of 7.5 mm. A total of 10 windings per side is selected, with a winding width d_w of 500 µm and an isolation width d_i of 250 µm.

The price of a PCB per unit of copper is non-linearly related to copper thickness. Since it is lowest for a copper thickness of 70 µm, this thickness is used.

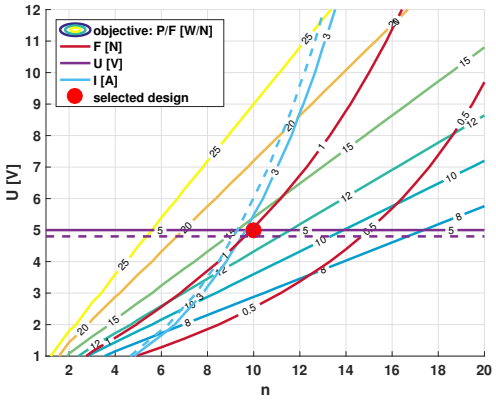

Figure 4.12: An optimisation was performed to determine the number of windings per coil. The objective was to minimise the power losses per unit force created. At any time, five of the seven coils should be able to create the required torque of 0.1 Nm. An average arm of 45 mm gives 0.5 N per coil. Since the resistance of each coil in practice might be higher than theoretically calculated, it was decided to design each coil to deliver a force of 1 N. The selected design with 10 windings per coil is indicated in red.

4.3.2 PCB design

The PCB design was performed in Eagle and shown in Figure 4.13. A Matlab program was written to output Eagle commands for drawing the seven coils in Eagle. This allowed a design to be realised that meets the manufacturing requirements. The basics to PCB design for an electromagnetic actuator and a description of the design approach are found in Appendix E.

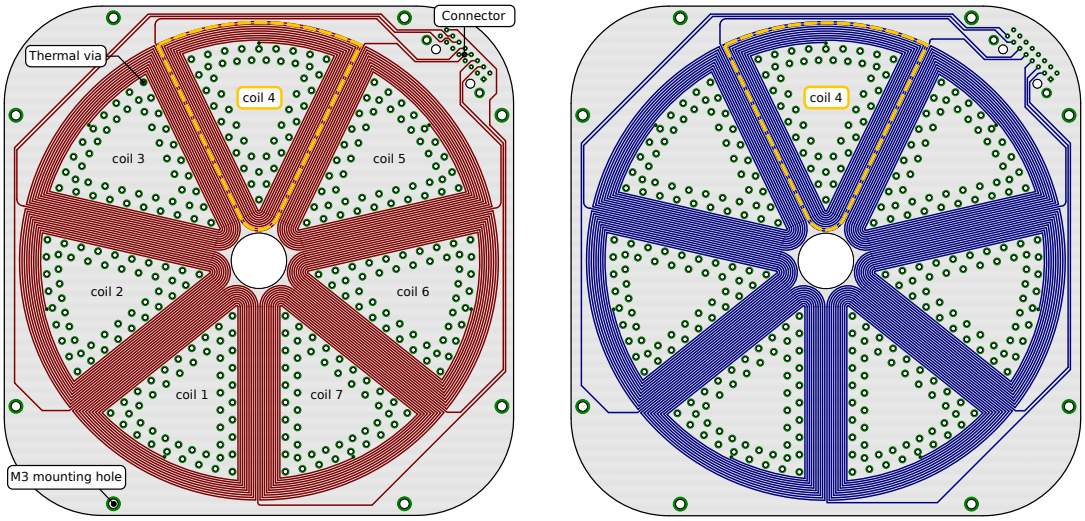

(a) Top copper layer **(b)** Bottom copper layer

Figure 4.13: The coils of the stator are embedded in two copper layers of a PCB. Top view of the coil windings in (a) the top copper layer and (b) the bottom copper layer. The location of coil number 4 is indicated in yellow. The thermal vias create a thermal connection between the copper layers for increased heat dissipation.

Coil resistance and inductance

The resistance and inductance of each coil were measured. They are slightly different for each coil since the traces connecting each coil to the connector have different shapes and lengths.

Table 4.1: Properties of the seven coils of the stator

	Resistance	Inductance @ 1 kHz
Coil 1	2.0 Ω	24.1 µH
Coil 2	2.0 Ω	25.9 µH
Coil 3	1.9 Ω	25.7 µH
Coil 4	1.8 Ω	26.5 µH
Coil 5	1.8 Ω	26.0 µH
Coil 6	1.8 Ω	26.3 µH
Coil 7	1.9 Ω	25.4 µH

4.3.3 Thermal design

Copper has a much higher conductivity (400 W/mK) than FR4 (0.25 W/mK). Therefore the copper layers are connected by so called thermal vias. Thermal vias are created by drilling a hole in the FR4 base layer and subsequently copper plating the hole. An optimisation to design the sizing and spacing of thermal vias as in [12] was used. The thermal vias allow a good thermal path from the coils to the copper planes of PCB. On top of the PCB a 0.125 mm thick sheet of Mylar is placed, to prevent ferrofluid from entering the thermal vias.

Additionally, the bottom copper planes inside the windings are not covered with soldermask to allow a heat sink to be added for additional thermal capacity, increased area for heat dissipation and a larger heat transfer coefficient from the PCB to the surroundings. The heat sink is a 300 µm copper plate of the size of the PCB. Alternatively a 500 µm thick aluminium heat sink could be used. Since copper has a thermal conductivity of 401 W/m/K and aluminium 237 W/m/K, a 300 µm copper plate conducts heat similar to a 500 µm aluminium plate.

Figure 4.14: The bottom copper planes of the PCB, inside the windings, are not covered with soldermask to allow a copper heat sink to be added.

Eddy current damping due to heat sink

The heat sink also causes so-called Eddy current damping. A velocity of the mover causes a voltage to be induced in the copper. Faraday's law describes this phenomenon; the induced voltage $\mathcal{E}$ is described by the change in magnetic flux ϕ_{m} per unit time t:

$$\mathcal{E} = -\frac{d\phi_{\mathrm{m}}}{dt} \tag{4.11}$$

Since copper and aluminium are electrical conductors, this causes currents in the heat sink. These currents create Lorentz forces that act against the direction of movement on the mover. The induced currents and forces scale linearly with velocity. This corresponds to a damping force.

The Eddy current damping scales linearly with the induced currents.

$$c_{\mathrm{Eddy}} \propto I = \frac{U}{R} = \frac{U}{\frac{\rho l}{wt}} \propto \frac{t}{\rho} \tag{4.12}$$

where w is the width of the cross sectional area of the heat sink, t is the thickness of the heat sink, ρ is the electrical resistivity of the material of the heat sink and l is the length of the conductor over which the voltage is applied.

Thus as long as the factor between thickness and electrical resistivity of the heat sink is kept the same, the same amount of Eddy currents is expected. Since copper has an electrical resistivity of $1.68 \times 10^{-8}\,\Omega\mathrm{m}$ and aluminium $2.82 \times 10^{-8}\,\Omega\mathrm{m}$, a 300 µm copper plate creates a similar amount of Eddy current damping as a 500 µm aluminium plate.

That the electrical and thermal conductivity of copper are both approximately a factor 1.7 higher than those of aluminium is not surprising, since electrical and thermal conductivity phenomena are both related to how well electrons can move through the material.

Although aluminium is the preferred choice due to lower cost, a copper heat sink was applied in the demonstrator since 300 µm copper was available at the university.

Thermal validation

The heat generated in the coils creates a temperature rise dT of the PCB. When the assumption is made that all heat is transferred to the air by means of convection, the heat generated is related to temperature by:

$$dT = \frac{Q_{\mathrm{total}}}{hA_{\mathrm{surface}}} \tag{4.13}$$

where h is the heat transfer coefficient and A_{surface} is the surface area used for convection. This behaviour is experimentally validated by applying a current of 0.5 A and 1 A to all coils simultaneously over 500 s. The relation between temperature and time is seen in Figure 4.15. The temperature rise thus does not exceed the maximum operating temperature of the permanent magnets (NdFeB / N42) of 80 °C.

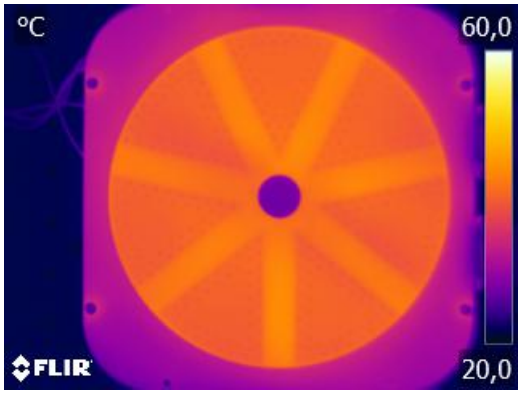

(a) Temperature after 500 s at 0.5 A. $T = 44\,^{\circ}\mathrm{C}$.

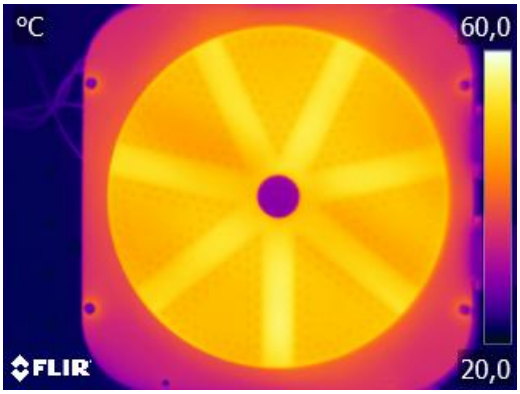

(b) Temperature after 500 s at 1 A. $T = 55\,^{\circ}\mathrm{C}$.

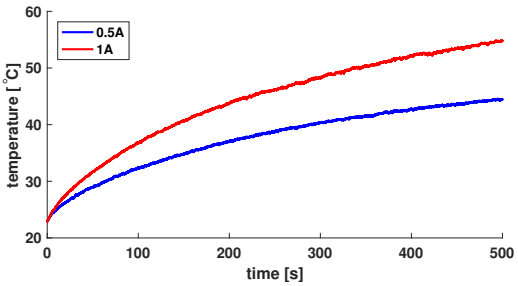

(c) Temperature over 500 s.

Figure 4.15: Thermal image and temperature measurement of the coils, measured for two current settings (a) 0.5 A and (b) 1 A, over 500 s (c). The outside of each coil is not seen by the thermal camera, since the positive stop blocks that part of the PCB.

4.4 Actuator forces and torque

One of the key performance indicators of the actuator is the motor or force constant k_t. This parameter allows to determine the increase in force generated, for every unit increase in current.

$$k_{\mathrm{t,translation}} = \frac{F}{I} \approx Bl \tag{4.14}$$

$$k_{\mathrm{t,rotation}} = \frac{T}{I} \approx Blr \tag{4.15}$$

The motor constants of each coil are not constant over the range of translations and rotations. The theoretical modelling of this position dependency and the force validation is described in this section.

4.4.1 Force transformation matrix

The Lorentz forces of the seven coils of the stator generate forces and torques relative to the coordinate system of the stator. The planar forces can be combined into one force vector $\boldsymbol{F}$:

$$\boldsymbol{F} = \begin{bmatrix} F_x & F_y & T_\theta \end{bmatrix}^T \tag{4.16}$$

The currents of each coil can be combined in one current vector $\boldsymbol{I}$:

$$\boldsymbol{I} = \begin{bmatrix} I_1 & I_2 & I_3 & I_4 & I_5 & I_6 & I_7 \end{bmatrix}^T \tag{4.17}$$

Since each coil creates forces in the three directions, a 3x7 force transformation matrix $\mathbf{\Phi}$, including the motor constants of the different coils, can be formed. The forces created by a combination of different currents are calculated with:

$$\boldsymbol{F} = \mathbf{\Phi}\boldsymbol{I} \tag{4.18}$$

The forces and torques produced by the actuator depend on the magnetic flux density acting on each coil, and therefore on the position and rotation of the mover. Each combination of planar position and orientation therefore has its own force transformation matrix, which makes $\mathbf{\Phi}$ position dependent: $\mathbf{\Phi}(x, y, \theta)$.

By inverting this matrix, the currents can be calculated to achieve the required forces at all positions and orientations. Since this matrix is not square, multiple combinations of currents can be found to create the required forces. Therefore this is an over-actuated system.

4.4.2 Modelling

The position-dependent transformation matrix $\mathbf{\Phi}$ describes the coupling between the currents through each coil and the generated forces on the mover. When the mover is at the position $x = 0, y = 0$ and $\theta = 0°$, the forces delivered by each coil are opposite to the forces delivered when the mover is positioned at $x = 0, y = 0$ and $\theta = 45°$. This is due to the reversal in flux density when the mover rotates.

This position-dependent behaviour is modelled with a semi-analytical model using a combination of COMSOL and Matlab. COMSOL is used to calculate the magnetic flux density in z-direction at 1 mm below the rotor. This height corresponds to the average distance of the top and bottom copper layers to the mover. These results are combined in Matlab with the position of the windings of coil number 4, as shown in Figure 4.13. By dividing each straight and curved section of the winding into multiple sections and linearly interpolating the flux density, the Lorentz force created by a force of 1 A on each section can be calculated analytically. Combining the forces created by each section of the coil allows the motor constants kF_x, kF_y and kT_θ to be calculated. The results for the central position are shown in Figure 4.16.

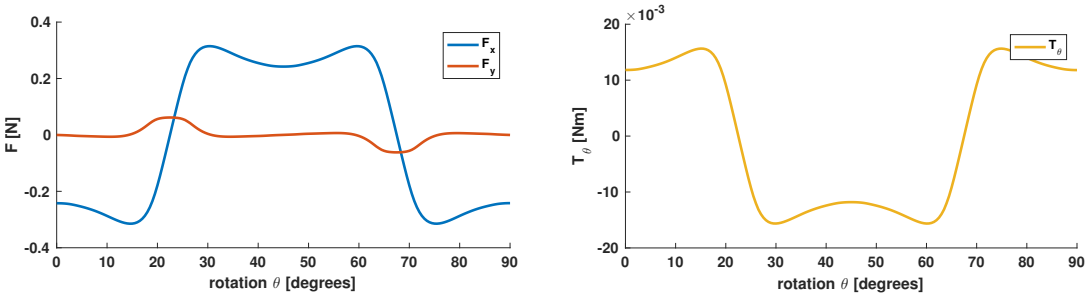

(a) Forces **(b)** Torque

Figure 4.16: The forces and torque that each coil can generate on the mover are dependent on the position (x, y θ) of the mover. The forces and torque that are generated by one coil for a current of 1 A are displayed as a function of rotation θ. The position of the mover is $(x = 0), (y = 0)$. Due to the 8 magnet poles, this signal is repeated every 90°. These calculations are done for all possible positions of the mover, and used as a lookup table for the force transformation matrix.

By translating and rotating the winding position with respect to the flux density calculated in COMSOL, the motor constants can be calculated for different positions in x, y, θ. Instead of expressing the planar position in x, y-coordinates, polar coordinates r, ϕ were used, since the stator is rotational symmetric. This approach created results with less noise and with less computational effort than when COMSOL alone was used. One analytical calculation for every degree in rotation takes 6 s per evaluated location.

The semi-analytical model is used to calculate a position-dependent lookup table for each coil. By calculating the position of the mover relative to each coil, the motor constants $kF_{\mathrm{x,local}}$, $kF_{\mathrm{y,local}}$ and $kT_{\theta,\mathrm{local}}$ in the local coordinate system of each coil are calculated. By an Euler transformation the local forces are translated to the global coordinate system. Each coil thereby gives three entries to the force transformation matrix $\mathbf{\Phi}$.

4.4.3 Validation

The force generated in the x-direction was validated by implementing the position-dependent lookup table in a control algorithm. Two load cells were used to measure the force. A constant force of 0.1 N was applied to position the mover against the load cells. Subsequently the control force was increased in steps of 0.05 N to 0.45 N. The actual force was simultaneously measured. As is seen in Figure 4.17, the force delivered was 12 % lower than the theoretical force. This deviation could be explained by a lower current being delivered to the coils than expected, or the stator coils placed further from the mover in reality than in the model. The difference is seen to be constant over a large range of forces, and is compensated for by decreasing the motor constants used in the control system with 12 %.

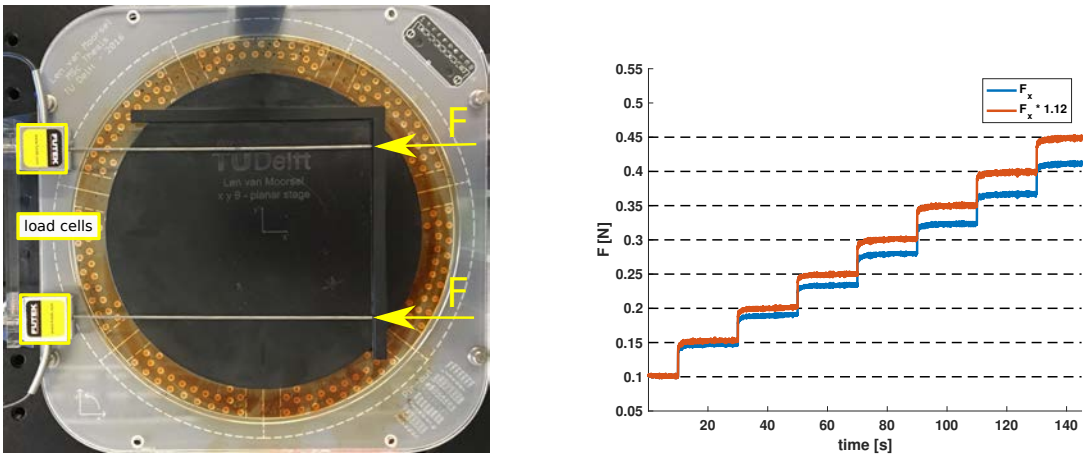

(a) **(b)**

Figure 4.17: Force measurement in x-direction. (a) The measurement setup uses two load cells. The force of the mover is transferred to the load cells by means of two steel rods. (b) The measured force deviates by 12 % from the force setpoint calculated with the inverse force transformation matrix. This measurement is used for calibration. The deviation is compensated for in the control system by a 12 % gain.

4.5 Conclusion

A conceptual analysis was performed to evaluate the forces generated in x and y and torque in θ by different actuator concepts. Sixty concepts with different numbers of magnet poles and coils were evaluated. A concept with 8 magnet poles and 7 coils was chosen for implementation, after considering additional constraints. A magnetic design of the mover and ferrofluid bearing was made. The load capacity and stiffness of the ferrofluid bearing were measured. To determine the number of windings per coil in the PCB stator, an optimisation was performed. A position-dependent transformation matrix containing the motor constants of this setup was semi-analytically calculated. The inverse of this matrix can be used to calculate the required current of each coil to generate planar forces and torque. The forces generated by the actuator were measured and compared to the model.

5
Amplifier

One amplifier is used for each of the seven coils. Although the name amplifier suggests that a control signal is amplified, the voltage is regulated between 0 and 5 V by the amplifiers. H-bridges were selected over linear current amplifiers, since an H-bridge can apply a voltage in either direction, while being powered by one voltage level, whereas current amplifiers need two voltage levels, increasing the cost of the power supply. Moreover, H-bridges are more energy efficient, reducing power consumption.

5.1 Introduction to PWM

H-bridges use a principle called Pulse Width Modulation (PWM) to regulate the average voltage supplied to the load, by switching the power supply voltage on and off at a very fast rate. This creates a block signal with a so-called PWM frequency. The PWM frequency used is 20 kHz. A basic PWM signal is seen in Figure 5.1. The relation between the time that the power supply is on during one period compared to the total time of that period, is known as duty cycle D:

$$D = \frac{t_{\text{on}}}{t_{\text{on+off}}} \tag{5.1}$$

A low duty cycle corresponds to a low voltage, and a high duty cycle to a high voltage:

$$V_{\text{out}} = D \cdot V_{\text{s}} \tag{5.2}$$

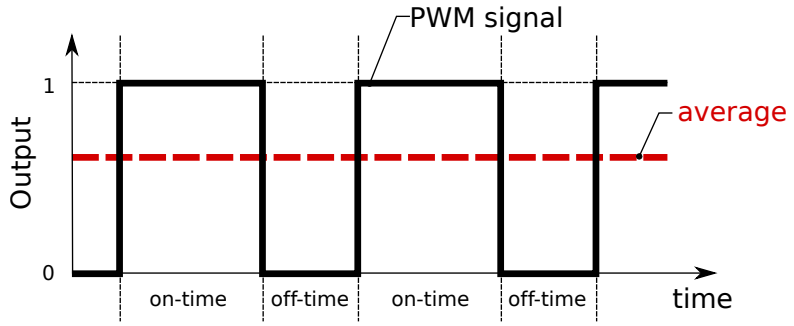

Figure 5.1: PWM signal for a duty cycle D of 60 %. The average output is linearly related to the duty cycle.

where V_{out} is the average output voltage of the H-bridge and V_{s} is the power supply voltage.

5.2 H-bridge

The H-bridge uses four different switches to supply positive and negative currents to the load. The basic H-bridge design is shown in Figure 5.2. Four switches are present that can be turned on or off. The output of the H-bridge is connected to a load, which is usually a motor, indicated by M. By switching the top left switch and bottom right switches on, a positive current is supplied to the load. By switching the top right and bottom left switches on, a negative current is supplied.

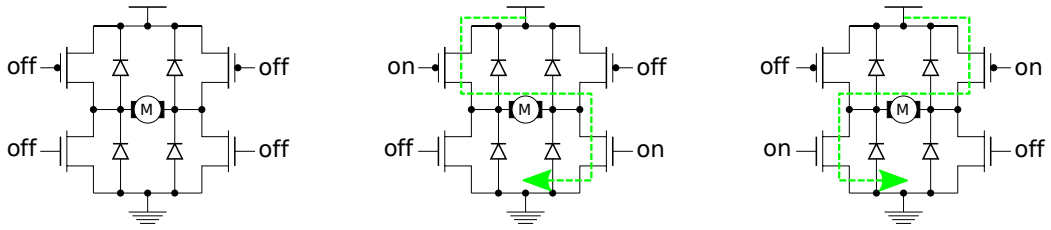

(a) Standby **(b)** Forward operation **(c)** Reverse operation

Figure 5.2: The three modes of operation of the H-bridge. The load is usually a motor, indicated by M. The switches are controlled by PWM signals generated by two Arduinos.

5.3 Load

The H-bridges are used to drive currents through the coils, which act as loads. Each load acts as low-pass filter on the output voltage of the H-bridge. The load can be modelled as a resistance R in series with an inductance L and a back EMF V_{EMF} related to the Electromotive Force generated by the moving permanent magnets. Since the mover is expected to have a maximum velocity lower than 30 mm/s, this term will be considered negligible compared to the resistance and inductance of the coil. A schematic drawing of the load is seen in Figure 5.3. The source impedance of the H-bridges introduces an additional resistance R_{s} to the circuit. This term is small compared to the impedance of the coil.

The transfer function $H(j\omega)$ is calculated with:

$$H(j\omega) = \frac{I_{\text{out}}}{V_{\text{s}}} = \frac{1}{Z(j\omega)} \tag{5.3}$$

resulting in:

$$V_{\text{s}} = Z(j\omega)I_{\text{out}} \tag{5.4}$$

where $Z(j\omega)$ is the impedance of the system. Ignoring the back EMF, the impedance of the system in the frequency domain is:

$$Z(\omega) = R_{\text{s}} + R + j\omega L \tag{5.5}$$

where R_{s} is neglected in the following.

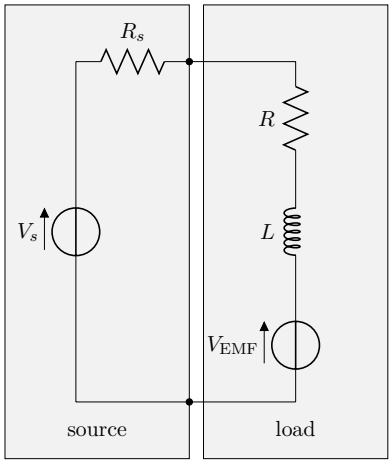

Figure 5.3: The load can be modelled as a resistance in series with an inductance and a back EMF related to the Electromotive Force generated by the moving permanent magnets. The source resistance R_s and Electromotive Force are low compared to the other components and are neglected in the transfer function of the load.

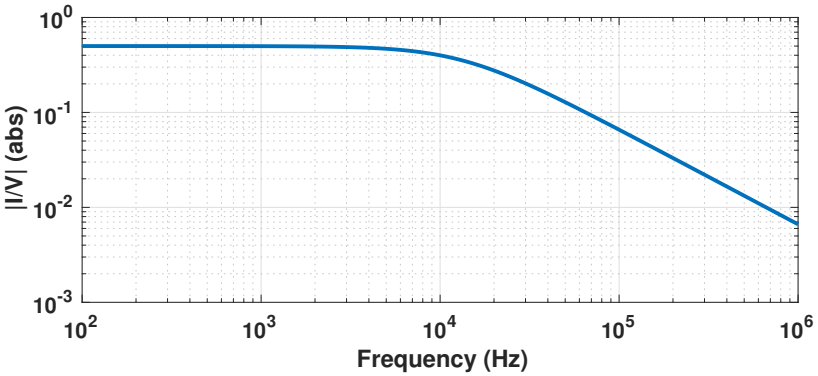

Figure 5.4: Bode plot of load. The load is filtering the 20 kHz Pulse Width Modulation signal. The current ripple has an amplitude of 51 % of the input current. The mass however acts as another low-pass filter. This makes a design without an output filter possible.

This gives the transfer function from voltage to current:

$$H(j\omega) = \frac{1}{Z(j\omega)} = \frac{1}{R + j\omega L} \tag{5.6}$$

The load thus acts as a low-pass filter. The frequency response is seen in Figure 5.4. The range of frequencies that pass the filter is called its bandwidth. The point at which the filter attenuates the signal to half its unfiltered power is called its cutoff frequency ω_c. Since power is defined by:

$$P = I^2 R \tag{5.7}$$

this occurs when the current is decreased by a factor $\sqrt{2}$. This corresponds to an amplification of approximately $-3\,\text{dB}$ or an attenuation of $3\,\text{dB}$.

$$\frac{|H(0\,\text{rad/s})|}{\sqrt{2}} = |H(\omega_\text{c})| \tag{5.8}$$

Solving Equation 5.8 yields:

$$\omega_c = \frac{R}{L} \tag{5.9}$$

If the PWM frequency is significantly higher than the cutoff frequency, the coil reduces the current ripple created by the PWM signal. For a coil with a resistance of 1.8 Ω and inductance of 24 µH, the coil has a cutoff frequency of 11.9 kHz. At 20 kHz the load filters the PWM signal:

$$\frac{|H(20\,\text{kHz})|}{|H(0\,\text{rad/s})|} = \frac{|\frac{1}{R+j\omega L}|}{|\frac{1}{R}|} = \frac{R}{|R+j\omega L|} = \frac{1}{\sqrt{1+(0.533\pi)^2}} = 0.51 \tag{5.10}$$

This results in a current ripple with a frequency of 20 kHz and an amplitude of 51 % of the input current. Since this current is used generate a force to actuate the mover, the response of the mover on the force ripple should also be taken into account. With a mass of 464 g a response with a gain $|\frac{x}{F_x}|$ of 1.4×10^{-10} m/N is expected. Therefore, a reduction of the current ripple is unnecessary. The current ripple could however be reduced by increasing the PWM frequency or by using an additional output filter [2]. Apart from a lower force ripple, an output filter has the advantage of lower power losses for a certain force, since power losses scale with I^2, and an output filter reduces high current peaks.

5.4 Implementation

Two types of H-brides were implemented. First a standard solution based on a TB6612 H-bridge with a maximum PWM frequency of 100 kHz was implemented. A PCA9685 PWM driver controlled the H-bridges and communicated over an Inter-Integrated Circuit (I2C) protocol with the Raspberry Pi. During the experimental implementation it was found that the PWM driver limits the PWM frequency to a maximum of 1526 Hz. This created loud noise for the human ear. Additionally the I2C bus could only handle approximately 200 new duty cycle setpoints per second. For seven coils this reduces the sample rate for each coil to just below 30 Hz. To not overload the I2C bus, the sample rate of the control system would have to be reduced, increasing the communication delays between the different software programs.

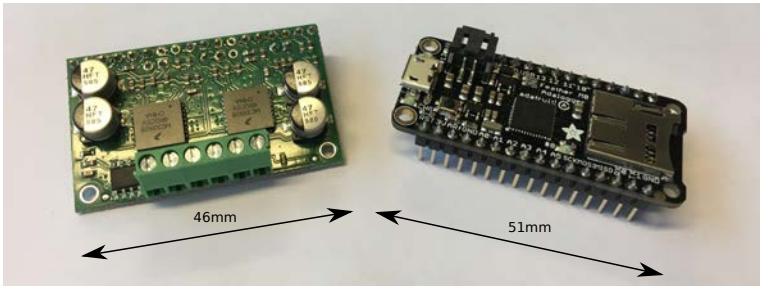

Figure 5.5: Selected hardware. (left) H-bridge based on the MC33926 chip. (right) Arduino: Adafruit Feather M0 microcontroller used for H-bridge control.

Since this significantly reduced the bandwidth of the system, a new design was made based on another H-bridge chip. The MC33926 H-bridge with a maximum PWM

frequency was selected. It features current feedback, under-voltage, over-current and over-temperature protection. This makes this H-bridge very suited for a robust amplifier design. Current feedback allows a current controller to be built. Without this feature a shunt could be used for current measurement. The 14 PWM signals necessary for the seven H-bridges are controlled with two Arduinos. The 32-bit Adafruit Feather M0, based on Cortex M0 microcontroller architecture, was selected since it is a low-cost microcontroller with a clock speed of 48 MHz and 8 hardware PWM pins. Each Arduino controls three or four H-bridges respectively, and communicates with the Raspberry over a communication protocol called SPI. The selected hardware is seen in Figure 5.5.

5.4.1 Timers, counters and PWM

To create PWM signals, an Arduino uses its internal clock, a counter and a comparator. Each clock cycle, the counter is increased by one step, and the value of the counter is compared to a reference value. If the counter is lower or higher than the reference value, the output of the comparator is respectively set to zero or one. By inverting the created signal, a PWM signal is created.

Two PWM operating modes can be selected: fast PWM and phase-correct PWM. The basic working principle is shown in Figure 5.6. In fast PWM the counter only increases, in phase-correct PWM the counter also counts down. In fast PWM mode, when changing the duty cycle the phase of the signal is changed. Fast PWM is generally used for Digital to Analog Converters, when phase does not matter but high frequency is needed. To mitigate the change in phase, phase-correct PWM can be used. This is generally used to for motor speed controllers and servos. Since the duty cycle has to be changed continuously, phase-correct PWM was used. The downside of this is that the number of steps to set the duty cycle, the resolution, reduces by 50 % compared to fast PWM.

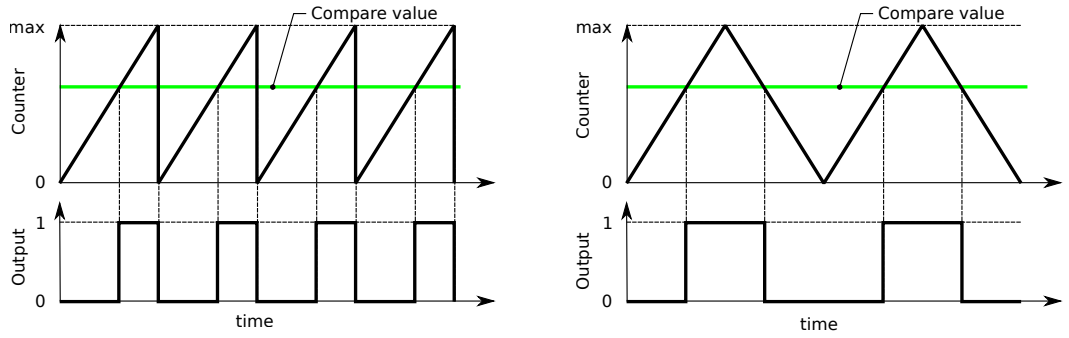

(a) fast PWM **(b)** phase-correct PWM

Figure 5.6: PWM counter, compare and output: (a) fast PWM (b) phase-correct PWM.

In fast PWM mode, the frequency f_{PWM} is related to the clock frequency f_{clock} by:

$$f_{\text{PWM}} = \frac{f_{\text{clock}}}{\#_{\text{steps}}} \tag{5.11}$$

where $\#_{\text{steps}}$ is the total number of digital steps to set the duty cycle. For phase-

correct PWM and the same number of steps, the PWM frequency is halved due to the counter counting up and down:

$$f_{\text{PWM}} = \frac{f_{\text{clock}}}{2\#_{\text{steps}}} \tag{5.12}$$

To reach the same PWM frequency as in fast PWM mode, the number of steps has to be reduced by a factor two, reducing the resolution of H-bridge. A higher resolution could be achieved with a microcontroller with a higher clock frequency, or with a lower PWM frequency. However, microcontrollers with clock frequencies above 84 MHz are unlikely to be available at a low price. A lower PWM frequency would increase the current ripple through the coils and create audible sound for human hearing.

Specifications of the amplifier are listed in Table 5.1.

Table 5.1: Specifications of the amplifier design

clock frequency	f_{clock}	48 MHz
PWM frequency	f_{PWM}	20 kHz
number of steps	$\#_{\text{steps}}$	1200
resolution (bits)		10.2-bit
resolution at V_{s}=5 V		4.2 mV

5.4.2 Power supply

The power supply used is a TracoPower TML 40105C, able to supply 8 A at 5 V. It is a switched-mode amplifier that converts 230 V AC to 5 V DC. It is selected for its compact design and 5 V output, which is the minimum voltage for the H-bridges. Choosing the voltage as low as possible allows a low number of windings to be used per coil and keeps the smallest change in voltage of the H-bridges low. It has a switching frequency of 132 kHz and an efficiency between 75 and 84 %.

5.5 Validation

In this section the performance of the power supply and H-bridge are validated.

5.5.1 Power supply

The voltage of the power supply is measured for different loads, to determine the internal resistance of the power supply (Figure 5.7).

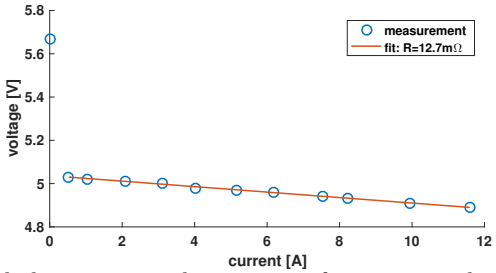

Figure 5.7: The power supply has an internal resistance of approximately 12.7 mΩ. The voltage drops approximately 0.6 V from no load to loading. This is likely a base-emitter voltage drop across a transistor.

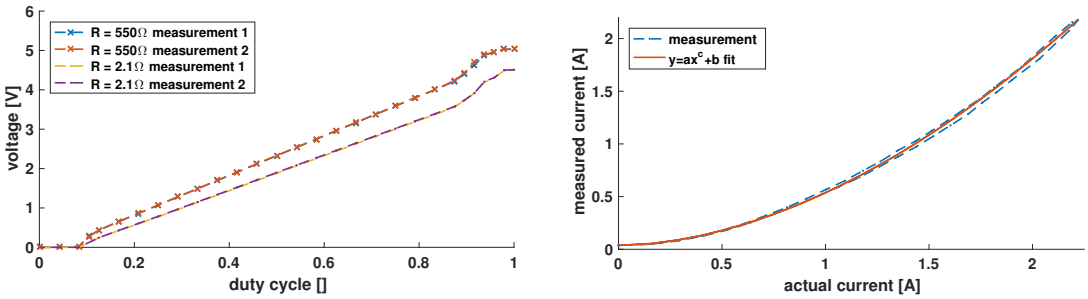

(a) (b)

Figure 5.8: (a) The output voltage of the H-bridge is non-linearly related to the duty cycle. The measurement was performed with a high impedance as load, to keep the voltage drop over the H-bridge low, and with a coil, to measure the increased voltage drop over the H-bridge at higher currents. (b) The current measured by the H-bridge is non-linearly related to the actual output current. A fit was made assuming a form $y = ax^c + b$. The values are $a = 0.5$, $b = 0.037$ and $c = 1.825$.

5.5.2 H-bridge

In theory, the H-bridge creates a voltage linearly related to the duty cycle and the current measurement should be linearly related to the actual current. Measurements were performed to verify if the voltage is linearly related to the duty cycle and if the current is measured accurately. However, both these relations were not linear (Figure 5.8). Since the voltage is non-linearly related to duty cycle, a lower voltage is applied to the coil than would be expected in theory. However, since the non-linearity between duty cycle and voltage is accurately known and repeatable, it can be compensated for using a lookup table from voltage to duty cycle.

5.6 Current controller

The resistance of the coils increases with temperature. The resistance R at any temperature T is related to the resistance R_0 at temperature T_0.

$$R = R_0(1 + \alpha(T - T_0)) \tag{5.13}$$

Copper has a temperature coefficient α of $3.86 \times 10^{-3}\,\Omega\text{m}/^\circ\text{C}$. A resistance of $2\,\Omega$ at $20\,^\circ\text{C}$ increases to $2.15\,\Omega$ at $40\,^\circ\text{C}$. For a constant voltage, this causes the current, and therefore the force, to decrease with temperature.

To compensate for the increase in resistance with temperature, the current through the coil is measured and used for feedback control. The current measurement has to be corrected for the revealed non-linearity. A lookup table was implemented. As the sensitivity of this table is high for low currents, measurement noise causes a large impact on the current measurement. This makes the current sensor unsuited for current feedback at low currents. For this reason a feedforward controller is implemented for low current setpoints. The exact implementation of these controllers is discussed in Appendix G.

The performance of the feedforward controller and feedback controller is seen in Figure 5.9. Only the feedforward controller is used for current setpoints below 0.5 A and the feedback controller is added at higher values. This creates a linear relationship

between current setpoint and current output. Additionally, the temperature could be measured to compensate with feedforward control for the resistance increase with temperature. This however requires additional sensors. For improved current control, a shunt should be used for current measurement.

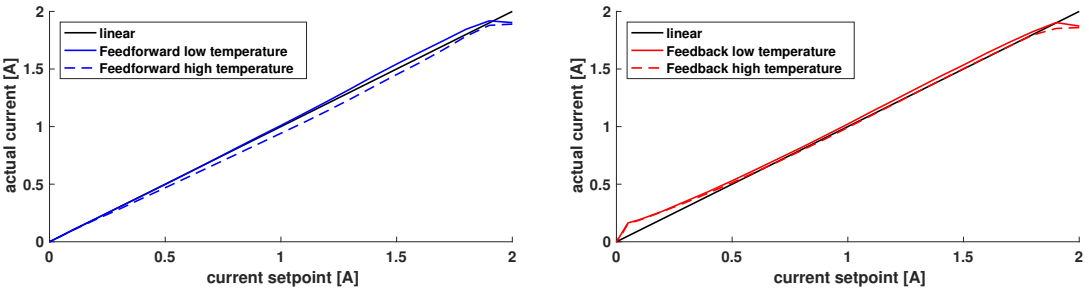

(a) feedforward controller **(b)** feedback controller

Figure 5.9: The performance of the feedforward and feedback controller was measured at two different coil temperatures. (a) The feedforward controller uses a lookup table to compensate for the non-linear relationship between duty cycle and voltage. The feedforward controller is not compensating the duty cycle for the increase in coil resistance at increased temperature levels. (b) The feedback controller uses the current sensor embedded in the H-bridge chip. It uses a lookup table to compensate for the non-linear relation between actual current and measured current. The current controller compensates for the increase in coil resistance, but does not perform well at low current setpoints. Combining these controllers allows a linear relation between current setpoint and actual current to be achieved over a large range of currents. The maximum currents of 1.9 A are limited by the 5 V voltage source, the internal voltage drop in the H-bridge and the coil resistance.

5.7 Conclusion

An amplifier based on H-bridges was designed, implemented and validated. The H-bridges are used to drive currents through the seven coils of the PCB stator. H-bridges were selected over linear amplifiers since H-bridges can apply a voltage two directions, while being powered by one voltage level, and for their high efficiency. To overcome practical problems, a current controller consisting of a feedforward and a feedback control scheme with different lookup tables was implemented.

6
Controller

The demonstrator stage is a Multiple-Input Multiple-Output system. For simplified control it is decoupled into three Single-Input Single-Output systems. Three independent Proportional, Integral and Derivative (PID) controllers are used to control the position of the mover. A schematic overview of the control system is shown in Figure 6.1.

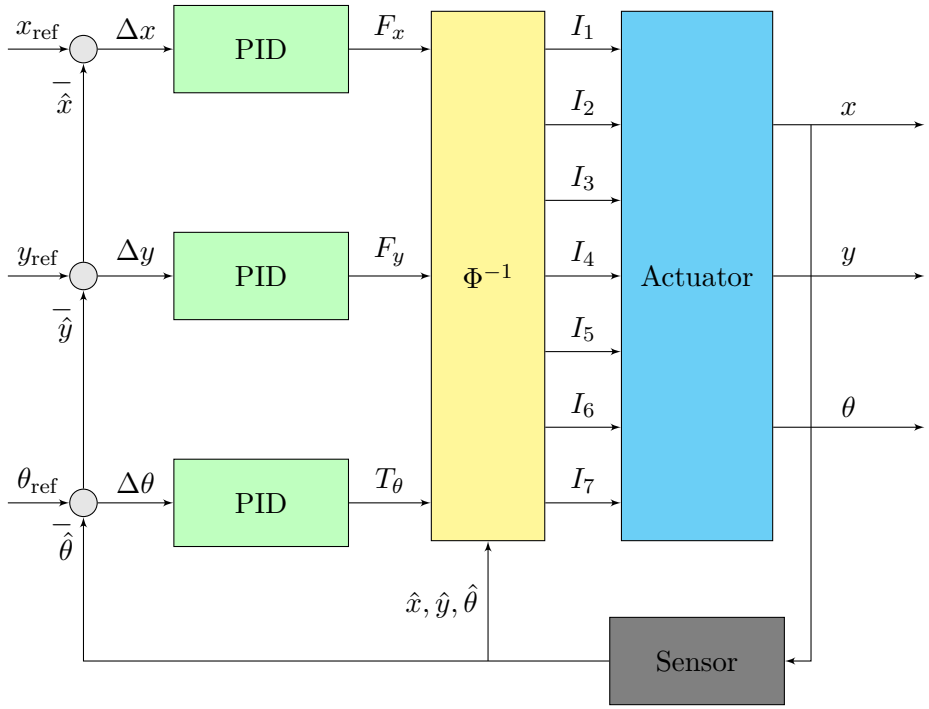

Figure 6.1: Control system overview. The error between the reference value and measured position is used in three independent PID controllers. The calculated forces are transformed by an inverse transformation matrix Φ^{-1} into currents to be supplied to the stator. The actuator transforms the currents into forces and the forces into positions.

In this chapter the control system used to position the mover is presented. The chapter starts with controller goals and background information on how to measure the performance of the controller. Then the theoretical model of the system to be controlled is discussed, followed by the implementation of the inverse force transformation matrix and the design and tuning of the three PID controllers. Since the sensor sys-

tem is limiting the control frequency, first a basic controller is designed and used to identify the response of the system. Then a novel advanced controller, that mitigates the limitations of the sensor system, is designed to increase the control bandwidth. The translational controller is covered in this chapter. The reader is referred to Appendix H for the rotational controller.

6.1 Controller goals

The basic goals of a control system [13] are:

- Avoid instability
- Follow reference signals
- Reduce effects of load disturbances
- Reduce effects of measurement noise

6.2 Performance specifications

In order to design a control system, performance requirements must be set and stability margins must be determined. Stability margins allow the overall stability of the closed-loop response to be determined from the open-loop transfer function and give an indication of the degree of stability of the system. Stability margins can guarantee certain levels of performance and robustness of the control system.

Performance specifications are related to the open-loop (OL) transfer function L

$$L(j\omega) = CG \tag{6.1}$$

where C and G are the transfer functions of the controller and the plant in the frequency domain.

- **Control bandwidth** is the lowest frequency where the gain of the open-loop transfer function is equal to 1, also known as the unity-gain crossover frequency.
- **Phase margin** is the amount of additional phase lag to reach the stability limit of $-180°$. It is determined by measuring the difference of the phase of the open-loop response with respect to $-180°$, at the unity-gain crossover frequency.
- **Gain margin** is the amount of gain needed to reach instability. It is measured as the reciprocal of the magnitude when the phase of the OL transfer function crosses $-180°$. A high gain margin avoids that errors in the calculated controller gains lead to instability.

Recommended values for phase and gain margins are 45° - 60° and 2 - 5 [14].

6.3 System

The seven currents corresponding to the Lorentz actuators are the inputs of system that has to be controlled. The positions x, y and θ are the outputs (Figure 6.2). The system consists of two parts: the force transformation matrix (subsection 4.4.1) with the real motor constants of each actuator, and the plant dynamics in each controlled Degree of Freedom.

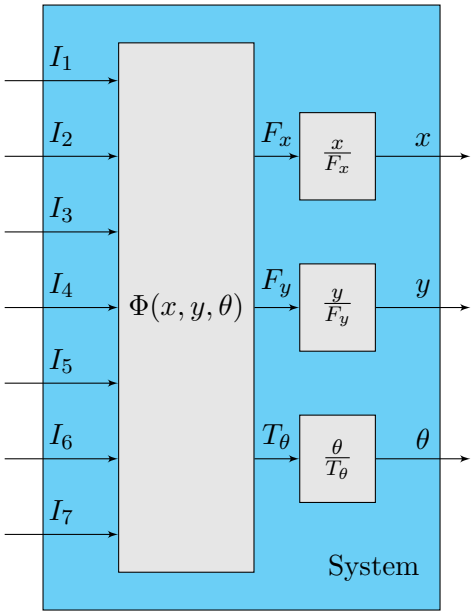

Figure 6.2: The actuator is the system that has to be controlled. The force transformation matrix converts the applied currents into forces and torque. The plant dynamics corresponding to each DOF convert the applied forces to the position and rotation of the mover.

The plant dynamics are modelled as a mass-damper system in translation and an equivalent model in rotation.

Plant dynamics in translation

$$m\frac{d^2x}{dt^2} + c\frac{dx}{dt} = F(t) \tag{6.2}$$

$$G_{\mathrm{x}}(s) = \frac{x}{F} = \frac{1}{ms^2 + cs} \tag{6.3}$$

where m is the mass of the mover and c the damping coefficient.

Plant dynamics in rotation

$$I\frac{d^2\theta}{dt^2} + C\frac{d\theta}{dt} = T(t) \tag{6.4}$$

$$G_\theta(s) = \frac{\theta}{T} = \frac{1}{Is^2 + Cs} \tag{6.5}$$

where I is the moment of inertia of the mover and C the rotational damping coefficient. The frequency response of these two systems is shown in Figure 6.3.

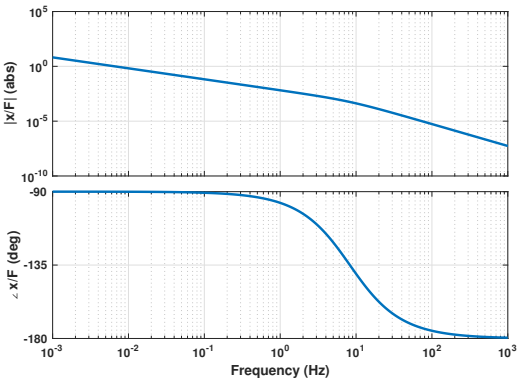

(a) Translational: $G_{\mathrm{x,y}}$

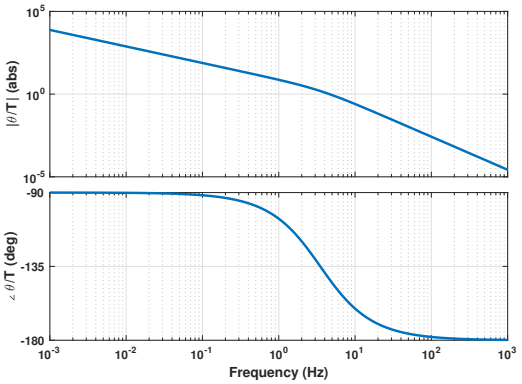

(b) Rotational: G_{θ}

Figure 6.3: Modelled plant dynamics, based on the mass, moment of inertia and estimated values for ferrofluid damping in translation and rotation.

6.4 Inverse transformation matrix and commutation

As was discussed in section subsection 4.4.1, the motor constant of each actuator depends on the three DOF position of the stage because the permanent magnets are attached to the mover. The force that each coil delivers at every position for a current of 1 A was calculated with a semi-analytical model. The real force was seen to deviate 12 % from the calculated force. This deviation is compensated for in the control system by implementing a feedforward control scheme.

Inverse transformation matrix

The position-dependent transformation matrix is implemented in the control system to make sure the control system "knows" what current to supply to generate a force.

$$\boldsymbol{I} = \boldsymbol{\Phi}^{-1}\boldsymbol{F} \tag{6.6}$$

Since the position-dependent transformation matrix is not square, the system of equations defined by the transformation matrix does not yield a single solution. Therefore a pseudo-inverse of the matrix is calculated to obtain one of the solutions.

An alternative would be to make the transformation matrix square by deleting four of the seven columns of the matrix. The columns with the lowest motor constants for that position could for instance be chosen. For translation this is likely to give higher forces for the same total current, since only coils are used that create forces that align well with the desired total force. For rotation however, deleting four columns would significantly reduce the produced torque for the same total current. Since for rotation almost every coil can create a force in the desired direction, the motor constant is higher using a pseudo-inverse than when four columns of the transformation matrix are unused.

Commutation

The implementation of the inverse transformation matrix allows the currents to be calculated when a full rotation is performed. This is referred to as commutation in literature. The currents sent to each coil when a full rotation is performed around $x = 0$ and $y = 0$ are shown in Figure 6.4. The electrical frequency is four times higher

than the mechanical frequency. This is caused by the 8 alternating magnet poles, which create the same electrical behaviour for every 90° in rotation.

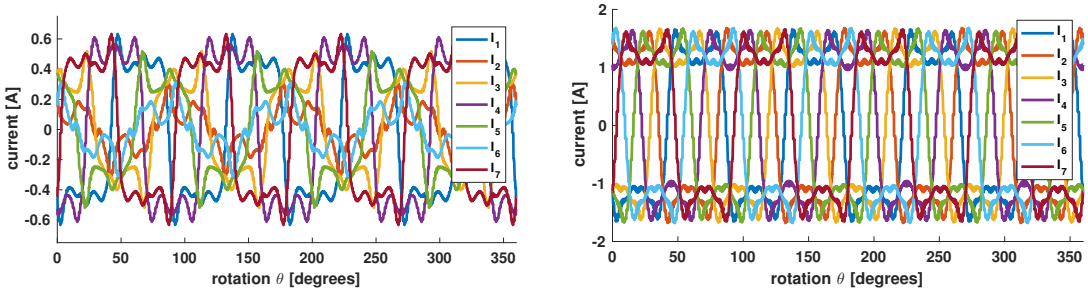

(a) $F_x = 0.4\,\text{N}$ **(b)** $T_\theta = 0.1\,\text{Nm}$

Figure 6.4: Commutation at $x = 0$ and $y = 0$: the currents sent to each coil. The electrical frequency is four times higher than the mechanical frequency, caused by the magnet ring of 8 alternating poles. (a) A force of 0.4 N is generated in x-direction. (b) A torque of 0.1 Nm is generated. A slight difference between the currents to coil 4 and the other coils is observed. Only coil 4 does not undergo an Euler transformation from its local coordinate system to the global coordinate system.

6.5 Basic control: introduction to PID control

The control scheme to position the plant is based on a PID controller. This controller calculates the error value $e(t)$ between the desired reference setpoint and the measured position. Based on this error, a correction action $u(t)$ is calculated with proportional, integral and derivative terms. The controller tries to minimise the error by continuously calculating a new value of $u(t)$.

$$u(t) = K_\text{p} e(t) + K_\text{i} \int_0^t e(\tau) d\tau + K_\text{d} \frac{de(t)}{dt} \tag{6.7}$$

where K_p is the proportional gain, K_i the integral gain and K_d the derivative gain. Taking the Laplace transform of this equation yields a formulation in the frequency domain:

$$C(s) = K_\text{p} + \frac{K_\text{i}}{s} + K_\text{d} s \tag{6.8}$$

- P accounts for present values of the error. If the error is positive, the control output is also positive.
- I accounts for past values of the error. If the output at this time is not sufficiently strong, error will accumulate over time, and the controller output will rise. [15]
- D accounts for possible future values of the error, based on the current rate of change of the error.

K_d also amplifies noise at high frequencies. To attenuate high frequency noise, the derivative gain is filtered with a low-pass filter (LPF). This is referred to as a tamed PID controller. The low-pass filter has a $-3\,\text{dB}$ cutoff frequency ω_c, corresponding to the frequency where the power of the signal is being halved.

The transfer function of an LPF is:

$$H_\text{LPF}(s) = \frac{1}{\frac{1}{\omega_\text{LPF}} s + 1} \tag{6.9}$$

therefore the transfer function of the tamed PID controller is:

$$C(s) = K_\mathrm{p} + \frac{K_\mathrm{i}}{s} + \frac{K_\mathrm{d} s}{\tau_\mathrm{f} s + 1} \tag{6.10}$$

where τ_f is equal to $\frac{1}{\omega_\mathrm{LPF}}$.

Four guidelines for motion control are followed to design the tamed PID controller [16].

1. The open-loop gain of the system at the targeted crossover frequency should equal one. The total controller gain at the crossover frequency should thus be chosen equal to the inverse of the gain of the plant. The proportional gain is equal to the total gain corrected for the additional gain of 3 caused by the differentiator ($K_\mathrm{t} = \frac{1}{G_{@\omega_\mathrm{c}}}$, $K_\mathrm{p} = 0.33 K_\mathrm{t}$).
2. The differentiating action (D) is started at one third of the unity-gain crossover frequency ($\omega_\mathrm{d} = 0.33\omega_\mathrm{c}$).
3. The differentiating action (D) is terminated at three times the unity-gain crossover frequency ($\omega_\mathrm{t} = 3\omega_\mathrm{c}$).
4. The integrating action (I) is started at extremely low frequencies and is stopped at one third of the starting frequency of the differentiator, corresponding to approximately one tenth of the unity-gain crossover frequency ($\omega_\mathrm{i} = 0.1\omega_\mathrm{c}$).

6.6 Basic controller

The first step to a robust controller based on the PID guidelines is getting a good estimate of the frequency response of the plant. This model is obtained through system identification. Since the plant is a mass damper system without any stiffness, it is naturally unstable. Closed-loop system identification is performed using a basic controller to add control stiffness to the system. The control stiffness keeps the mover close to a desired location while a disturbance or noise frequency sweep (chirp) is added to the system. Due to the ZOH behaviour of the sensor, the derivative of the sensor signal sampled at the controller cycling frequency of 250 Hz, is either zero or close to infinity. The derivative action can thus not be used to increase the phase margin of the system. A basic PI controller is designed with a bandwidth of just below 1 Hz. This controller is limited by the phase lag of the plant in combination with the phase lag due to the time delay of the sensor system.

The control parameters were obtained through heuristic tuning, by increasing K_p until stable oscillatory behaviour was found. The K_p value was subsequently halved to the value found, and integral action was added to achieve a steady state tracking error of zero within 20 s. Figure 6.5 and Figure H.1 show the response of: the plant acquired by system identification in the next section, the controller, the open-loop response and the closed-loop response. The translational system has a bandwidth of 0.87 Hz and a phase margin of 40°. The rotational system has a bandwidth of 0.57 Hz and a phase margin of 43°. The parameters and stability margins of the basic controller are found in Table 6.1.

Table 6.1: Basic controller: parameters and stability margins

	translation	rotation
bandwidth	0.87 Hz	0.57 Hz
K_p	40	$57 \times 10^{-3} = 1 \times 10^{-3} \cdot \frac{360}{2\pi}$
K_i	20	$72 \times 10^{-3} = 1.25 \times 10^{-3} \cdot \frac{360}{2\pi}$
phase margin	40°	43°
gain margin	2.4	3.8

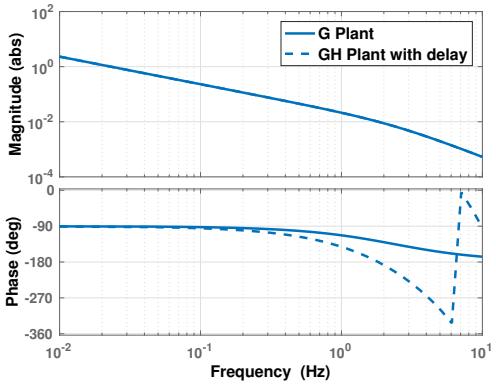

(a) Plant response $G_{\mathrm{x,y}}$

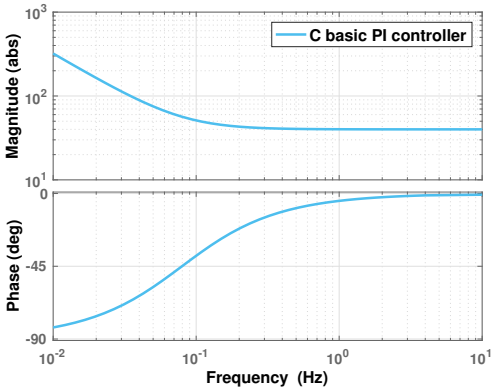

(b) Controller $C_{\mathrm{x,y}}$, $f_\mathrm{c} = 0.87\,\mathrm{Hz}$

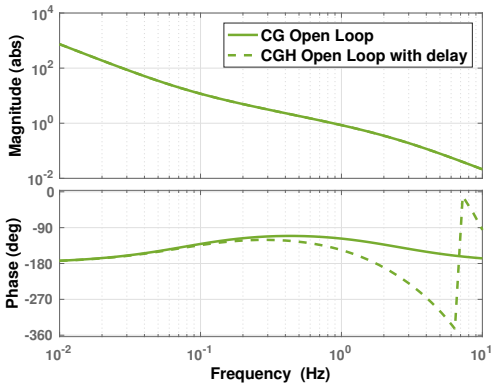

(c) open-loop response $L_{\mathrm{x,y}}(j\omega) = CG$

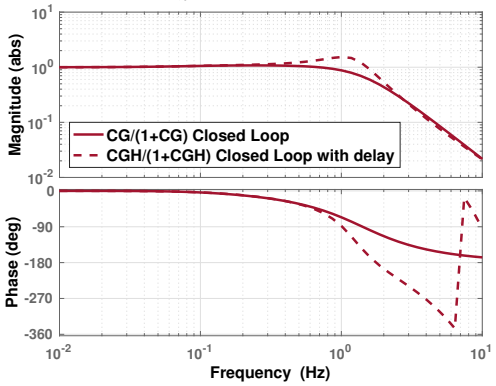

(d) closed-loop response $T_{\mathrm{x,y}}(j\omega) = \frac{CG}{1+CG}$

Figure 6.5: The translational motions are controlled with basic PI controllers with a bandwidth of 0.87 Hz.

6.7 Closed-loop system identification

In order to determine the plant dynamics G and sensor dynamics H, disturbance d and noise n frequency sweeps were injected to the system in separate measurements. The outputs y and $\hat{y}$ were measured with reference sensors and the image sensor system, respectively. The reference sensors used to measure the three planar DOFs were two Micro-Epsilon optoNCDT1300-20 sensors and one optoNCDT1401-5. These are analog position sensors with a range of 20 mm and 5 mm. The range is inversely proportional to the resolution of the sensor. The schematic overview is seen in Figure 6.6 and the measurement setup in Figure 6.7.

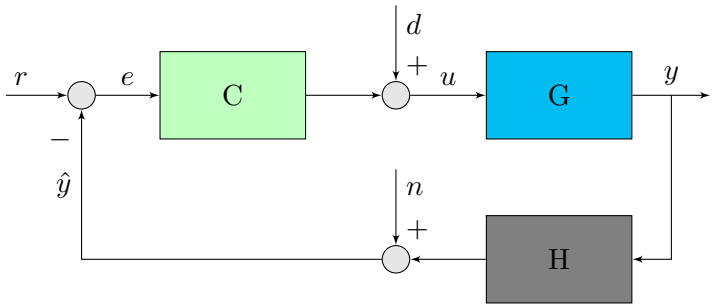

Figure 6.6: System identification overview. The system consists of the controller C, plant G and sensor dynamics H transfer functions. Disturbance d and noise n frequency sweeps were injected to the system. The outputs y and $\hat{y}$ were measured with laser triangulation sensors and the image sensor system, respectively.

Disturbance was injected as a force with an amplitude of 0.1 N or a torque with an amplitude of 0.01 Nm. Noise was injected with an amplitude of 0.5 mm in translation or 0.5° in rotation. These amplitude levels were chosen to give a small but detectable response. The frequency sweeps start at 0.01 Hz and have a maximum frequency of 100 Hz after 30 s. They are injected as a logarithmic sweep to give a good response over the entire range of frequencies. The sweeps are performed bidirectionally: the sweep starts at its lowest frequency and after reaching its maximum frequency it returns to its lowest frequency again.

A separate Arduino was used to simultaneously log the analog signals of the laser triangulation sensors, and the digital signals of the frequency sweep and camera sensor system. An overview of the data acquisition can be found in Figure 6.8. The Raspberry Pi sends the current digital chirp and sensor signals from the control system to the Arduino over SPI. Simultaneously the Arduino measures the analog signals from the laser triangulation sensors. These measurements were sent over Serial to a laptop for recording. This resulted in the data of the camera sensor system and the laser triangulation sensors being synchronised. Since the ADC of the Arduino is adding noise to the measurements, additional measurements were done with a NI-DAQ USB-6008 data acquisition unit. These measurements were synchronised to the data logged by the Arduino by adjusting the starting time of the measurement.

By performing a Fast Fourier Transform (FFT) of the injected input to the measured output, four frequency responses were found:

$$\frac{\hat{y}}{d} = \frac{GH}{1+CGH} \tag{6.11}$$

$$\frac{y}{d} = \frac{G}{1+CGH} \tag{6.12}$$

$$\frac{\hat{y}}{n} = \frac{1}{1+CGH} \tag{6.13}$$

$$\frac{y}{n} = -\frac{CG}{1+CGH} \tag{6.14}$$

$$\tag{6.15}$$

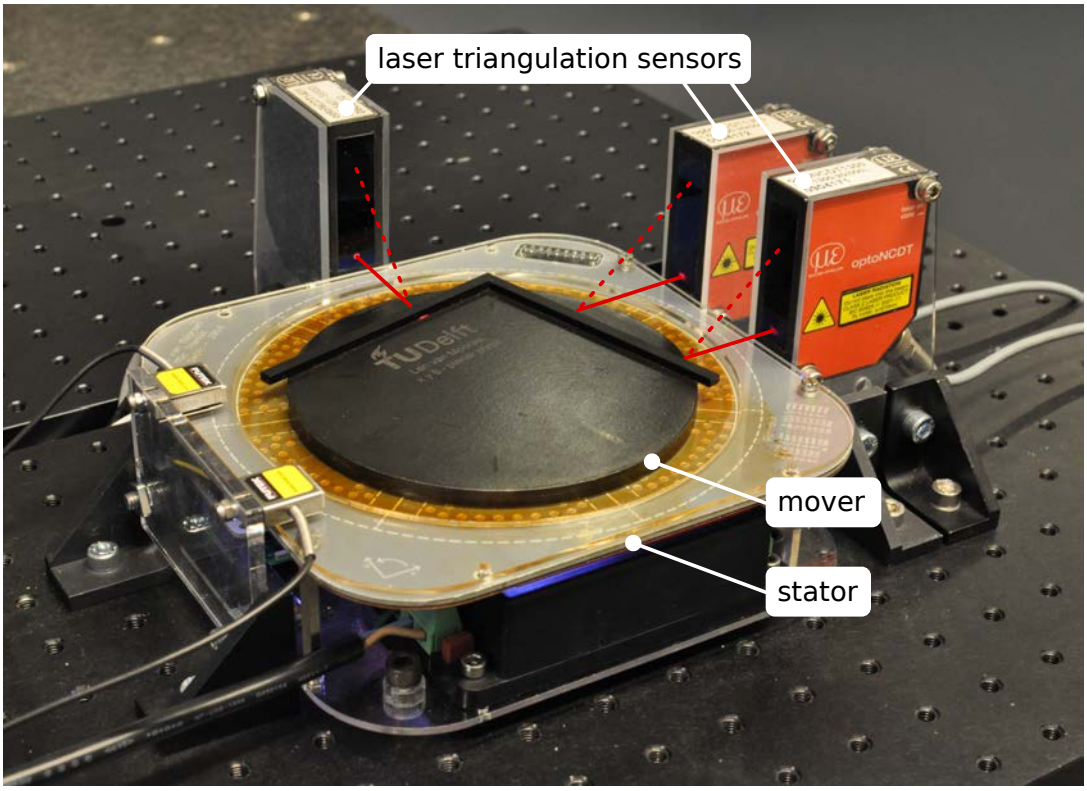

Figure 6.7: Measurement setup with reference sensors used to measure the three planar DOFs: two Micro-Epsilon optoNCDT1300-20 sensors and one optoNCDT1401-5. The two 20 mm range sensors were used to measure the x-position and θ-rotation of the mover. The 5 mm range sensor was used to measure the y-position of the mover. The light path of the lasers is indicated in red. The stage has a size of 175x175x50 mm.

These responses for translation and rotation are shown in Figure 6.9 and Figure H.2 respectively. The plant is modelled as a mass damper with $m = 0.464\,\text{kg}$ and $c = 6.9\,\text{Ns/m}$ and the sensor dynamics are modelled as a time delay $H = e^{-\tau s}$ with $\tau = 80\,\text{ms}$. The model matches closely to the measured response, except for the phase of $\frac{\hat{y}}{n}$.

The delay found is higher than the 60 ms delay of the image-recognition algorithm measured in subsection 3.4.5. This could be caused by communication delays between the different software programs. An overview of the software can be found in Appendix I. The sensor signal is first sent from the sensor system algorithm over UDP to the control system, and sent from there over UDP and SPI to the Arduinos. Since the controller is running with a sample time of 4 ms, entering the control system and exiting the control system consequently induces a delay of 4 ms. The UDP and SPI protocols also introduce additional delays. The additional delay of 20 ms is however also present in the final setup and should be taken into account when designing an advanced controller.

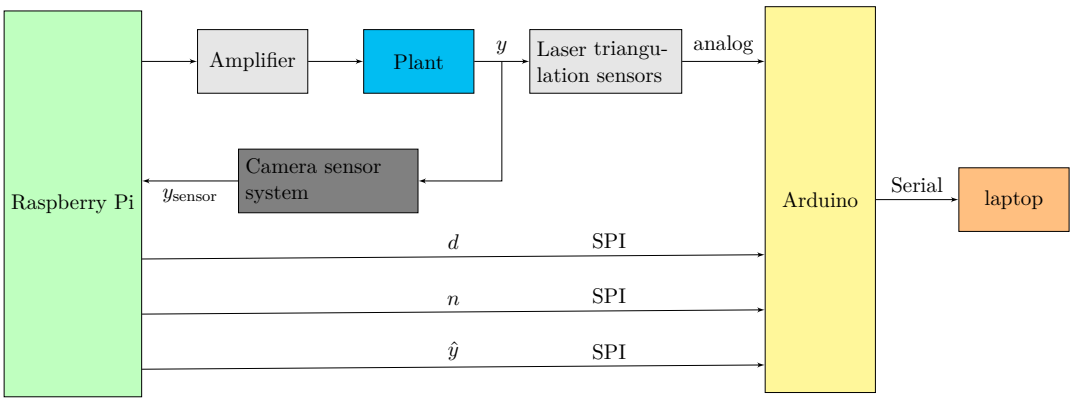

Figure 6.8: Data acquisition overview used for system identification. An Arduino was used to simultaneously measure the analog signals of the laser triangulation sensors and the digital signals from the Raspberry Pi. A laptop was used to log the data.

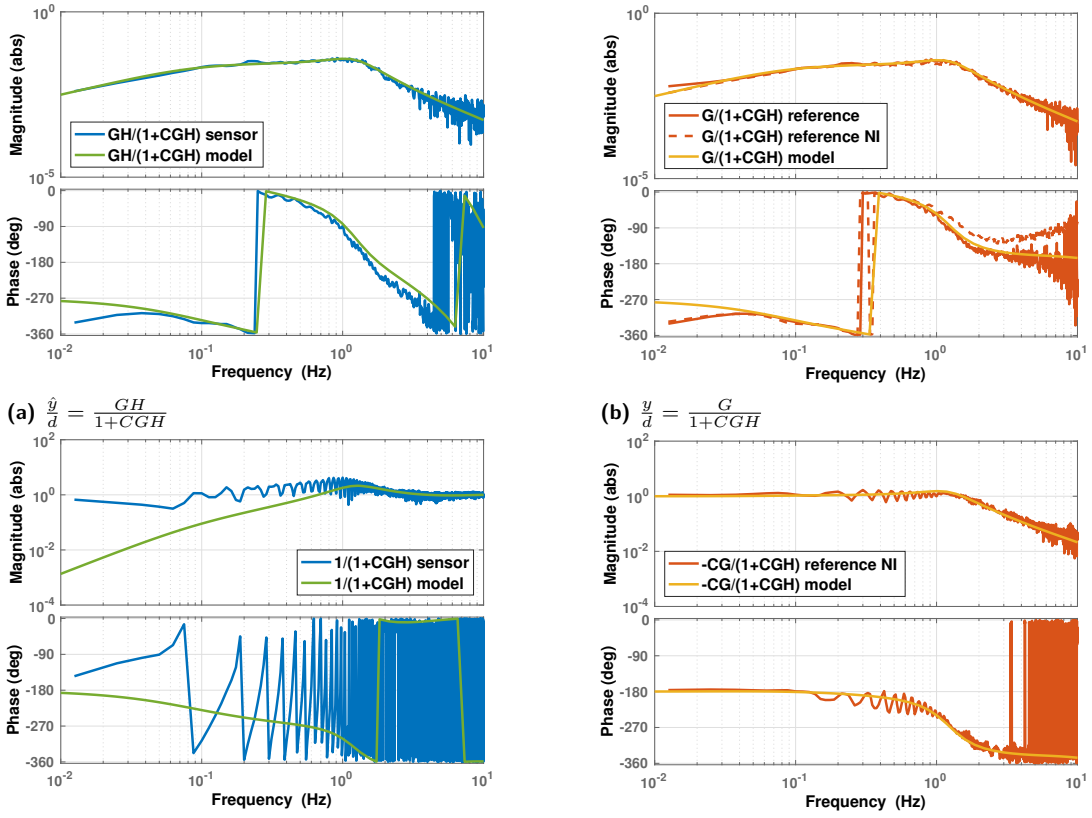

(a) $\frac{\hat{y}}{d} = \frac{GH}{1+CGH}$ (b) $\frac{y}{d} = \frac{G}{1+CGH}$

(c) $\frac{\hat{y}}{n} = \frac{1}{1+CGH}$ (d) $\frac{y}{n} = -\frac{CG}{1+CGH}$

Figure 6.9: The translational response was identified with a frequency sweep injected to the system as disturbance or noise. Outputs of the camera sensor and reference were recorded. By taking an FFT of these signals the response was found. The responses match closely to the modelled dynamics, except for the phase of $\frac{\hat{y}}{n}$, using $m = 0.464\,\text{kg}$, $c = 6.9\,\text{Ns/m}$ and $H = e^{-\tau s}$ with $\tau = 80\,\text{ms}$.

By further post-processing the measured data, the sensor dynamics and plant dynamics can be obtained.

Sensor dynamics are obtained with:

$$H = \frac{\frac{GH}{1+CGH}}{\frac{G}{1+CGH}} = \frac{\frac{\hat{y}}{d}}{\frac{y}{d}} = \frac{\hat{y}}{y} \tag{6.16}$$

Plant and sensor dynamics are be obtained with:

$$GH = \frac{\frac{GH}{1+CGH}}{\frac{1}{1+CGH}} = \frac{\frac{\hat{y}}{d}}{\frac{\hat{y}}{n}} = \frac{n}{d} \tag{6.17}$$

These responses are seen in Figure 6.10. A close match between the measured and modelled dynamics is observed.

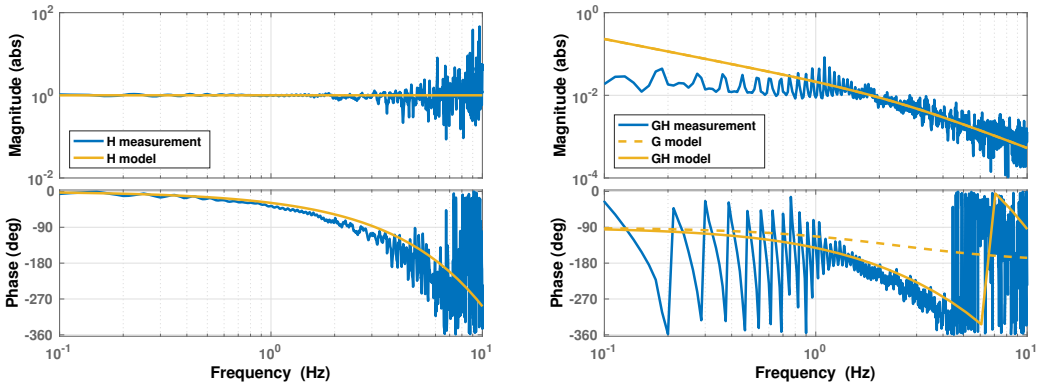

(a) Sensor dynamics H **(b)** Sensor and plant dynamics GH

Figure 6.10: Sensor dynamics H and sensor and plant dynamics GH. A close match between the measured and modelled dynamics is observed.

It is noteworthy that the damping value $c = 6.9\,\mathrm{Ns/m}$ used in the modelled plant deviates by only a factor 3.5 from the value $24\,\mathrm{Ns/m}$ calculated theoretically in Appendix B. This shows that the damping in translation can be predicted relatively well, notwithstanding the fact that the model only contains the damping of the ferrofluid, whereas in the real setup additionally Eddy current damping due to the copper heat sink is present.

6.8 Advanced control

With the plant and sensor dynamics identified, a more advanced controller can be designed to increase the bandwidth. The sensor system was seen to have two downsides:

- the sensor signal has a delay
- the sample rate is low creating ZOH output behaviour

Additionally, the delay and sample rate are not constant due to the sensor algorithm using a different amount of time for each image.

A common approach to handle delay is to implement a model-based controller to estimate the current sensor signal using a model of the plant. A common approach to get rid of the sharp edges of the stepwise changing signal is by implementing

a low-pass filter, called a reconstruction or anti-imaging filter. This filter causes an additional phase shift in the frequency domain, corresponding to a time delay in the time domain. This should be taken into account in the stability analysis. By combining a reconstruction filter with a model-based controller a novel advanced controller was designed to compensate for the downsides of the sensor system.

6.8.1 Model Predictive Control

A conceptual model predictive controller is seen in Figure 6.11. By using the output of the controller as an input to a state estimator containing a model of the plant, the position of the mover is estimated.

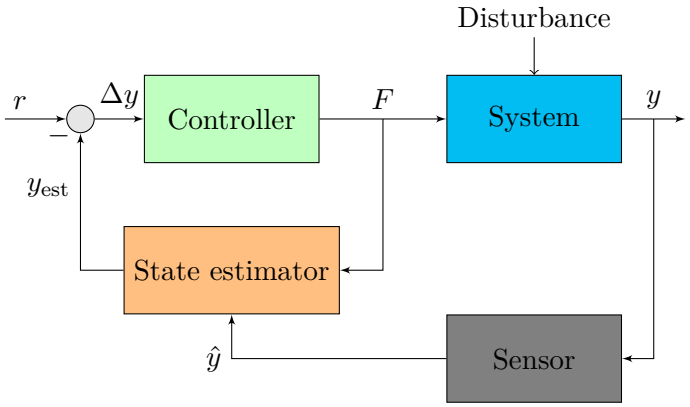

Figure 6.11: Model predictive controller for one DOF. The output F is used as an input to the state estimator that contains a model of the plant. Based on F and the sensor signal $\hat{y}$ the position of the mover is estimated as y_{est}.

Classical predictive control: Smith predictor

A Smith predictor [17] is a model-based controller for plants with a long dead time. An overview of a Smith predictor is seen in Figure 6.12. A model of the plant G_m is used to estimate the current state of the output of the system. The estimated signal is used for direct feedback. Delaying this signal with the delay ($e^{-s\tau_m}$) of the plant, $\hat{y}_m$ is obtained. Comparing $\hat{y}_m$ to the actual signal $\hat{y}$, allows the error between model and measurement to be observed. This signal is additionally used as (delayed) feedback signal, to correct for modelling errors and disturbances.

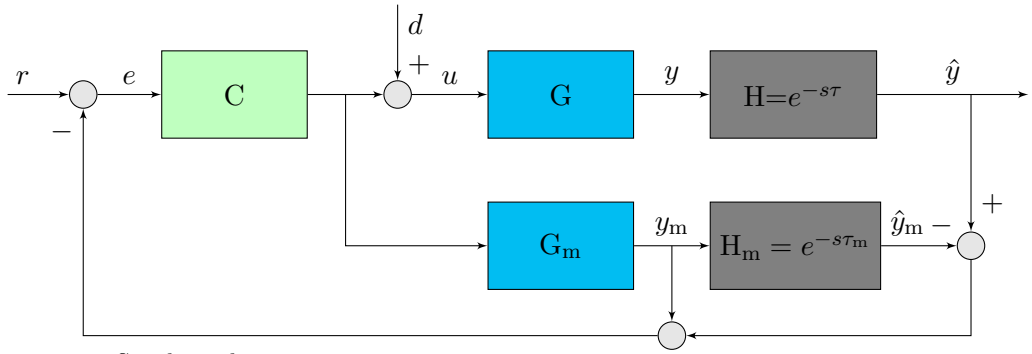

Figure 6.12: Smith predictor.

Combined with disturbance observer

The basic controller does not observe continuous disturbances to the system, such as a disturbance created by gravity if the stage is not perfectly level. The error between the model and the real measurement is used to compensate for this disturbance. A Proportional and Integral (PI) controller is used to integrate the error and the output of this controller is used as feedforward to the plant. The Smith predictor with disturbance observer is presented in Figure 6.13.

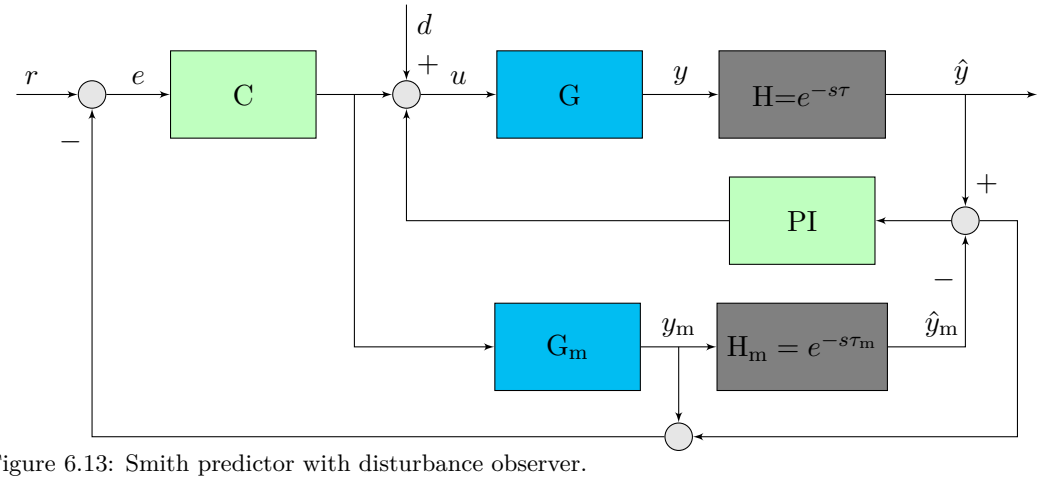

Figure 6.13: Smith predictor with disturbance observer.

6.8.2 Reconstruction filter

Theoretically the bandwidth of a control system is limited by the Nyquist-Shannon sampling theorem, stating that the sampling rate of the sensor should be at least twice as high as the maximum frequency range. For a good control performance however, a rule of thumb is to choose a sampling rate of about 5 to 10 times the control bandwidth of the controlled system. Based on this rule of thumb and the sensor system sampling rate of 16 Hz, the control system would be limited to 1.6 or 3.2 Hz, not considering the additional delay.

The sampling rate creates a stepwise changing signal. This is known as zero-order-hold behaviour. To create a smooth signal, the sharp edges can be filtered by a low-pass filter, called reconstruction filter. The filter however causes an additional phase shift [16]. The implementation of and signals created by a reconstruction filter are shown in Figure 6.14 and Figure 6.16a.

Figure 6.14: Reconstruction filter using a low-pass filter (LPF).

Additionally, the ZOH behaviour can be changed into first-order-hold (FOH) behaviour (Figure 6.15), by extrapolating the difference between the last and before-last sample. This improves the quality of the reconstructed signal (Figure 6.16b). The signal reconstructed by means of ZOH and low-pass filtering is a good estimate of the original signal, it is however delayed.

The transfer function of the LPF used is:

$$LPF(s) = \frac{20}{20 + s} \tag{6.18}$$

The additional time delay is:

$$\tau_{\text{LPF}} = 50\,\text{ms} \tag{6.19}$$

The following rules of thumb are found from theoretical simulations:

- The product of the sample rate and the filter coefficient should be chosen equal to 1.2. For a sample rate of 60 ms the filter coefficient should be $20\,\text{s}^{-1}$. The filter becomes: $\frac{1}{1+s/20}$.
- The product of the filter coefficient and τ_{LPF} should be equal to 1. For a filter coefficient of $20\,\text{s}^{-1}$, $\tau_{\text{LPF}} = 50\,\text{ms}$.

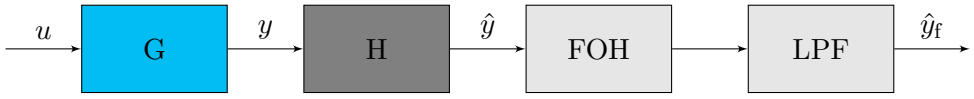

Figure 6.15: Reconstruction filter using a first-order-hold (FOH) element and a low-pass filter.

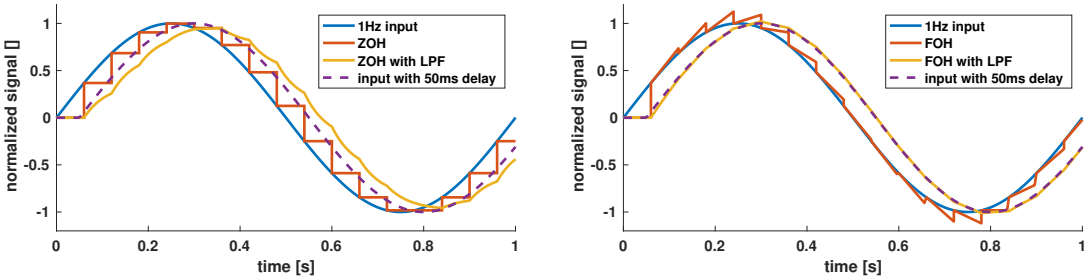

Figure 6.16: Reconstruction filters using an LPF: $\frac{1}{s/20+1}$. (a) ZOH signal. (b) FOH signal. The ZOH filtered signal closely matches the input signal, it is however delayed by 50 ms.

6.8.3 Smith predictor with reconstruction filter

By combining the Smith predictor with a reconstruction filter, a novel advanced controller is designed (Figure 6.17). By measuring when the signal of the sensor system is updated, a FOH element with variable sample rate was created. The sensor-system delay τ_{m} is measured using the time difference between the last and second last sample. Additionally a delay of 20 ms was added to the measured sensor system delay of approximately 60 ms, as was revealed by system identification of the sensor dynamics. An extra delay is added to compensate for the phase shift of the low-pass reconstruction filter. The controller is implemented for one translational DOF.

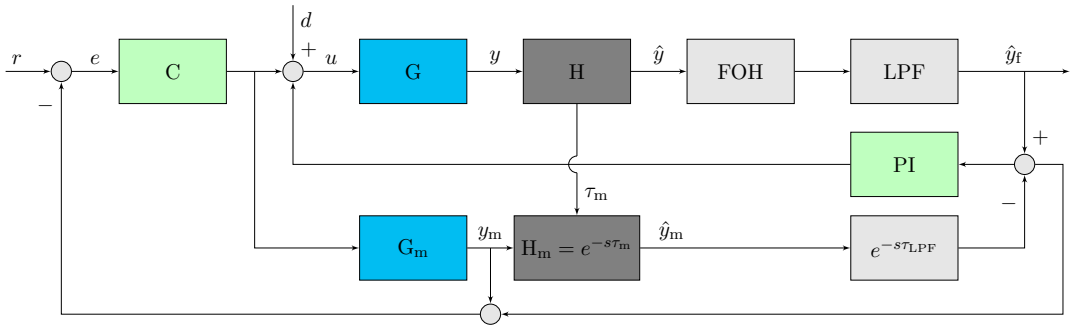

Figure 6.17: Novel advanced controller: Smith predictor combined with a disturbance observer and a reconstruction filter using a first-order-hold element. The time delay of the sensor system τ_m is continuously measured. An additional time delay is added to compensate for the phase shift created by the low-pass filter.

6.9 Advanced controller

The advanced controller is a tamed PID controller tuned using the four guidelines of section 6.5. Additionally a low-pass filter with a cutoff frequency of three times the bandwidth is added directly before the controller, to attenuate high frequencies. The parameters and stability margins are found in Table 6.2. The modelled responses corresponding to the advanced controller are seen in Figure 6.18 and Figure H.3.

Table 6.2: Advanced controller: parameters and stability margins

	translation	rotation
bandwidth	10.1 Hz	10.2 Hz
K_p	628	1.3
K_i	3.9×10^3	8.2
K_d	30.0	6.2×10^{-3}
τ_f	5.3×10^{-3}	5.3×10^{-3}
phase margin	48°	51°
gain margin	5.0	5.1

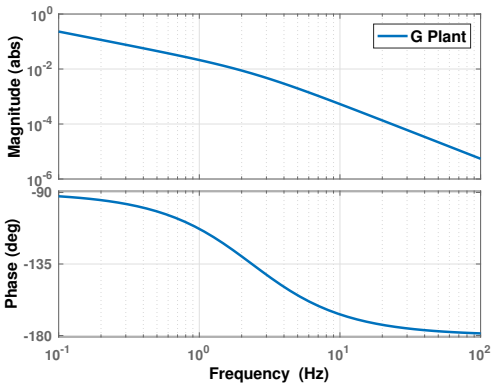

(a) Plant response $G_{\mathrm{x,y}}$

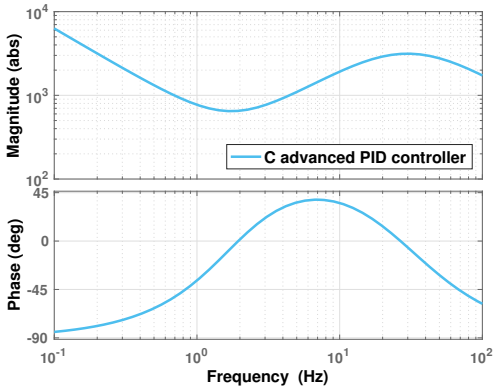

(b) Controller $C_{\mathrm{x,y}}$, $f_{\mathrm{c}} = 10\,\mathrm{Hz}$

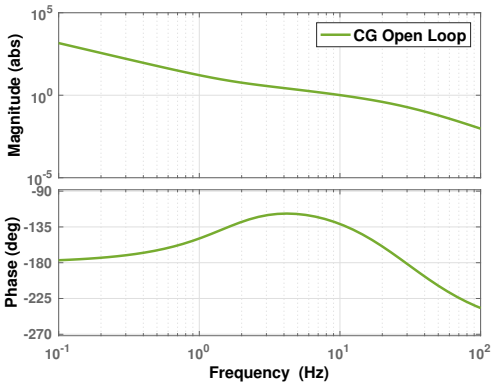

(c) open-loop response $L_{\mathrm{x,y}}(j\omega) = CG$

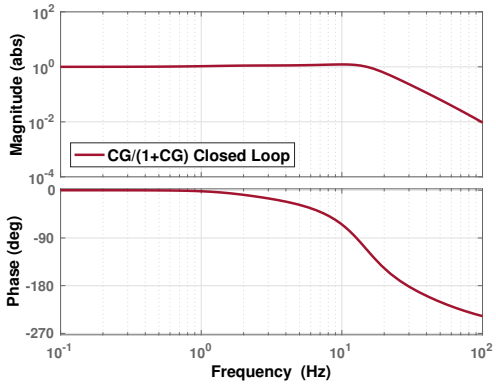

(d) closed-loop response $T_{\mathrm{x,y}}(j\omega) = \frac{CG}{1+CG}$

Figure 6.18: Advanced controller: The translational motions are controlled with a tamed PID controller with an additional low-pass filter. It has a bandwidth of approximately 10 Hz.

6.10 Conclusion

A controller was designed to control the position of the three Degrees of Freedom of the mover. A pseudo-inverse of the position-dependent force transformation matrix was implemented to calculate the currents for the seven coils. A basic PI controller was implemented and achieved a sub-Hertz bandwidth. Closed-loop system identification was performed using the basic PI controller. The identified plant allowed a novel advanced controller to be designed based on a Smith predictor and a reconstruction filter, to handle the delay and zero-order-hold behaviour of the sensor system. The advanced controller was tuned for a bandwidth of 10 Hz.

7
Results

After implementing the controllers results can be obtained. The performance of the demonstrator is measured in terms of step response, positioning precision, positioning stability and linearity.

To measure the performance, the same reference sensors were used as in section 6.7. However, the data is now only logged by the NI-DAQ system. These signals were not used as feedback for the control system. The two sensors with a range of 20 mm have a resolution of 12 or 13 µm. These two sensors are used to measure the position x and rotation θ of the mover. The two sensors are placed at 50.5 mm from each other, therefore the angular resolution is 0.0136° or 0.0147°. The sensor with a range of 5 mm has a resolution of 3.3 µm and is used to measure the y-position of the mover.

7.1 Step response

The step response of the system was measured in order to evaluate the performance of the demonstrator stage. A step response is used since a step contains an infinite range of frequencies. 5 mm and 10° steps were performed and the rise and settling times were measured (Figure 7.1).

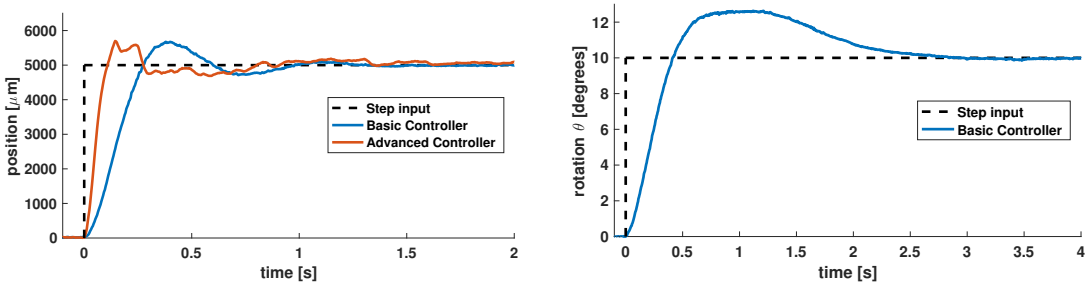

(a) Translation **(b)** Rotation

Figure 7.1: Step response with basic and advanced controller. (a) The basic controller in translation creates a step response with a rise time t_r of 0.19 s and a settling time t_s of 0.93 s. The advanced controller has a rise time of 0.072 s and a settling time of 1.59 s. The rise time is increased due to the 10 Hz bandwidth of the advanced controller. The settling time is expected to reduce with improved tuning. (b) The basic controller in rotation creates a step response with t_r=0.29 s and t_s=2.5 s. The step response could be improved by tuning the controller and implementing the advanced control scheme for rotation.

7.2 Positioning precision

To determine the repeatability of the system, multiple steps of the same size were made as seen in Figure 7.2. The position at the end of each step was measured with the reference sensors, and the measured position was compared to the desired position.

To create a large data set, 25 steps of 20 sec were made and the error between the desired position and final position was calculated. Step sizes of 1 mm and 20° were used. The spread in the data gives a measurement for the precision of the stage (Figure 7.3).

For translation the probability density function shows a normal distribution. The 3σ precision is 16.0 µm, meaning that 99.7 % of the steps are within a range of ±16 µm. For rotation the stage is controlled to within the resolution of the reference sensors.

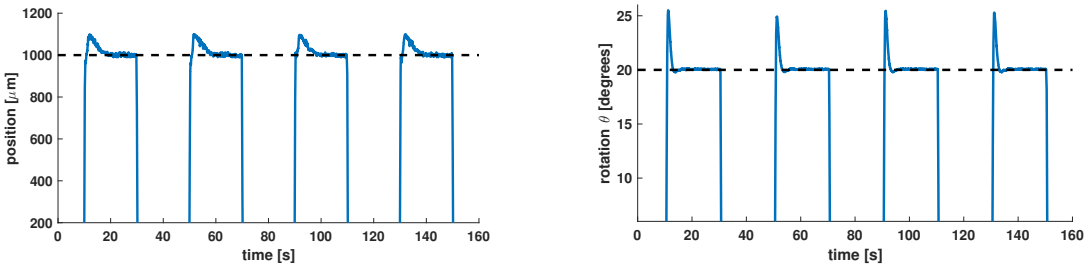

(a) Translation **(b)** Rotation

Figure 7.2: Steps of 1 mm and 20° for measuring the repeatability of the system, by means of laser triangulation sensors.

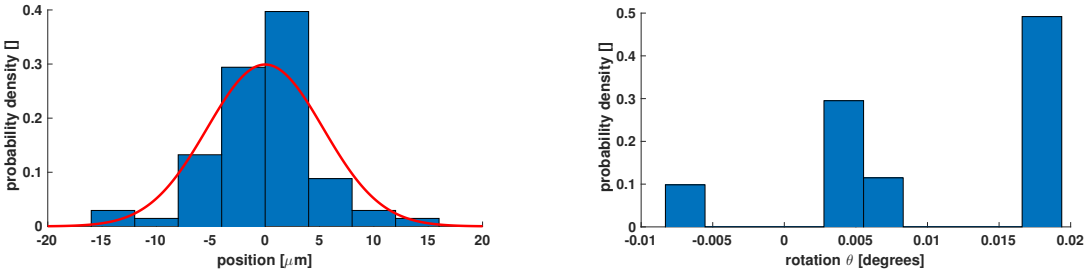

(a) Translation: $3\sigma = 16.0$ µm **(b)** Rotation

Figure 7.3: Positioning precision with basic controller. The positioning precision (3σ) is 16.0 µm for translation. In rotation the resolution of the 20 mm range laser triangulation sensors, in combination with the 12-bit NiDAQ-6008 data acquisition unit, is too low to fit a normal distribution. Worst case the positioning precision (3σ) would be 0.028°. Two bars are created around the mean instead of one. This is caused by the slight difference in resolution of the two sensors. Two 5 mm sensors and a 16-bit NiDAQ-6211 would be preferred to measure the precision more accurately.

7.3 Positioning stability

Next to positioning precision, it is also important to know how close the mover stays to the desired location once the mover has arrived at that location. The positioning stability is determined by positioning the mover at a desired location, and measuring its position over 300 s with the reference sensors. It includes the measurement stability, actuator stability and the disturbances. The error is normally distributed (Figure 7.4). The 3σ positioning stability in translation is 14.3 µm. This means that 99.7 % of the time the mover stays within ± 14.3 µm of the desired location. It is noteworthy that this is only a fraction of the sensor resolution of 83 µm. The 3σ positioning stability in rotation is 0.046°.

Number of bins: 160x120

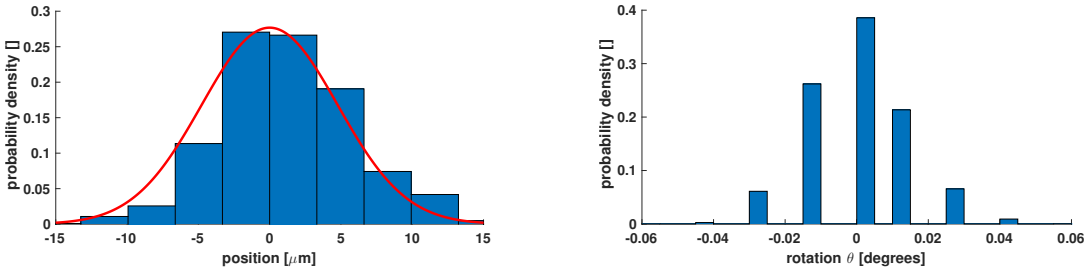

(a) Translation: $3\sigma = 14.3$ µm **(b)** Rotation: $3\sigma = 0.046°$

Figure 7.4: Positioning stability with basic controller measured over 300 s. The resolution of the laser triangulation sensors is low in rotation. A better measurement could be obtained with the setup described in Figure 7.3.

Number of bins: 320x240

Additional measurements were performed with 320x240 image sensor bins. The results is a 3σ positioning stability of 8.7 µm and 0.048°. It is noteworthy that this is only a fraction of the sensor resolution of 42 µm seen by each pixel bin.

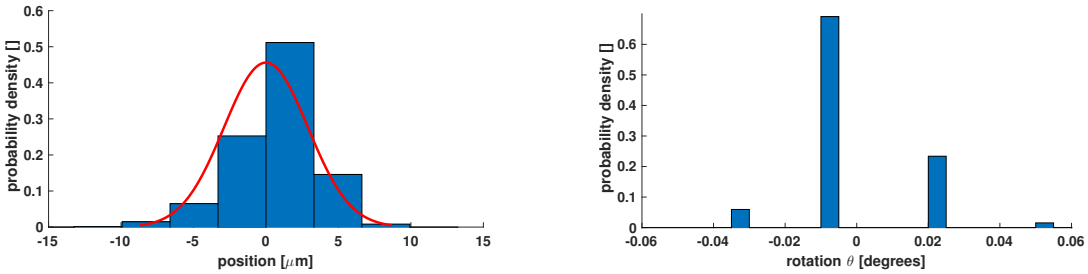

(a) Translation: $3\sigma = 8.7$ µm **(b)** Rotation: $3\sigma = 0.048°$

Figure 7.5: Positioning stability with basic controller and 320x240 pixel bins. The positioning stability in translation improves by a factor 1.6 by increasing the number of pixel bins with a factor 2. No improvement was seen in rotation, this could however be caused by the low resolution of the reference sensors for rotation.

7.4 Linearity

In order to assess the linearity of the step response, consecutive steps of 1 mm and 1° were made from −10 mm to 10 mm and −10° to 10° (Figure 7.6). The large range sensors are now also used to measure the translations. The 20 mm range of the reference sensors is limiting the measurement at −10 mm.

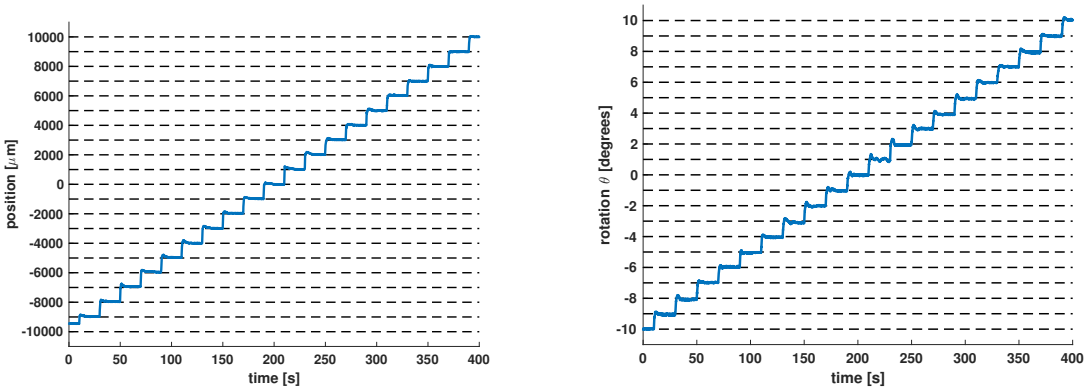

(a) Translation **(b)** Rotation

Figure 7.6: Consecutive steps of 1 mm and 1° using the basic controller.

Additionally, different step sizes are made, by making a steps from the central $x = 0$ $y = 0$ position and returning to that position after 20 s (Figure 7.7). The overshoot increases linearly with step size.

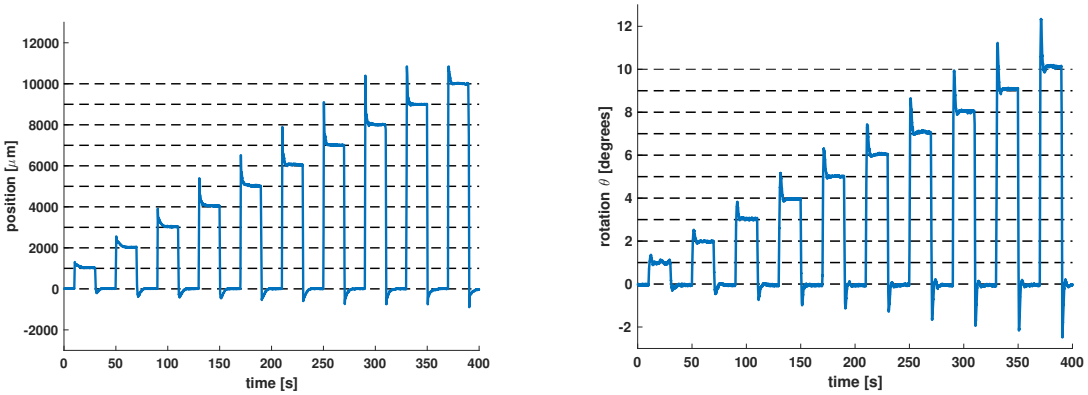

(a) Translation **(b)** Rotation

Figure 7.7: Step response for different step sizes using the basic controller.

7.5 Specifications of the complete system

Table 7.1: Specifications of the complete system

Performance	
Translational settling time (5 mm step)	0.93 s
Rotational settling time (10° step)	2.5 s
Precision (3σ) in translation	16.0 µm
Precision (3σ) in rotation	$\approx 0.028°$
Stability (3σ) in translation (160x120 bins)	14.3 µm
Stability (3σ) in translation (320x240 bins)	8.7 µm
Stability (3σ) in rotation	$\approx 0.048°$
Sensor system	
Resolution	83 µm/bin
Number of bins	160x120
Measurement dispersion (3σ) in translation	3.9 µm
Measurement dispersion (3σ) in rotation	0.0177°
Sample rate	≈ 16 Hz
Time delay	≈ 60 ms
Depth of Field	4.0 mm
Actuator	
Resistance coils	1.8 - 2.0 Ω
Inductance coils @ 1 kHz	24.1 - 26.5 µH
Average tangential motor constant per coil	0.25 N/A
Average rotational motor constant per coil	12.5×10^{-3} Nm/A
Amplifier	
Type	H-bridge
PWM frequency	20 kHz
Maximum current	1.9 A
Physical properties	
Translational range	30 mm
Rotational range	∞
Moving stage mass	464 g
Moving stage moment of inertia around z	9.5×10^{-4} kgm^2
Moving stage diameter	152 mm
Moving stage thickness	6 mm
Actuator dimensions	175x175x2 mm
Overall stage dimensions	175x175x50 mm

8

Discussion

Comparison to previous research. Within the portfolio of micrometre stages built to date, sensor systems are the main cost drivers and limiting factors of these stages. Sensors should be the main consideration for decreasing overall cost. Comparing the present stage to previous work of Café [1], Mok [2] and Habib [3], a number of differences is observed:

- The stage developed in this thesis has a significantly lower cost (€300) than the research stage developed by Café (€35000) and Habib (€800). The cost is however higher than the stage by Mok (€200).
- The positioning precision (3σ) of 16.0 µm is lower than that achieved by Mok, Habib and Café (9.7 µm, 0.2 µm and 10 nm respectively).
- On the other hand, this system is able to translate 30 mm compared to 9 mm or 10 mm in the other stages, allowing larger surfaces to be scanned.
- Compared to the achieved 360° rotation of Habib, the present stage is able to freely rotate for an infinite number of rotations, which is not seen in any of the other developed stages.

Limitations. In this stage the sensor algorithm is limiting the performance of the complete system. Some of the limitations of the system are listed:

- The image sensor was chosen for its low cost, high number of pixels, absolute performance and full insight in the software used to extract position information from the captured images. The required computational effort by the image-recognition software, running on the processor of the microcontroller, limits the resolution and bandwidth of the system.
- Additionally, the sensor system is limited in speed due to blurring of the images when the target translates within the time that the image sensor captures light for one image. With the current magnification, the image sensor system was tested to track speeds of 480 mm/s, which is more than sufficient for this system.

- Without the sensor system limitations, probably the communication delays between the different software programs and the control system would be the limiting factor for control bandwidth.
- Due to the desired bandwidth of 10 Hz, it was regarded unnecessary to perform a mechanical vibration analysis of the system. The out-of-plane stiffness of the PCB could however limit the system at higher frequencies.

Scaling. The developed knowledge allows the system and its subsystems to be scaled for applications in other fields of research.

- The range of the sensor system could be increased without affecting the resolution, with a larger target.
- The resolution of the sensor system could be increased up to the diffraction limit of the optical system by:
  - simultaneously decreasing the size of the markers and increasing the optical magnification;
  - increasing the number pixels of the image sensor.
- The translational range of the actuator could be increased by scaling its total planar dimensions.
- An actuator with a different number of coils and permanent magnet poles could be designed by using the developed design guidelines.

Future perspective. Computational power per unit cost is expected to follow Moore's law. Future microcontroller generations will thus be able to process a larger number of pixel bins at increased sample rates. The increase in positioning stability performance from 14.3 µm to 8.7 µm with number of pixel bins, demonstrates a promising future for precise positioning systems based on low-cost image-recognition sensor systems.

9

Conclusion

Looking into the possibilities to decrease the cost of precision stages, a low-cost three degree of freedom micrometre precision stage using a single image sensor was successfully designed, implemented and validated. The stage can complete an infinite number of rotations and has a translational range of 30 mm in two directions. The system has a 3σ positioning precision of 16.0 µm in translation and 0.028° in rotation and a 3σ positioning stability of 8.4 µm and 0.046° was achieved. This is an especially good result considering a component cost of €300. The combination of infinite rotation and relatively large translational range at a low cost has resulted in a one-of-a-kind positioning system. The performance of the system is mainly limited by the sensor system and the corresponding image-recognition algorithm.

Sensor system. The image sensor is by itself incapable of detecting positions. An absolute three Degree of Freedom micrometre-precision sensor system was developed by combining the image sensor with an absolute position target consisting of an array of 2D barcodes, and a state-of-the-art image-recognition algorithm developed at the university of Córdoba. The computational effort of the image-recognition algorithm causes a time delay and a relatively low sample rate. A trade-off between sensor resolution, sample rate and delay resulted in a sensor system with the following specifications: 120x160 pixel bins; an optical resolution of 83 µm, increased with pixel interpolation to a 3σ measurement dispersion of 3.9 µm in translation and 0.018° in rotation; an average sample rate of 16 Hz; an average time delay of 60 ms and a depth of field of 4 mm.

Actuator. To actuate the stage, coils are used as Lorentz actuators, embedded in a stator PCB. The coils create Lorentz forces on permanent magnets in the mover. An analysis of 60 axial flux permanent magnet motor (AFPMM) concepts was performed and design guidelines were established for an AFPMM that is able to translate in x, y, which is not possible in conventional AFPMMs. The concept with 7 coils and 8 magnet poles was selected for implementation. A semi-analytical model was developed to determine the force that each coil exerts on the mover at every location and rotation. Force measurements revealed a 12 % deviation between the model and reality.

Ferrofluid bearing A ferrofluid bearing was implemented between mover and PCB stator. The bearing has a vertical stiffness of 800 kN/m and a load capacity of 100 N. This is 100 times the required load capacity.

Control system. The demonstrator stage is a Multiple-Input Multiple-Output system. A transformation matrix decouples this system into three Single-Input Single-Output systems, decreasing the control complexity. A commutation strategy to translate and rotate the mover at every location was successfully implemented in the control scheme, by using the results of the semi-analytical model in the transformation matrix. Current controllers based on H-bridges compensated for the increase in resistance of the coils with temperature. Non-linear behaviour of the H-bridge and current sensor was observed and corrected for with lookup tables.

Increased control bandwidth. The sample rate and delay of the sensor limits the control bandwidth of the system to below 1 Hz. This behaviour was experimentally validated and mainly caused by the image-recognition algorithm. The control bandwidth has been successfully increased to 10 Hz by implementing a novel model predictive controller (MPC). The MPC uses an observer and a reconstruction filter to compensate for the 60 ms delay and 16 Hz sample rate of the sensor system. The observer uses information about the system inputs, sensor dynamics, reconstruction filter and dynamic properties of the plant. Instead of using the delayed sensor information, the estimation of the actual position was used to control the system.

Low-cost system. In line with the low-cost requirements, the system has been implemented to run standalone on low-cost microcontrollers. A Raspberry Pi is used for the image-recognition algorithm, complete control system and communication with the image sensor, actuator and human machine interface. Two Arduinos based on Cortex-M0 architecture were used for the designed current controllers of the amplifier.

Summary. A standalone, high-performance positioning system was built, by using a low-cost image sensor. Full system knowledge of the mechatronic design and trading off specifications of the individual subsystems allowed high overall performance to be achieved. The project was completed with a final component cost of €300, in a time frame of eleven months. Although the image-recognition algorithm is limiting the system, the cost of computing power decreases annually. The feasibility of using an image-recognition sensor system for micrometre positioning was demonstrated in this thesis, and shows a bright future for micrometre positioning systems based on this technology.

Bibliography

[1] M. Café, *Design of a 6 DOF nanometer ferrofluid stage.* (2014), unpublished, Master Thesis.

[2] G. Mok, *The design of a planar precision stage using cost effective optical mouse sensors,* (2015), unpublished, Master Thesis.

[3] H. Habib, *Design of a three degrees of freedom planar precision stage using a single position sensitive detector,* (2015), unpublished, Master Thesis.

[4] S. van Veen, *Ferrofluid bearings,* (2013), unpublished, Master Thesis.

[5] S. Garrido-Jurado, R. Muñoz-Salinas, F. J. Madrid-Cuevas, and M. J. Marín-Jiménez, *Automatic generation and detection of highly reliable fiducial markers under occlusion,* Pattern Recognition **47**, 2280 (2014).

[6] S. F. Ray, *Applied Photographic Optics: Lenses and Optical Systems for Photography, Film, Video, Electronic and Digital Imaging.*, ISBN 0-240-51540-4 (Focal Press, 2002).

[7] L. Larmore, *Introduction to Photographic Principles* (Dover Publications, Inc. New York, 1965).

[8] A. Mahmoudi, N. A. Rahim, and W. P. Hew, *Axial-flux permanent-magnet machine modeling, design, simulation and analysis,* Scientific Research and Essays **6**, 2525 (2011).

[9] M. Osa, T. Masuzawa, N. Omori, and E. Tatsumi, *Radial position active control of double stator axial gap self-bearing motor for pediatric VAD,* Bulletin of the JSME **2** (2015).

[10] Y. Okada, K. Dejima, and T. Ohishi, *Radial position control of a pm synchronous type and induction type rotating motor,* Industry Applications Society Annual Meeting (1994).

[11] S. Lampaert, *Planar ferrofluid bearings modelling and design principles,* (2015), unpublished, Master Thesis.

[12] R. S. Li, *Optimization of thermal via design parameters based on an analytical thermal resistance model,* Thermal and Thermomechanical Phenomena in Electronic Systems , 475 (1998).

[13] K. J. Åström, *Introduction to control,* (2004), Lund Institute of Technology, Lund University.

[14] K. J. Åström and T. Hägglund, *PID controllers: Theory, Design and Tuning* (Instrument Society of America, 1995).

[15] M. Araki, *PID Control,* Control Systems, Robotics, and Automation **II** (1984).

[16] R. Munnig Schmidt, G. Schitter, and J. van Eijk, *The Design of High Performance Mechatronics.*, ISBN: 978-1-60750-825-03 (IOS Press, 2012).

[17] O. J. M. Smith, *A controller to overcome dead time,* ISA Journal **6**, 28 (1959).

[18] P. Samarin, K. B. Kent, R. Herpers, and T. Saitov, *Fiducial Marker Detection Using FPGAs*, Master's thesis, University of New Brunswick, Fredericton, NB, E3B5A3, Canada (2013).

[19] P. A. Tipler and G. Mosca, *Physics for Scientists and Engineers* (W. H. Freeman and Company, 2008).

A

Paper proposals

In this appendix the abstracts of two proposals for papers are presented.

A.1 Axial Flux Permanent Magnet Motor Design for Large Translations

Abstract

This paper presents the design and analysis of a novel planar axial flux permanent magnet motor. The motor was designed for translations of 30 mm in x and y and an infinite range of rotation in θ_z. A planar ferrofluid bearing was used to constrain the remaining three Degrees of Freedom. A conceptual analysis was performed to characterise forces generated in x and y and torque in θ_z. 60 actuator concepts were considered in this analysis, with different number of stator coils and magnetic poles. One of these concepts was chosen for implementation, after considering manufacturing and implementation constraints. The motor constants of this setup and the pseudo-inverse matrix necessary for required force and torque to coil current transformation were theoretically calculated. The force generated by the prototype was measured for model validation.

A.2 XY∞: Implementation of a Vision System for Position Control of a Planar Precision Stage

This paper presents the implementation of the image sensor and image-recognition algorithm for position control of the planar stage.

Targeted journal: Sensors and Actuators A: Physical
Targeted conference: Vision, Robotics & Motion

Abstract

Given the current lack of cost-effective vision sensors for precise 3DOF planar positioning systems and a foreseen increase in speed and resolution of image-recognition algorithms, a relevant research topic is the feasibility study of micrometre positioning using vision. In this research, a low-cost vision system was designed and implemented on a three degrees-of-freedom planar precision stage for digital microscopy applications. An axial flux permanent magnet motor design capable of large translations in x and y and infinite rotations in θ_z was designed in previous research. For the vision system, a cost-effective image sensor and open-source image-recognition algorithm were selected. The image-recognition algorithm detects the position of a marker map placed on the bottom of the moving stage. The algorithm is able to determine 6 degrees-of-freedom position information, however only the three planar degrees of freedom are required. The delay of the sensor system is not constant and restricts the bandwidth of the system significantly: 0.8 Hz was achieved with a PI controller. A Smith predictor was implemented to compensate for this dynamically changing delay. Furthermore, the zero-order-hold behaviour of the sensor was filtered with a first-order-hold reconstruction filter. A novel controller was developed by compensating for the additional delay of the reconstruction filter with the Smith predictor. A PID controller designed with this technique achieved a bandwidth of 10 Hz. The results obtained on the practical setup are provided and discussed.

B

Ferrofluid damping

B.1 Translation

The translational damping coefficient c of a ferrofluid bearing can be calculated according to [11]:

$$c = \eta_\mathrm{r}\eta_\mathrm{b}\frac{A_\mathrm{bearing}}{h_\mathrm{bearing}} \tag{B.1}$$

where η_r is dependent on the velocity profile of the fluid and is approximately 4 in case of trail formation. η_b is the ferrofluid viscosity, h_bearing is the fly height of the bearing and A_bearing the total contact area of the bearing:

$$A_\mathrm{bearing} = w_\mathrm{ferrofluid}(\pi(D_\mathrm{outer} + D_\mathrm{inner}) + m \cdot \frac{D_\mathrm{outer} - D_\mathrm{inner}}{2}) \tag{B.2}$$

where $w_\mathrm{ferrofluid}$ is the width of each ferrofluid line segment, D_outer and D_inner are the outer and inner diameter of the magnet ring and m is the number of poles.

With, $\eta_\mathrm{r} = 4$, $\eta_\mathrm{b} = 0.25\,\mathrm{Pas}$, $m = 8$, $D_\mathrm{outer} = 120\,\mathrm{mm}$, $D_\mathrm{inner} = 60\,\mathrm{mm}$, and assuming a fly height of $h_\mathrm{bearing} = 100\,\mu\mathrm{m}$ and a ferrofluid line thickness of $w_\mathrm{ferrofluid} = 3\,\mathrm{mm}$, a damping of $c = 24\,\mathrm{Ns/m}$ is obtained.

B.2 Rotation

The torque T needed to overcome rotational damping can be calculated according to [11]:

$$T = \int\int_S \tau r^2 dr d\theta = \int\int_S \eta\frac{r\omega}{h}r^2 dr d\theta = \eta\frac{\omega}{h}\int\int_S r^2 dr d\theta = \eta\frac{\omega}{h}J = \eta_\mathrm{r}\eta_\mathrm{b}\frac{\omega}{h}J \tag{B.3}$$

where$\int\int_S$ is the surface integral, defined by the radius r and the angle θ, ω is the angular velocity of the bearing and J the polar moment of inertia[1] of the ferrofluid contact.

The rotational damping coefficient C_rot can thus be calculated with:

$$C_\mathrm{rot} = \frac{T}{\omega} = \eta_\mathrm{r}\eta_\mathrm{b}\frac{J}{h} \tag{B.4}$$

[1]The polar moment of inertia J should not be confused with moment of inertia (rotational equivalent for mass) or area moment of inertia (used to calculate bending of a beam).

For a mover with m magnet poles, the polar moment of inertia consists of three terms:

$$J = J_{\text{inner}} + m \cdot J_{\text{line}} + J_{\text{outer}} \tag{B.5}$$

where J_{inner}, J_{line}, J_{outer} correspond to the inner ring, the m line segments and the outer ring of the bearing.

Special care must be taken to decide which η_{r} is used for what part of the polar moment of inertia. When the disk rotates around its centre, the ferrofluid at the inner and outer ring has a triangular velocity profile, corresponding to $\eta_{\text{r}} = 1$, whereas the line contacts have a velocity profile consisting of a triangle combined with a parabola, corresponding to $\eta_{\text{r}} = 4$.

This gives the following rotational damping coefficient:

$$C_{\text{rot}} = \frac{\eta_{\text{b}}}{h}(J_{\text{inner}} + m \cdot 4J_{\text{line}} + J_{\text{outer}}) \tag{B.6}$$

Rings The polar moment of inertia of the inner and outer rings can be calculated with:

$$J_{\text{ring}} = \frac{\pi}{4}(r_2^4 - r_1^4) \tag{B.7}$$

This gives: $J_{\text{inner}} = 2.55 \times 10^{-7}\,\text{m}^4$ and $J_{\text{outer}} = 2.04 \times 10^{-6}\,\text{m}^4$

Line segments To calculate the polar moment of inertia of the lines, the perpendicular axis theorem is used. It relates J_{z} to the area moments of inertia about the other two mutually perpendicular axes: I_{x} and I_{y}. $J_{\text{z}} = I_{\text{x}} + I_{\text{y}}$

$$I_{\text{x}} = \frac{(r_{\text{outer}} - r_{\text{inner}})w_{\text{ferrofluid}}^3}{12} \tag{B.8}$$

for the long axis of each line segment and

$$I_{\text{y}} = \frac{w_{\text{ferrofluid}}(r_{\text{outer}}^3 - r_{\text{inner}}^3)}{3} \tag{B.9}$$

for the short axis of each line segment.

Assuming $w_{\text{ferrofluid}} = 3\,\text{mm}$ gives a polar moment of inertia of each line segment of $J_{\text{line}} = 1.89 \times 10^{-7}\,\text{m}^4$.

Assuming a bearing fly height of 100 µm, a total rotational damping coefficient C_{rot} of $20.9 \times 10^{-3}\,\text{Nms/rad}$ is obtained. The inner ring contributes $0.6 \times 10^{-3}\,\text{Nms/rad}$, the outer ring $5.1 \times 10^{-3}\,\text{Nms/rad}$ and the eight line segments $15.1 \times 10^{-3}\,\text{Nms/rad}$.

C

Image sensor technology and hardware selection

C.1 Image sensor technology

Two types of image sensor technology have been generally applied in past 50 years: CCD and CMOS. The CCD was invented in 1969 and measures the movement in electrical charge. Pixels of a CCD are represented by capacitors, which allow the conversion of incoming photons to electron charges. The CCD is used to measure the movement in charge. They are widely applied in professional and scientific applications where high-quality imaging is required. CMOS is a technology for constructing Integrated Circuits (ICs) and was patented in 1967. The name CMOS is also used to describe the image sensors made with this technology. Different than CCD, the electrons captured in the capacitors are not shifted to a single output amplifier, but transformed into a voltage directly at the source. The difference in working principle is shown in Figure C.1. By using additional electronics per pixel, the image information can be read in less time than with CCD sensors. The disadvantage is that additional space is required for the electronic circuit. This light sensitive area of a CMOS sensor is thus smaller than that of a CCD sensor, and less photons can be collected.

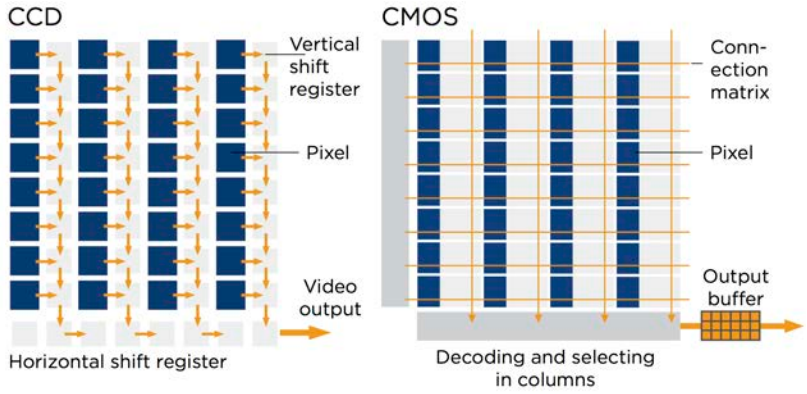

Figure C.1: Design of a CCD sensor (left) and a CMOS sensor (right)[a]. The charge is shifted pixel by pixel in the CCD sensor. In the CMOS sensor the charge of each pixel is directly converted to a voltage and measured. This makes the CMOS much faster.

[a] http://s.baslerweb.com/media/documents/BAS1505_White_Paper_Benefits_of_CMOS_EN.pdf

In applications with less accurate demands, such as digital cameras CMOS technology has traditionally been mainly applied. Although CMOS was known to acquire lower quality images than CCD, the quality of CMOS has significantly increased. Due to its lower power consumption and lower cost than CCD, much research has gone into improving the CMOS technology. Therefore, in case of consumer electronics, CMOS is nowadays outperforming CCD on almost any performance indicator.

C.2 Hardware selection

Hundreds of different image sensors are available all with different characteristics. Since this research is about high precision position sensors, resolution is important for static performance and frame rate for dynamic performance. Additionally a goal is to build a standalone system using a low-cost microcontroller and the image sensor needs to be commercially available and easy to implement.

After a market research the OmniVision OV5640 and OV5647 5 MP sensors with a maximum frame rate of 120 fps were found. The OV5640 module is specified to work with the pcDuino Acadia based on a 1.2 GHz ARM Cortex A9 processor. However, the Camera Serial Interface (CSI) connector on the camera module was found not to be compatible with the microcontroller. The Raspberry Pi V1.3 camera module is based on the OV5647 and uses a Mobile Industry Processor Interface (MIPI) Camera Serial Interface Type 2 (CSI-2) to connect with the Raspberry Pi. The Raspberry Pi 3B is based on a 1.2GHz ARM Cortex A53, which has slightly lower performance than the pcDuino. This sensor and microcontroller were selected for conceptual validation. Apart from a compatible sensor module, an additional advantage of using the Raspberry Pi over the pcDuino is a larger online community working on software for this hardware. During the project a new 8 MP camera sensor module V2.1 for the Raspberry Pi was released based on the Sony IMX219 and was used for the final design. The V2.1 camera is preferred over the V1.3 camera, since at a frame rate of 90 fps, limited by the sensor software, the V2.1 camera reads out 1280x720 pixels, in contrast to the 640x480 pixels of V1.3. More pixels can be used for a higher resolution of the sensor system.

The Raspberry Pi is limiting the data transfer between the image sensor and the microcontroller processor. MIPI CSI-2 version 1.01 supports up to four data lanes, where each lane has a maximum of 1 Gbps bandwidth, however only two are available for the Raspberry Pi. With these two MIPI data lanes, a maximum frame rate of 120 fps can be achieved. However, if all 4 MIPI lanes of the V2.1 camera would be used, the sensor is able to produce an image size of 1280x720 pixels at 198 fps or 960x540 pixels at 240 fps. The Raspberry Pi Compute Module has two CSI-2 interfaces. Interface 0 has two data lanes, interface 1 has four data lanes. If higher frame rates are essential, the Raspberry Pi Compute Module 3 could be used, which is expected to be released in the beginning of 2017.

D

Detailed magnetic design

In this appendix the detailed considerations for the magnetic design are described.

D.1 Magnet thickness

For precise positioning systems it is important to have high accelerations so that the mover arrives at the desired position within a short time.

The accelerations of the mover are related to its mass and the force acting on the mover, by Newton's Second Law of Motion:

$$a = \frac{F}{m} \tag{D.1}$$

The goal is thus to select magnets which can create the highest force per unit mass of the rotor. Since the generated force is linearly related to the magnetic flux density, magnets with the highest flux density per unit mass are the objective. In general magnets with smaller thickness have a higher flux density per unit mass than thicker magnets. Therefore the thinnest available magnets, with appropriate dimensions in the xy-plane, were selected. The selected magnets are 4 mm thick.

D.2 Steel backing plate

A steel backing plate is used for the following reasons:

- The magnetic flux density at the coils is increased.
- The magnetic flux density is decreased above the mover: the location where the object of interest for microscopy is placed. This allows lightly magnetic objects to be easily removed from the mover.
- The different magnet segments can be easily assembled into one ring.
- The stiffness of the mover is significantly increased, which comes at only a small reduction in achieved accelerations, since the forces are simultaneously increased.

The steel backing plate reduces the reluctance path of the magnetic flux. The magnetic flux Φ can be calculated with [16]:

$$\Phi = \frac{\mathcal{F}}{\mathcal{R}} = \frac{B_\mathrm{r} l_\mathrm{m}}{\mu_0 \mathcal{R}} \tag{D.2}$$

where $\mathcal{F}$ is the magnetomotive force and $\mathcal{R}$ the reluctance of the flux path. B_r and

l_m are the remanent flux and length of the magnet from north to south pole and μ_0 is the magnetic permeability equal to $4\pi \times 10^{-7}\,\mathrm{NA}^{-2}$.

An analogy between an electric and a magnetic circuit can be made: voltage is equivalent to magnetomotive force $\mathcal{F}$, resistance to reluctance $\mathcal{R}$ and current to magnetic flux Φ. Since the relative permeability of steel is a factor 5000 higher than that of air, the magnetic flux and therefore the magnetic flux density $\mathbf{B}$, can be increased below the mover with a steel backing plate.

The steel backing plate however also increases the mass of the mover. The steel backing plate increases the mass more than the force, thereby reducing the maximum accelerations. A trade-off was made and a steel backing plate of 2 mm was selected. It increases the mass of the mover from its magnet mass of 253 g to 464 g.

D.3 Single or double rotor

Single and double rotor configurations are seen in literature. A single rotor single stator configuration was selected, however a double rotor single stator configuration was also investigated. By doubling the number of magnets, the flux density could be increased by a factor 3 and maximum accelerations by a factor 1.5. The location of the ferrofluid was also simulated in COMSOL. The ferrofluid spreads over the mover, increasing its contact area with the stator and thereby significantly increasing the damping coefficient of the bearing. A single rotor configuration was chosen for its lower cost, lower number of parts, better serviceability and lower damping compared to a double rotor configuration.

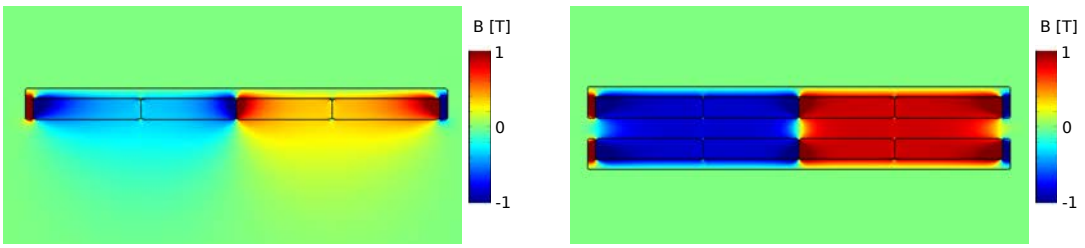

(a) Single rotor **(b)** Double rotor

Figure D.1: Magnetic flux density in z-direction for a single and double rotor configuration. The single rotor configuration has an average magnetic flux density in z-direction of 0.35 T. For the double rotor configuration it is 0.85 T. This increases the possible forces by a factor 2.4, however the accelerations only increase by a factor 1.2 due to the additional mass. The 20 % increase in acceleration comes at a twice as high component cost.

D.4 Distance between rotor and stator

Increasing the distance between the rotor and stator leads to a lower magnetic flux density in z-direction at the location of the coils,. Increasing the distance thus reduces the Lorentz forces that can be generated by the coils. The mover is therefore placed as close as possible to the stator.

D.5 Steel ring and ferrofluid location

The location of the ferrofluid is defined by the magnetic field intensity, the load that the bearing has to carry and the applied amount of ferrofluid. Since the magnetic field intensity is highest where a north and south pole meet, all ferrofluid accumulates at those edges. Therefore no air pockets are formed with a simple steel plate.

By adding steel rings on the inside and outside of the magnet ring, the field intensity is increased at the locations where the magnets meet the rings. Ferrofluid pockets will therefore be formed, increasing the load capacity and stiffness of the bearing. The stiffness of the pockets additionally increases the stiffness for tilt. The steel rings however also decrease the average magnetic flux density in z-direction.

D.5.1 Ferrofluid location defined by the magnetic field intensity

The magnetic field intensity at 1 mm below the rotor is seen in Figure D.2, for a rotor with and without steel rings.

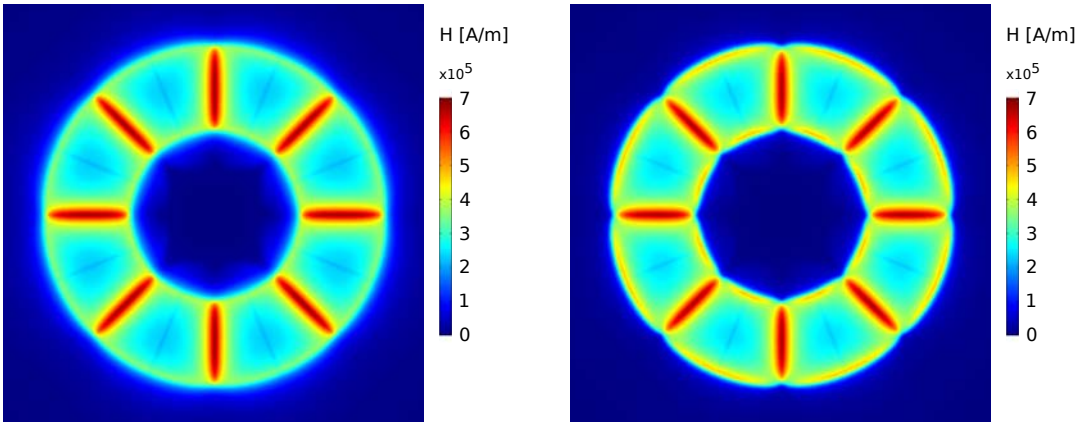

(a) without steel rings **(b)** with steel rings

Figure D.2: Magnetic field intensity H at 1 mm below the rotor, for a configuration without steel rings (a) and with steel rings (b). The location of the ferrofluid is determined by the magnetic field intensity. The ferrofluid accumulates at the red and yellow locations. The steel rings influence the location of the ferrofluid. By adding steel rings to the backing plate, air pockets are formed.

D.5.2 Flux density

Figure D.3 shows that the steel rings reduce the average magnetic flux density in z-direction, due to the opposite flux at the location of the rings. Since the Lorentz force generated by one coil is related to the average magnetic flux density, the steel rings decrease the maximum Lorentz force created by each coil.

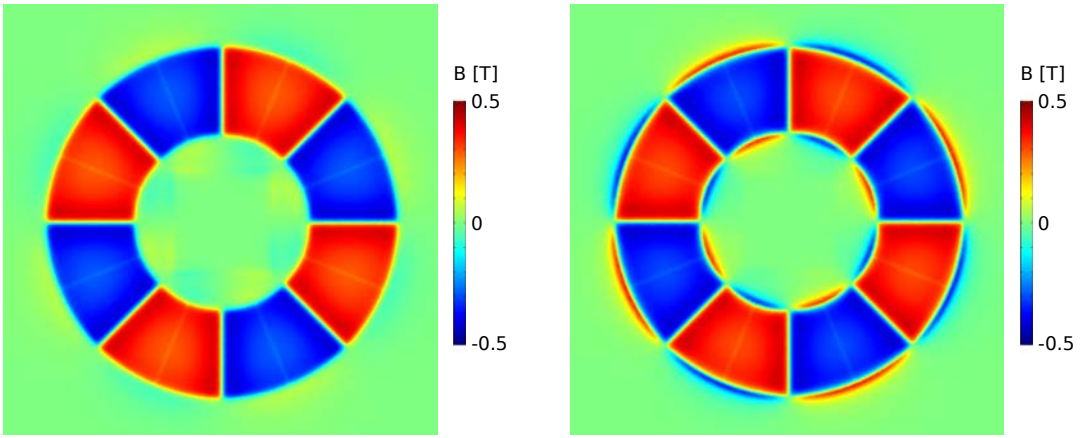

(a) without steel rings **(b)** with steel rings

Figure D.3: Magnetic flux density in z-direction at 1 mm below the rotor, for rotor configurations with and without steel rings of 1 mm. The configuration without steel rings has a higher average magnetic flux density in z-direction. Therefore it allows higher Lorentz forces to be generated.

D.5.3 Negligible influence of current on the ferrofluid location

To calculate the influence of the currents on the location of the ferrofluid, the magnetic field due to an infinitely long straight wire is calculated. The magnetic field strength H, created by a straight winding of length dl, is related to the current I by:

$$I = \oint H dl \tag{D.3}$$

$$I = H 2\pi r \tag{D.4}$$

$$H = \frac{I}{2\pi r} \tag{D.5}$$

where r is the orthogonal distance to the wire segment. The magnetic flux density B is related to the magnetisation M and field intensity by:

$$B = \mu_0 \mu_r (M + H) \tag{D.6}$$

where μ_0 is the magnetic permeability in vacuum and μ_r the relative permeability. In air $M = 0$ and $\mu_r \approx 0$, thus, B due to an infinitely long, straight wire is given by [19]:

$$B = \mu_0 H = \frac{\mu_0 I}{2\pi r} \tag{D.7}$$

For a current of $I = 1\,\text{A}$ and a distance of $r = 0.01\,\text{mm}$, $B = \frac{4\pi \cdot 10^{-7}}{2\pi \cdot 10 \times 10^{-6}} = 2 \times 10^{-2}\,\text{T}$. Since the flux density of the permanent magnets is a couple of orders of magnitude higher ($\approx 0.3\,\text{T}$), the effect of the current on the location of the ferrofluid can be neglected.

D.6 Magnet selection

To create the magnet ring, 16 magnets are needed. Since production can cause a spread in flux density inside each magnet, 24 magnets were ordered. To determine the spread in magnetic flux density between the different magnets, they were placed on a steel plate of 2 mm thick, and the maximum flux density in z-direction of each magnet was measured. The measurements are shown in Figure D.4 and a large spread in magnetic flux density is seen.

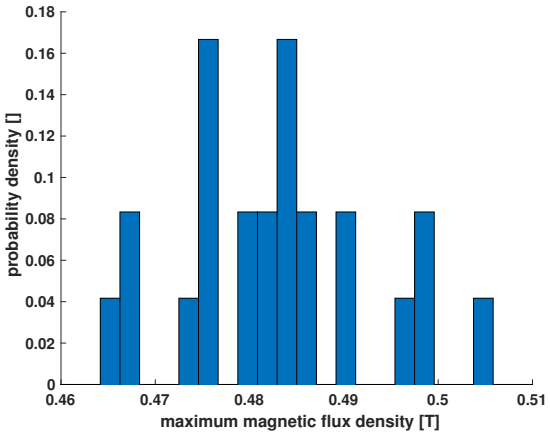

Figure D.4: Probability density function of the maximum magnetic flux density in z-direction of different magnet segments.

There are a number of different ways to cope with this spread in magnetic flux density, based on the scalar equation of the Lorentz force.

$$F = BIl \tag{D.8}$$

- The magnetic flux density B could be equalised at the height of the coils, by changing the z-position of each individual magnet. Additionally B could be adjusted by adding back iron locally to the rotor above weaker magnets, or removed from the rotor above strong magnets.
- The current through each coil could be adjusted for by the control system, to compensate for the weaker magnetic flux density. This would however lead to a control system that is different for different rotors, which is undesirable.
- The magnetic flux density can be evened out by measuring all magnets, and selecting the 16 magnets with the lowest standard deviation. This creates a negligible dependency of the motor constants on the position of the mover due to difference in magnets. This is the solution chosen for the final rotor assembly, since the least mechanical adjustments need to be done to the rotor and the control system can be the same for every 90° of rotation.

E

PCB design for an electromagnetic actuator

This appendix elaborates on the basics of a PCB and the method used to design a stator PCB that meets manufacturing requirements.

E.1 PCB basics

A PCB typically consists of four layers:

- base layer (FR4)
- copper layers
- soldermask
- silkscreen

The **base layer** is usually glass fibre FR4 and adds stiffness and thickness (usually 1.55 mm) to the PCB. On the outside of the FR4, thin **copper** foils are laminated. The thickness of a copper layer is expressed in terms of ounces per square feet (oz). One oz corresponds to 35 µm. Typical thicknesses are 18 µm, 35 µm, 70 µm, and 105 µm. PCBs with 1 to 16 copper layers can be found. A layer of **soldermask** covers the outside copper layers, and adds the green or black colour to the PCB. On top of the soldermask, a layer of **silkscreen** is added. It contains text and symbols for humans to understand the PCB and is usually white.

E.2 Board design

For PCB design two files are used: one schematic that contains information about which connections should be made between components; a board file that contains an actual drawing of the copper and via locations. The schematic design file is very simple and consists only of the connector used to connect the PCB to the amplifiers. The board design file is much more advanced. Both the bottom and top design can be found in Figure 4.13.

E.3 Size of PCB and coils

The size of the PCB is based on the translational range of motion and the size of the magnet segments. The target is sized to allow translations of 30 mm. It has a width of

37.5 mm and a diagonal of 53 mm. Magnet segments are selected that allow the target to be placed inside the magnet ring. These magnets have an inner radius of 30 mm and an outer radius of 60 mm, creating a ring with an outer diameter of 120 mm. The coils are designed such that each magnet segment only "sees" the straight part of a coil at every location. Therefore the coils have a length as long as the range of translation plus the radial length of each magnet. The outer diameter of the straight part of the coils (150 mm) is equal to the outer diameter of the rotor of (120 mm) plus the translational range (30 mm).

E.4 Design approach

The PCB design was performed in Eagle. Since this application is normally used for PCBs for electrical design rather than electromagnetic designs, the Eagle user interface snaps the copper traces to predefined coordinates defined by a square grid that can be adjusted in size. Since the desired coils are not square, it is decided to calculate the position of the windings with Matlab rather than to draw it manually in Eagle. Eagle has a command line interface that allows the traces to be placed.

E.5 Eagle commands

The following eagle commands were used to draw the PCB traces (from x1,y1 to x2,y2) and vias in Eagle:

- wire (x1 y1) (x2 y2); (for a straight trace)
- wire (x1 y1) @+radius (x2 y2); (for a curved trace with positive radius)
- wire (x1 y1) @-radius (x2 y2); (for a curved trace with negative radius)
- via (x y); (to place a via at a specified location)

Additional useful commands were found to be:

- polygon; (to start drawing the border of an area that has to be filled with copper, known as polygon pour)
- name; (to name the created border)
- ratsnest; (to create the polygon pour and shorten unrouted traces, known as airwires)
- ripup @ ; (to remove polygon pour)
- change shape round; (to change the shape of a via to round)

E.6 Meeting the design rules

In order to meet the design rules set by manufacturer Eurocircuits, design rule checks can be automatically performed in Eagle. It is important to note that Eagle is not able to check if two copper traces are too close to each other if they are part of the same signal. The traces that are part of one coil will thus not be checked for enough spacing. This check can be performed as long as the windings are not connected to one another. A design can be check by the performing the following steps:

1. Construct the sides of the coil and the top half
2. Perform the design rule check

3. Remove all traces
4. Construct the sides of the coil and the bottom half
5. Perform the design rule check
6. Add the top half of the coils again to create one full winding.

By designing the location of the traces in Matlab, drawing the traces that meet the design rules is simplified.

E.7 Exporting Eagle files to Solidworks

To see if the design made in eagle matches the CAD design in Solidworks, it is useful to be able to import the Eagle design into Solidworks. The steps necessary are described below.

A small ULP (User Language Program) file called *generate_3d_data_v091.ulp* can be downloaded from `cadsoft.io`. This ULP generates IDF (.emp, .emn) format 3D CAD exchange files from Eagle files (.brd, .sch).

In order to function, the outer dimensions of the board have to be drawn on layer 50. The components should be drawn in layers 57 and 58. The line thickness used specifies the height of the PCB and the components. The thickness and height outputs are defined as 1000 times the width of the lines on these layers.

These layers are not standard, and can be generate using the command line:

- LAYER 50 BoardDimension3D
- LAYER 57 tCAD
- LAYER 58 bCAD

By running the ULP script Eagle can generate .emn and .emp files. These can be imported into Solidworks by using an add-in called Circuitworks. The Add-ins can be found under the Solidworks Tools menu. Circuitworks subsequently allows the user to build a Solidworks model from the .emn and .emp files.

F

PCB connector and pin-out

Table F.1: Molex micro-fit connector pin-out

Pin	Connection	Pin	Connection
1	Coil 1, positive	9	Coil 1, negative
2	Coil 2, positive	10	Coil 2, negative
3	Coil 3, positive	11	Coil 3, negative
4	Coil 4, positive	12	Coil 4, negative
5	Coil 5, positive	13	Coil 5, negative
6	Coil 6, positive	14	Coil 6, negative
7	Coil 7, positive	15	Coil 7, negative
8	Ground	16	Ground

G

Current controller

Two controllers can be implemented on the Arduino to convert the current setpoint received from the Raspberry to a duty cycle D applied to the H-bridge:

1. Feedforward controller (Figure G.1)
2. Feedback controller (Figure G.2)

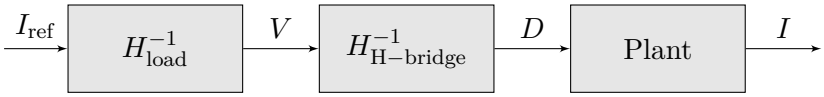

Figure G.1: Feedforward controller

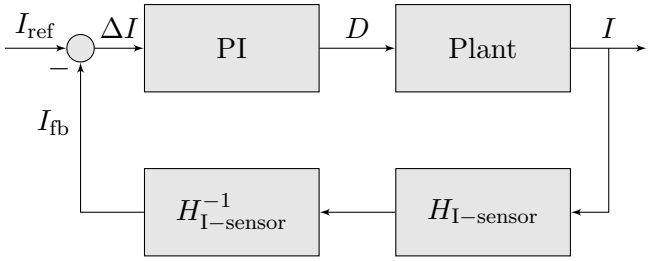

Figure G.2: Feedback controller

The **feedforward controller** uses the inverse of the transfer function of the load (H_{load}), calculated in chapter 5:

$$H_{\text{load}} = \frac{I}{V} \tag{G.1}$$

Also the inverse of the non-linear behaviour between duty cycle and voltage of the H-bridge ($H_{\text{H-bridge}}$) is used. The accuracy of the feedforward controller depends on how well H_{load} and $H_{\text{H-bridge}}$ are known. Especially H_{load} is relatively uncertain, due to the increase in resistance of the coil with temperature and the unknown temperature. Above 0.5 A the temperature of the coil was found to rise significantly above room temperature. $H_{\text{H-bridge}}$ is non-linear, however, well known and repeatable.

The **feedback controller** uses the measured current. The non-linearity between measured current and actual current ($H_{\text{I-sensor}}$) was revealed in section 5.5, and a good fit of the form $y = ax^c + b$ has been found. The feedback controller is thus expected to give a current output corresponding closer to the reference than the feedforward controller. However, the inverse of this transfer function has an infinite

sensitivity at low currents. A small measurement error will therefore create a large change in measured and output current.

For these reasons the feedforward controller was implemented for the entire current range, assisted by the feedback controller for currents above 0.5 A, to compensate for changes in current due to an increase in resistance of the coils. Integral anti-windup of the PI controller was implemented by clamping the output of the controller.

H

Rotational controller

In this appendix the rotational controller design is discussed. The basic controller, system identification and advanced controller are covered. For the translational controller the reader is referred to chapter 6.

H.1 Basic controller

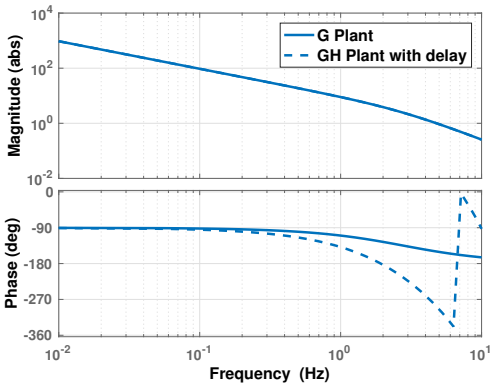

(a) Plant response G_θ

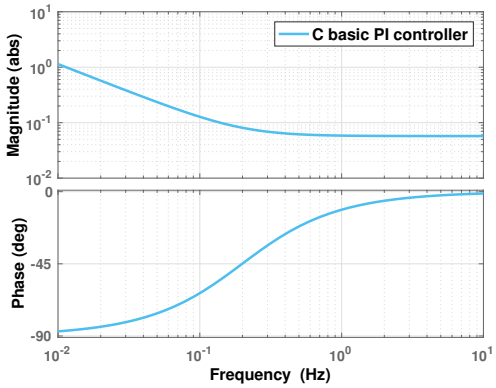

(b) Controller C_θ, $f_c = 0.57\,\text{Hz}$

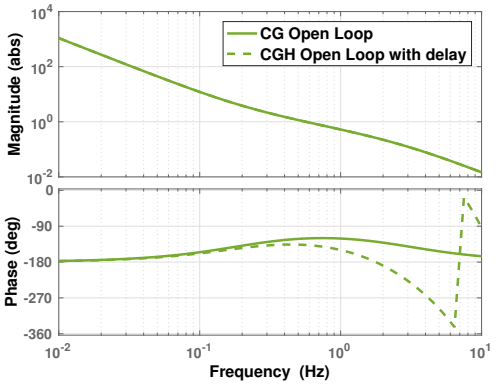

(c) open-loop response $L_\theta(j\omega) = CG$

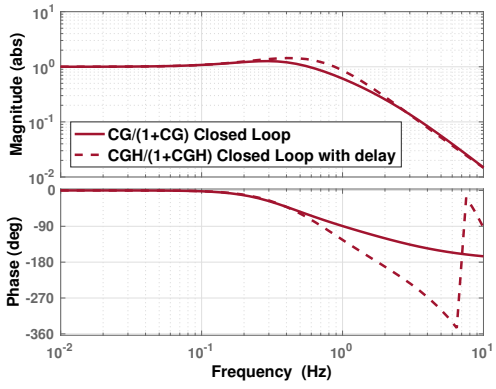

(d) closed-loop response $T_\theta(j\omega) = \frac{CG}{1+CG}$

Figure H.1: The rotational motion is controlled with a basic PI controller with a bandwidth of approximately 0.57 Hz.

H.2 System identification

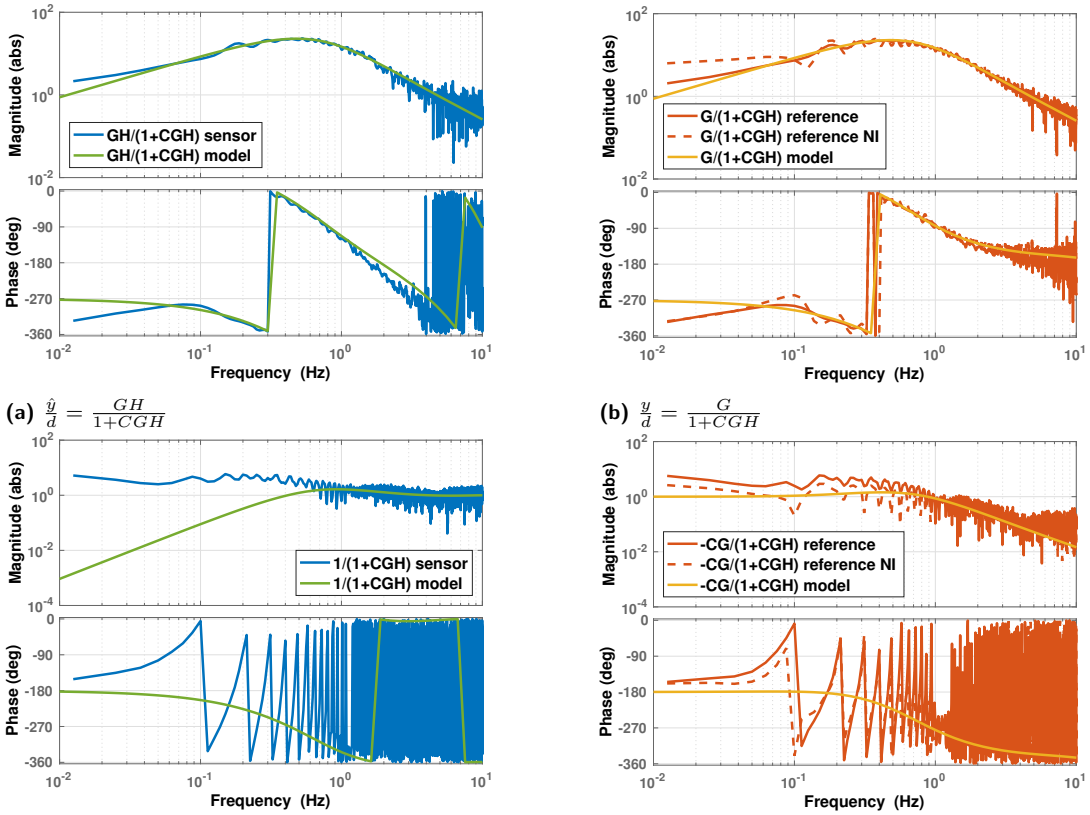

(a) $\frac{\hat{y}}{d} = \frac{GH}{1+CGH}$ **(b)** $\frac{y}{d} = \frac{G}{1+CGH}$

(c) $\frac{\hat{y}}{n} = \frac{1}{1+CGH}$ **(d)** $\frac{y}{n} = -\frac{CG}{1+CGH}$

Figure H.2: The rotational response was identified with a frequency sweep injected to the system as disturbance or noise. The outputs of the camera sensor and reference were recorded. By taking an FFT of these signals the response was found. The responses match closely to the modelled dynamics, except for the phase of $\frac{\hat{y}}{n}$ and $\frac{y}{n}$, using $I = 9.5 \times 10^{-4}\,\mathrm{kgm}^2$, $C = 0.017\,\mathrm{Nms/rad}$ and $H = e^{-\tau s}$ with $\tau = 80\,\mathrm{ms}$.

It is noteworthy that the damping value $C = 0.017\,\mathrm{Nms/rad}$ used in the modelled plant deviates by only a factor 1.25 from the value $0.021\,\mathrm{Ns/m}$ calculated theoretically. This shows that the damping in rotation can be predicted relatively well. The same comments made about Eddy current damping for translation hold for rotation.

H.3 Advanced controller

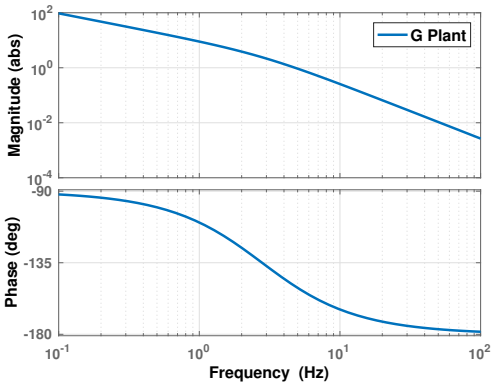

(a) Plant response G_θ

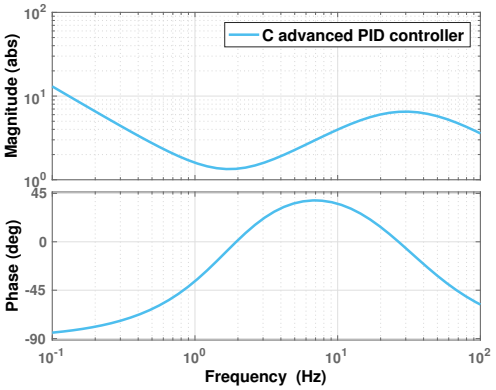

(b) Controller C_θ, $f_c = 10\,\text{Hz}$

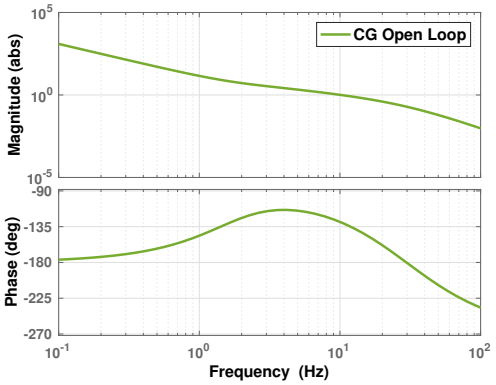

(c) open-loop response $L_\theta(j\omega) = CG$

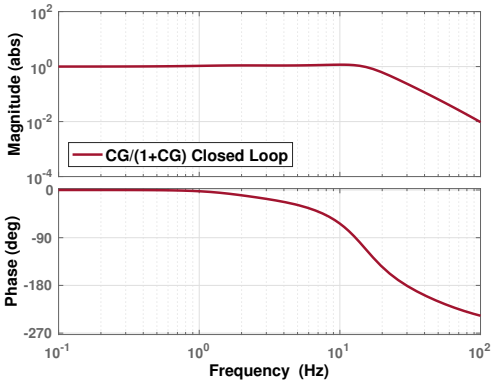

(d) closed-loop response $T_\theta(j\omega) = \frac{CG}{1+CG}$

Figure H.3: Advanced controller: The rotational motions are controlled with a tamed PID controller with an additional low-pass filter. It has a bandwidth of approximately 10 Hz.

I Software

The software for the demonstrator consists of five different files, that communicate with each other using UDP and SPI communication protocols. Details about the software implementation and installation are described in this appendix.

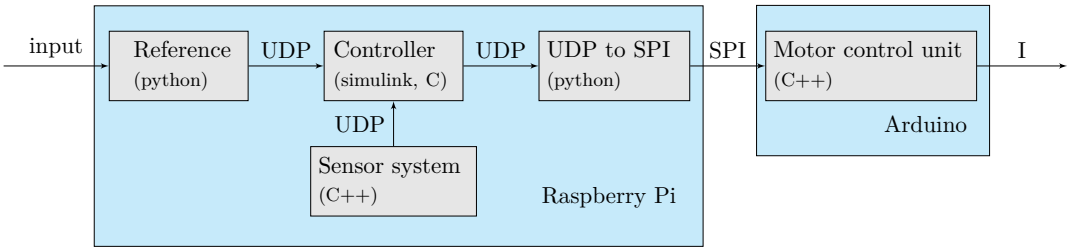

Figure I.1: Software overview

The software overview can be found in Figure I.1. The files are based on the following functions:

- Reference: receive the input from the 3D mouse and convert this into a position setpoint in x, y and θ.
- Sensor system: make image using the image sensor and process these into a position feedback.
- Controller: calculate the currents needed to create forces and torques.
- UDP to SPI: communicate between the Raspberry and the Arduinos.
- Motor control unit: convert the current setpoints into a PWM setpoint for the H-bridges. The H-bridges subsequently drive the current through the coils.

Communication creates a delay between the different algorithms. It is expected that these delays can be reduced by integrating the different software files in a single C++ program.

I.1 Communication: SPI

The Raspberry Pi is able to control the microcontrollers using different protocols: Universal Asynchronous Receiver Transmitter (UART), I2C and SPI (Serial Peripheral Interface). Since SPI is a simple communication protocol and fastest, it is chosen over UART and I2C.

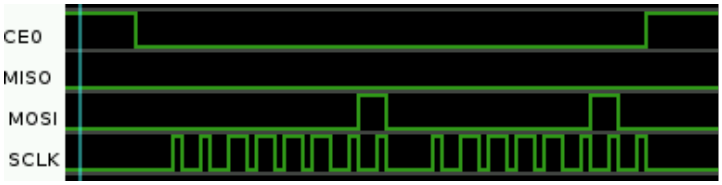

Figure I.2: SPI communication measured with piscope: sending out two bytes over SPI. First slave select 0 (CE0) is switch low to select slave 0, then the clock (SCLK) is enabled and is switched 8 times per byte. The value of MOSI determines what bit is sent each clock cycle. One byte consists of 8 bits. Binary 00000001 corresponds to a decimal 1 and 00000010 corresponds to a decimal 2.

SPI uses a master-slave configuration, the Raspberry Pi being the master and the Arduinos the two slaves. The master sends a clock signal, and upon each clock pulse one bit is shifted to the slave, and one bit is shifted back from the slave to the master. The signals are named Serial Clock (SCK) (or SCLK), Master Out Slave In (MOSI) and Master In Slave Out (MISO). The master is able to select which slave it is communicating to by using a separate Slave Select (SS) or Chip Enable (CE) signal per slave. The Raspberry Pi has a main SPI bus and an auxiliary SPI bus, therefore one SPI bus was used for each slave.

Since each slave controls the duty cycle of three or four H-bridges, four setpoints are sent to each slave. Each duty cycle setpoint is a value between 0 - 1200. Since one byte (8 bits) can contain 0 to 255, 2 bytes are used per H-bridge. Therefore a packet of 8 bytes is sent from the master to the slave to change the setpoints. To identify which byte arriving at the slave is the first, a simple communication protocol is used. The value of the first bit of the first byte is equal to 1, the first bit of the following 7 bytes equals zero. The remaining 7 bits per byte can be used for data. Only when all 8 bytes are received by the slave, they are written to a buffer containing the latest received setpoints.

I.2 H-bridge control

The setpoints from the Raspberry Pi sent over SPI are subsequently handled by the microcontrollers. The main loop continuously reads data from the buffer containing the latest setpoints, and recombines the 8 bytes into four setpoints. When the duty cycle setpoint is positive the left side of the H-bridge is switched and the right side is set to low continuously. When the setpoint is negative the right side of the H-bridge is switched and the left side is set to low.